

Nanomaterial Patterning in 3D Printing

Brian Elder, Rajan Neupane, Eric Tokita, Udayan Ghosh, Samuel Hales, and Yong Lin Kong*

The synergistic integration of nanomaterials with 3D printing technologies can enable the creation of architecture and devices with an unprecedented level of functional integration. In particular, a multiscale 3D printing approach can seamlessly interweave nanomaterials with diverse classes of materials to impart, program, or modulate a wide range of functional properties in an otherwise passive 3D printed object. However, achieving such multiscale integration is challenging as it requires the ability to pattern, organize, or assemble nanomaterials in a 3D printing process. This review highlights the latest advances in the integration of nanomaterials with 3D printing, achieved by leveraging mechanical, electrical, magnetic, optical, or thermal phenomena. Ultimately, it is envisioned that such approaches can enable the creation of multifunctional constructs and devices that cannot be fabricated with conventional manufacturing approaches.

1. Introduction

The ability to create tools to overcome environmental, biological, and societal challenges has been fundamental to human survival and evolution.^[1] However, conventionally manufactured devices have yet to approach the level of complexity and functional integration often exhibited in nature, such as in biological constructs.^[2–5] Naturally evolved constructs often exhibit 1) significantly higher geometrical complexity,^[6–13] 2) seamlessly integrated multifunctionality,^[13–19] and 3) the ability to spatially and temporally vary their properties.^[6,17,20–24]

The synergistic integration of nanomaterials with additive manufacturing, also known as “3D printing,”^[25–27] can enable the creation of geometrically complex, functional constructs. The ability to pattern nanomaterials in a 3D printing process can enable the fabrication of multiscale architectures that are seamlessly integrated with functional nanomaterials.^[28–55] This can be achieved by patterning and guiding the assembly of nanomaterials within a 3D printing process.

Indeed, in contrast to this multiscale 3D printing approach, achieving such a level of integration with conventional manufacturing techniques remains challenging. First, the geometrical complexity of structures fabricated with conventional manufacturing processes is typically limited. For example, advanced machining tools^[56,57] and microfabrication, such as photolithography,^[58,59] remain incapable of producing an entirely freeform structure with predefined voids and freestanding architectures.


Second, in contrast to the hierarchical assembly of a biological system, the degree of multifunctional integration achievable with conventional manufacturing techniques is often constrained by a postfabrication assembly process that is required to incorporate functional elements.^[60,61] In order to offset the high costs of tooling and production, significant design compromises must be made to preserve the modularity of a design.^[62–65] These competing requirements limit the degree of functional integration possible with conventional manufacturing approaches.

Third, the rapid personalization of device properties with a conventional manufacturing process is inherently challenging. Such modulation requires significant changes to a design, materials, and fabrication process, and is associated with an increase in lead time and development cost.^[66] This also constrains the functional complexity that can be programmed or imparted: for example, functional gradients typically exhibited in biological systems^[6,11,12,17,18,22,23,67] require the ability to modulate functional properties on-the-fly during a fabrication process, which is challenging with a conventional manufacturing process.

The ability to fine-tune functional material properties by incorporating nanomaterials in 3D printing processes offers an attractive approach to achieve seamless multifunctional integration. Nanomaterials are defined as materials having one of their dimensions in the range of ≈ 1 –100 nm.^[68] A significant subset of nanomaterials is particularly attractive as functional building blocks for device fabrication as nanomaterials exhibit a dependency of their functional properties with size, allowing the tailoring of properties for specific applications without the change of base materials. For example, in the nanoscale, the energy band gap of semiconductive nanomaterials (such as core-shell semiconductor quantum dots^[69]) becomes size-dependent when the size of the particle is smaller than the Bohr exciton radius.^[70,71] Further, the surface-to-volume ratio increases significantly as the length of a material approaches the order of nanometers.

B. Elder, R. Neupane, E. Tokita, U. Ghosh, S. Hales, Prof. Y. L. Kong
Department of Mechanical Engineering
University of Utah
Salt Lake City, UT 84112, USA
E-mail: yong.kong@utah.edu

E. Tokita
Department of Biomedical Engineering
University of Utah
Salt Lake City, UT 84112, USA

 The ORCID identification number(s) for the author(s) of this article can be found under <https://doi.org/10.1002/adma.201907142>.

DOI: 10.1002/adma.201907142

This geometrical effect increases the chemical and thermal reactivity,^[70] allowing the modulation of properties such as the decrease of melting point (tin^[72,73] and silver^[74,75] nanomaterials) as well as the increase of surface reactivity (zinc oxide nanowires and multiwalled carbon nanotubes as catalysts^[76]).

Recent advances in 3D printing have demonstrated the multiscale integration of nanomaterials^[25–27] to enhance mechanical properties^[29–38,77] and impart optical,^[39–43] electrical,^[33,44–47] thermal,^[37,38] actuation,^[31,48,49] and biological^[50–53] properties in 3D printed devices. Further, additional control over the deposition of nanomaterials (via phenomena such as evaporation^[40,78] and electrical forces^[33,54,55]) can impart anisotropy and heterogeneity in the functional properties of 3D printed constructs. The synergistic integration of the functional properties of nanomaterials and the versatility of 3D printing technologies can ultimately lead to the freeform fabrication of highly complex, heterogeneous, functional architectures (Figure 1a–c).

2. Overview: The Patterning of Nanomaterials for Multiscale 3D Printing

This review highlights the latest advances in controlling the deposition of nanomaterials with a wide range of physical phenomena (Figure 1d) to achieve a multiscale 3D printing process. This requires the ability to 1) pattern, organize or assemble nanomaterials (hereafter collectively referred to as pattern), 2) program the orientation of anisotropic nanomaterials, and 3) arrest the configuration of nanomaterials with a process that is compatible with the specific 3D printing technology. The manipulation of nanomaterial deposition can be achieved by understanding and modulating interparticle and externally applied forces that drive the assemblies of nanomaterials at the microscale to the mesoscale. As highlighted by Israelachvili et al., external forces or input of energy are required to direct nanoparticles to assemble in a specific configuration since nanomaterials do not self-assemble into the thermodynamically lowest energy state.^[79,80] Interparticle forces such as van der Waals attraction, steric repulsion, internal and external electrostatic and magnetic, solvation, capillary and convective, friction, and lubrication forces can modulate the short-range and long-range assemblies of nanomaterials.^[79,80] This review article discusses the patterning of nanomaterials to impart, enhance or modulate functional properties of microscale to macroscale 3D printed architecture which is achieved 1) by leveraging forces and energy that are dominant in a specific 3D printing process such as fluid flow and thermal energy, and 2) assisted by external electric or magnetic fields to realize self- and directed-assembly processes.

Specifically, we will first highlight the unique attributes of nanomaterials and their potential applications in imparting mechanical, electrical, and optical properties to 3D printed functional devices (Figure 1a). We will then introduce classes of 3D printing technologies that have been modified to achieve a multiscale integration process. Based on the nanomaterial integration strategies, we grouped the 3D printing technologies into two broad categories, “bulk” and “extrusion,” as shown in Figure 1b.

“Bulk” 3D printing methods encompass technologies in which a selective curing mechanism, such as crosslinking and



Yong Lin Kong is an Assistant Professor of the Department of Mechanical Engineering at the University of Utah (2018–present). Previously, he was a postdoctoral associate at the Massachusetts Institute of Technology (2016–2017). He received a B.Eng. in mechanical engineering from HKUST (2010), an MA, and a Ph.D. in mechanical engineering and materials science from Princeton University (2016). His research focuses on additive manufacturing of nanomaterial-based functional devices and biomedical devices.

sintering, operates within an ink or powder reservoir^[81–86] to create 3D features in a layer-by-layer approach. This includes stereolithography (SLA), digital projection lithography (DLP), continuous liquid interface production (CLIP), selective laser sintering (SLS), and binder jet 3D printing. In general, printing methods within this group can produce products with excellent surface finish,^[87,88] freestanding architecture and porous constructs.^[89] However, multimaterial integration and nanomaterial spatial variation are challenging in these categories, as the entire reservoir must be replaced to change the ink/powder materials. Some works have shown that localized integration is possible and can be achieved by applying the ink layer by layer using microfluidics,^[90] multiwavelength photopolymerization of multicomponent inks,^[91] or through the local injection of nanomaterials.^[49] Nevertheless, in most “bulk” 3D printing, nanomaterials have to be mixed with the entire ink bath and locally patterned with a range of physical phenomena.

In contrast, “extrusion” 3D printing methods encompass technologies in which the 3D printing ink is dispensed through a printhead or nozzle to create 3D features in a layer-by-layer approach. This includes fused deposition modeling (FDM), direct ink writing (DIW), direct inkjet printing, and aerosol jet printing (AJP). As the print bed is typically separated from the ink reservoir, this category of printing technologies is more versatile and can be readily modified to incorporate multiple materials. For example, the integration of multiple printheads in DIW or FDM allows the coprinting of a broad range of nanomaterials, polymers, or nanocomposites, enabling the merging of a wide range of materials in a single fabrication process.^[31,92–95]

Accordingly, we will highlight nanomaterial assembly and deposition in a 3D printing process, driven or assisted with physical phenomena (Figure 1d). In this review, the patterning phenomena are categorized as i) shear, ii) evaporative, iii) acoustic, iv) electrical, v) magnetic, vi) optical, or vii) thermal phenomena.

Shear force patterning represents mechanical rotation and translation of nanoparticles due to the motion of a fluid in a 3D printing process. For example, in the representative Figure 1di,

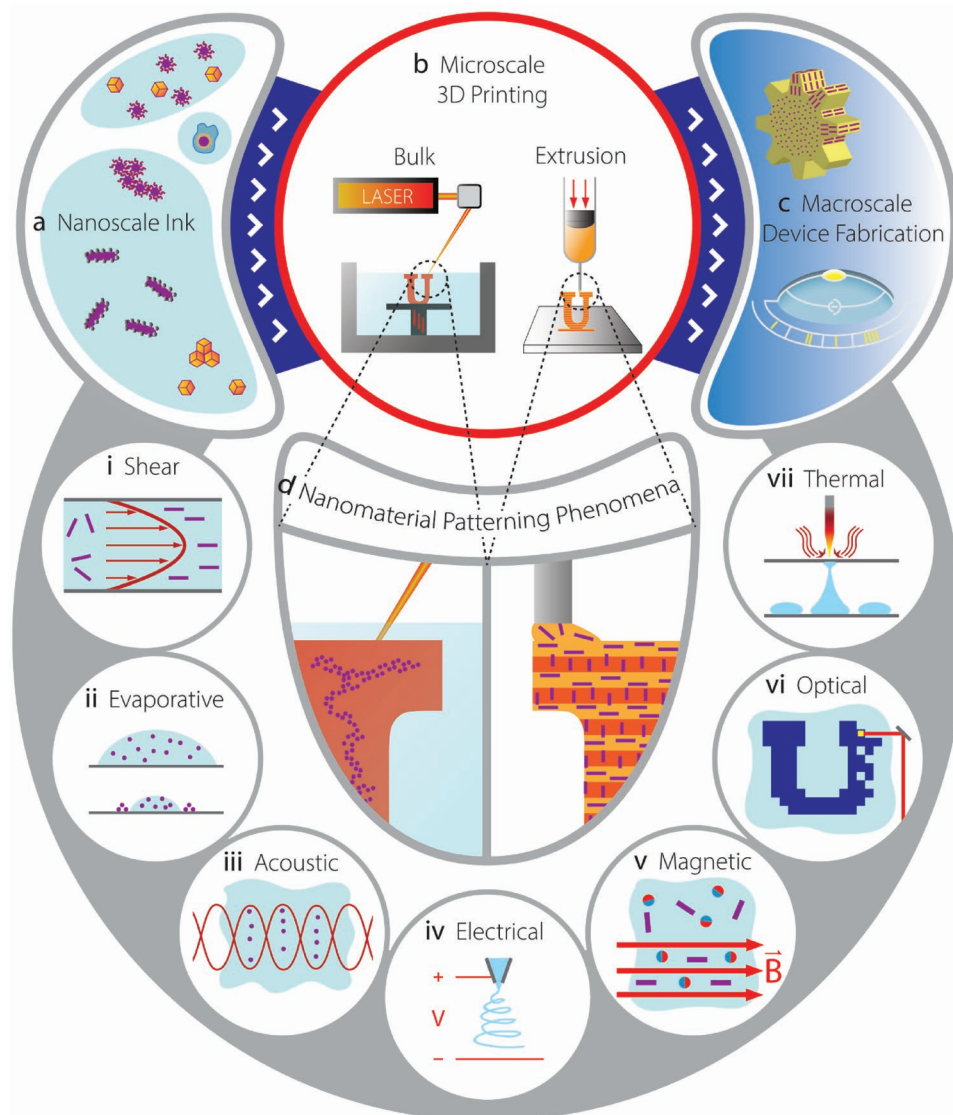


Figure 1. Multiscale 3D printing of functional devices with nanomaterials: a) the synergistic integration of nanoscale functional materials with b) a wide range of micrometer-scale 3D printing technologies, classified here as “bulk” and “extrusion” based printing c) can enable the creation of architecture and devices with an unprecedented level of complexity and functional integration. d) Multiscale 3D printing can be achieved via the patterning of nanomaterials integrated with 3D printing processes, driven or assisted by leveraging physical phenomenon such as i) shear, ii) evaporative, iii) acoustic, iv) electrical, v) magnetic, vi) optical, or vii) thermal phenomena. (Color legends: Red: patterning phenomena; light blue: 3D printing medium; purple: nanomaterials; and dark blue: cured/sintered ink.)

a velocity profile developed in a laminar flow inside a channel^[96] can align anisotropic particles.^[97]

Evaporative patterning describes patterning phenomena driven predominantly by an evaporation process of deposited ink droplets. Figure 1dii is a representative example of a complex and dynamic evaporative-driven nanoparticle assembly where the capillary flow will transport nanoparticles through advection.^[79,80] In combination with the effects of interparticle and particle-surface interactions, the drying of the droplet will ultimately kinetically trap nanomaterials on the substrate.

Acoustic force patterning leverages pressure waves often directed through the ink to drive the assembly of

nanoparticles.^[98,99] For example, Figure 1diii shows nanoparticles concentrated at the displacement nodes of a bulk acoustic wave.

Electrical patterning broadly describes the usage of electrical potentials to modulate the behavior of the ink, producing nanofilaments and nanodroplets directly from a larger reservoir, as well as orienting constituent nanomaterials. For example, Figure 1div shows an electrohydrodynamic printing process where surface charges, driven by high voltage, cause the fluid to eject as a rapid stream of droplets or as thin, continuous filaments with micrometer to nanoscale diameters. This allows for the direct fabrication of nanomaterial constructs.^[100,101]

Magnetic patterning leverages magnetic fields to align superparamagnetic nanoparticle-coated alumina platelets,

superparamagnetic colloids, ferromagnetic fibers, and nanoparticle–polymer composites. For example, as shown in Figure 1dv, a suspension of single-domain spherical nanoparticles and nonmagnetic nanorods coated with superparamagnetic iron oxide is aligned by the magnetic streamlines.

Optical patterning uses photons to achieve photopolymerization or to sinter powders in a 3D printing process. For example, in Figure 1dvi, a photon source polymerizes a voxel of ink within a tank of uncured resin. 3D printing processes based on two-photon polymerization can produce structures with nanosized features^[36] and custom lenses with nanoscale surface quality.^[43]

Thermal patterning uses thermal energy to modulate material system phase changes and crystal effects to guide the distribution of nanomaterials. For example, Figure 1dvii shows the application of a pointwise heat source that generates an electric potential in a lithium niobate wafer. The electric potential drives the droplet upward, to be deposited on the substrate.^[102]

3. Nanomaterials as Functional and Tunable Building Blocks for Devices

Indeed, recent advances in 3D printing have demonstrated how nanomaterials can alter 1) mechanical,^[29–38,77] 2) optical,^[39–43] 3) electrical,^[33,44–47] 4) thermal,^[37,38] 5) actuation,^[31,48,49] and 6) biological^[50–53] properties of 3D printed devices. The integration and manipulation of nanomaterials in 3D printing processes can impart tunable, functional properties to an otherwise passive construct. This multiscale patterning enables customization of the form and function of 3D printed architectures. For example:

Mechanical properties: Patterning anisotropic nanomaterials enables the creation of freeform composites with tunable, heterogeneous mechanical properties. For example, orienting alumina platelets and carbon nanotubes can replicate biological microstructures,^[29,34] including brick-and-mortar nacre,^[3,103,104] cholesteric mineralized chitin,^[4,10] and concentric cortical osteons.^[5,105] Such capability transforms an otherwise homogeneous passive construct into a nanocomposite with a tunable stress–strain response that can be used for steering crack propagation, optimizing directional load-bearing, and improving resistance to surface wear.^[29,77]

Optical properties: A subset of nanomaterials can impart optical properties where the band gaps can be tuned by changing the size of the particles due to quantum confinement effects. For example, colloidal quantum dots with size-tunable emission spectra can be used to 3D print multicolor light-emitting diodes.^[40] Furthermore, 3D architectures with heterogeneous, programmed absorption of polarized light can be fabricated by aligning metallic gold nanorods in an extruded polymer matrix.^[39] Nanomaterials can also be used to create structural color due to diffraction phenomena. For example, a tunable photonic crystal can be constructed from superparamagnetic colloidal crystals^[42] or eutectic metals.^[106] The distances between lamellar formations in the microstructure can be tuned to produce multicolored architectures.

Electrical properties: Electrically conductive nanomaterials can impart electrical properties to 3D printed structures. The

patterning of metallic and carbonaceous nanoparticles^[107,108] within 3D printed structures can produce freeform circuits and flexible electronics. For example, stretchable, conductive 3D traces containing silver nanowires^[109] can enable the fabrication of stretchable displays,^[110] stretchable antennas,^[111] and artificial muscles.^[112,113] Furthermore, local isolation of conductive nanomaterials can lead to complex, freeform circuits. For example, the simultaneous jetting of metal ion solutions can achieve chemical separation down to 400 nm.^[33]

Thermal responsive properties: Nanomaterial patterning can introduce thermally responsive properties. For example, by 3D printing graphene into delicate aerogel structures, a highly conductive nanomaterial can be patterned into a device with semiconductor-like behavior—specifically a temperature-dependent resistance.^[37,38] A combination of direct ink writing (DIW) and freeze casting transforms an aqueous solution of graphene oxide (GO) into a stiff, porous aerogel that is resilient to compressive loading. Supercooling of the aqueous solution causes ice dendrites to grow—aligning and concentrating the GO sheets along the crystal boundaries.

Actuation properties: Spatial variation in the concentration and orientation of nanomaterials can impart actuation abilities in 3D printed architecture. For example, orienting anisotropic nanofibers and platelets can produce shape-changing structures with programmable shape deformation.^[31,48] Composites containing anisotropic nanomaterials exhibit greater stress transfer between the host matrix and the principal edge/face of the nanoparticle, leading to anisotropic stress–strain behavior.^[114,115] Upon absorbing the solvent, the composite features increased swelling in the transverse direction relative to the axial direction of the nanoparticle loading. Convex and concave curvature is produced by combining printed filaments and layers with different swelling directions. Printing structures with this programmed hygromorphism^[116] results in complex shape transformations that resemble plant movement.^[20,116] Spatial variation in nanomaterial concentration can also be used to program regional differences in functional properties. For example, ferromagnetic iron nanoparticles can be confined by a local magnetic field to discrete regions within a printed structure.^[49] The structure features regional differences in magnetic remanence, which can be used for teleoperation. Rotation, translation, and deformation can be controlled through the attraction and repulsion between the structure and an external magnetic field.

Biological properties: The inclusion of nanomaterials into biocompatible substrates such as hydrogels can enhance bioactivity, and cell viability, of a 3D printed biomaterial.^[50,51,117] For example, incorporating nanomaterials such as nanosilicates^[118] and hydroxyapatite nanoparticles^[52] in hydrogels laced with human mesenchymal cells increases cell viability by up to 80%, increases osteoblast differentiation, and upregulates gene expression. Incorporating two-dimensional (2D) graphene sheets into scaffolding increases cell alignment,^[53] while the enhanced electrical conductivity improves cardiomyocyte stimulation.^[119] Lastly, carrier inks based on interactions between biocompatible nanoparticles and hydrogel polymers can form the backbone of rapid innovation in bioprinting.^[120] The carrier ink forms a transient polymer network that retains its tailored rheology after including secondary polymers and biological materials, hastening the process of producing biocompatible

inks. In addition, charged nanoparticles can increase network crosslinking, which reduces hydrophilic swelling, thereby improving the ability to print high-fidelity biocompatible architecture.^[121]

In summary, the seamless integration of nanomaterials with 3D printing can enable the fabrication of active structures with mechanical, optical, electrical, thermal, magnetic, actuation, and biological functional properties. Nanomaterial patterning techniques can impart and modulate nanoscale effects to control the deposition, concentration, and orientation of nanomaterial reinforcement. Next, we will briefly review the 3D printing technologies that have been used to achieve the multiscale integration with nanomaterials.

4. 3D Printing Methods

3D printing is defined as a computer-controlled, additive fabrication process wherein material is joined or solidified to form complex geometric structures.^[25,122–125] 3D printing is a broad class of advanced manufacturing technologies: the term “3D printing” was first coined in 1989 by Emanuel Sachs et al. with the invention of binder jetting 3D printing technology.^[124,125] although the concept of 3D printing was developed as early as 1986 with the invention of stereolithography.^[125,126] Over the past decades, a myriad of 3D printing technologies have been developed: from two-photon polymerization, with as small as nine-nanometer voxel resolution, in 2013^[127,128] to continuous liquid interface production in 2014.^[123,129] In parallel, there has been a significant increase in consumer-level desktop-sized 3D printing platforms since the expiration of certain patents^[130,131] driving the creation of open-source freeform fabrication platforms.^[123,132,133]

In contrast to conventional manufacturing, which requires molds, dies, or lithographic masks,^[125] 3D printing technologies are particularly powerful in complementing the mass production methodology in meeting the demands of manufacturing projects when economies of scale are no longer applicable. In addition to enabling a rapid prototyping capability, which significantly reduces device development time and cost, 3D printing allows for the personalization and customization of parts. In a streamlined process, a virtual model is designed in software, translated into machine instructions, and replicated in physical form. A single printer can produce thousands of different designs without molds, dies, or masks. This capability advances the field of medicine with the invention of personalized biomedical devices such as hip replacement implants,^[134] dental implants,^[135] ingestible electronics,^[136–138] and magnetic resonance imaging compatible devices^[139] that can potentially address significant unmet clinical needs.^[50,140–142] This also enables the creation of complex 3D geometry for applications in the aerospace^[143,144] and automotive^[144] industries, which are otherwise challenging to fabricate and assemble through traditional methods. Further, 3D printing can also be used to augment traditional manufacturing in a hybrid additive-subtractive six-axis machining robot, which reduces production time and material cost.^[145]

Despite significant potential applications, most commercially available 3D printing has yet to extend beyond the

fabrication of mechanical structures and prototypes. Primarily, achieving functional device printing requires the incorporation of multiple materials within a 3D printing process. This is challenging for two reasons: first, a significant subset of 3D printing technologies, such as stereolithography and binder jet, are developed and optimized to only fabricate a single material in each printing cycle.^[125] In order for the material to be changed, the ink bath or powder must be replaced. Second, the inclusion of additional materials often confounds the 3D printing development process as it is challenging to achieve the simultaneous optimization of multiple materials, primarily due to competing optimization requirements and material incompatibilities.^[146,147] However, the incorporation of nanomaterials into 3D printing processes allows for the optimization of device properties in both bulk and extrusion printing methods while extending the potential applications of these technologies.

To incorporate nanomaterials into 3D printing, nanomaterials typically are mixed either with solvents, polymers, or photocurable resins, depending on the 3D printing methods. For example, nanomaterials can be dispersed in aqueous or organic solvents^[148] and printed as-is, or mixed with polymers or resins. Nanomaterials can also be spread over the print bed in powder-based methods such as selective laser sintering (SLS). This section will highlight fundamental 3D printing technologies commonly used with nanomaterials by providing a brief overview of the underlying mechanisms behind each technology.

In this review, we have broadly categorized “3D printing” into two general categories in the context of nanomaterials integration, as described in the last section. Briefly, bulk methods (Figure 2a–e) describes technologies that print directly in a large reservoir of raw material by selectively curing, sintering, or binding material in a layer-by-layer fashion. Bulk methods include technologies such as stereolithography (SLA),^[126,149] digital projection lithography (DLP),^[84,125,150] continuous liquid interface production (CLIP),^[129] two-photon polymerization (2PP),^[125,151] powder bed fusion (PBF),^[81,82,152] and binder jet printing.^[89,153] Extrusion methods encompass 3D printing methods in which build material is selectively deposited on a print bed from a separate reservoir. Extrusion methods include technologies such as fused deposition modeling (FDM),^[125] direct ink writing (DIW),^[93] electrospinning, e-jet printing, and direct inkjet printing.^[124,154,155]

Bulk methods: Bulk methods are generally limited to printing with a single material and have a limited material selection due to the curing, sintering, or binding mechanisms that are involved. Furthermore, most bulk methods use photopolymers or high-temperature sintering of metals, both of which hinder the biocompatibility of the finished product.^[156] Binder jet 3D printing requires postprocessing (such as annealing) or addition of chemicals to consolidate the 3D structure. Geometric considerations should also be taken into account to allow resin or powder trapped in voids to be removed.^[157] **Table 1** summarizes the material selection and fabrication strategy of bulk printing methods.

Several considerations must be evaluated for each printing technology. In bulk 3D printing methods, the size, shape, and type of nanomaterials, such as cellulose nanocrystals,^[158] nanowires,^[44,159] carbon nanotubes,^[160] and graphene nanosheets,

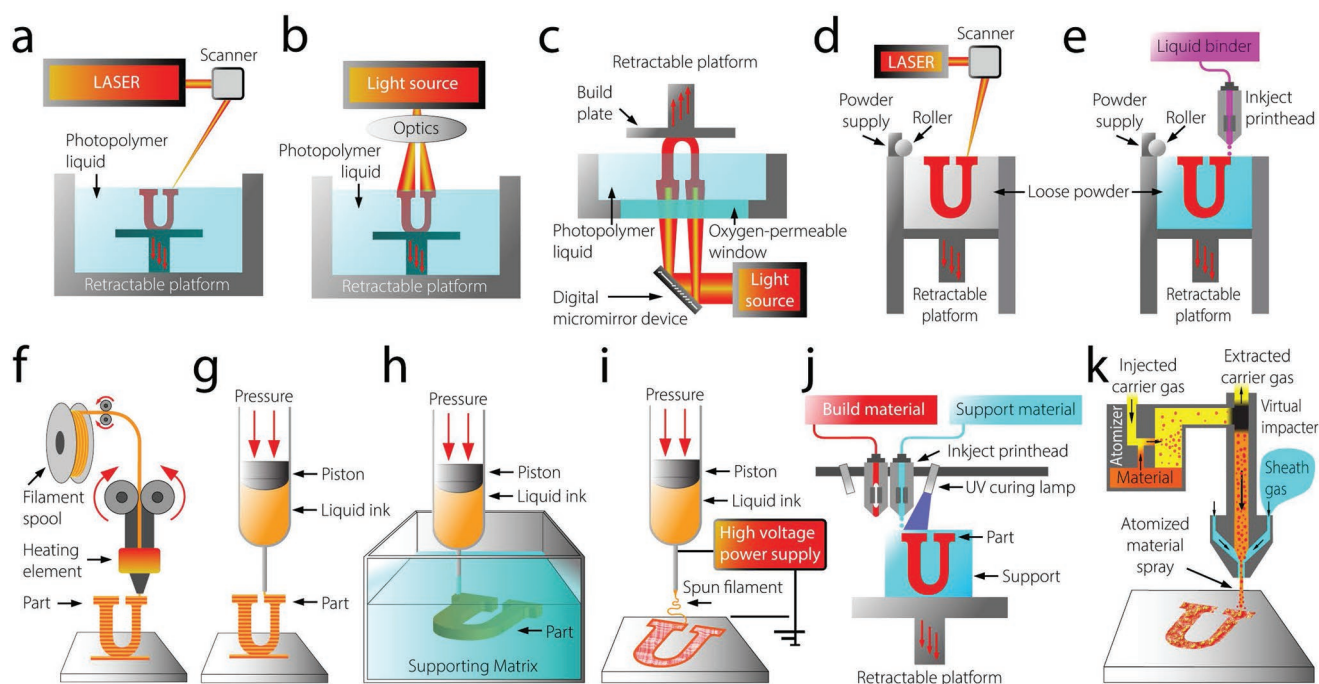


Figure 2. Schematics of bulk and extrusion 3D printing methods. a–e) Bulk methods: a) top-down laser stereolithography (SLA), b) top-down digital projection lithography (DLP), c) continuous liquid interface production (CLIP), d) powder bed fusion (PBF), and e) binder jet. f–k) Extrusion methods: f) fused deposition modeling (FDM), g) direct ink writing (DIW), h) sacrificial/embedded printing, i) electrospinning, j) direct inkjet printing, and k) aerosol jet printing (AJP).

can affect the printing process. For example, in SLA, high fill content (>50%) of nanowires, added to increase resilience to shape distortion due to shrinkage,^[159] will increase light scattering. The light scattering is affected by the size and shape of the nanoparticles, the loading of the nanoparticles, and the refractive index of the nanoparticles and resin.^[161] This light scattering reduces the selectivity of the curing laser, reducing the curing depth and increasing the curing width. In powder-based printing methods such as SLS and binder jetting, the particle size and shape affect the ease of rolling or spreading the powder.^[89] Nonspherical particles have more interparticle contact, thus more friction. Small particles (<1 μm) tend to agglomerate due to van der Waals attraction and require additional stabilizers. Particles around $\approx 20 \mu\text{m}$ can be spread as a dry powder, while particles less than 5 μm require a solvent to spread evenly.

The following is an overview of different bulk 3D printing technologies.

Stereolithography (SLA) uses an ultraviolet (UV) laser to photopolymerize a photocurable resin layer by layer (Figure 2a).^[162] Optics focus the laser radiation on a microscale area on the resin reservoir, and movement of this laser across the surface promotes shallow curing. The dimensions of the cured voxel are affected by laser power, particle loading, and refractive indexes of the particles and resin.^[129,161] Once the laser polymerizes a single layer, new liquid resin is introduced to begin the next layer. This process is repeated until the desired 3D object is formed. SLA is capable of producing structures with high-resolution features,^[125] though the method of photopolymerization limits the range of applicable materials.

Similar to SLA, digital projection lithography (DLP) uses UV light to selectively polymerize a liquid resin. Instead of using a single focused laser, DLP uses a spatial light modulating (SLM) element, such as a liquid-crystal display (LCD)^[85] or digital micromirror device^[84] to project an entire 2D slice on the resin-build plate interface. This allows an entire pattern to be printed at once (Figure 2b), decreasing the time to print.^[85] Most examples of DLP are limited to single material printing, and resolution is constrained by the dimensions of constituent pixels or micromirrors.^[85] However, Miri et al. have demonstrated a novel method for multimaterial DLP by leveraging a micro-fluidic device, which can switch among different cell-loaded, hydrogel bioinks by flooding the miniature patterning reservoir between sequentially cured layers.^[90]

Continuous liquid interface production (CLIP) uses a similar projection method to DLP, with the addition of an oxygen-permeable window. Oxygen inhibits photopolymerization, producing a “dead zone” of uncured resin between the polymerized part and the window, where the resin is continually replenished (Figure 2c).^[129] This enables a continuous printing process, surpassing the print speed (hundreds of millimeters per hour) of similar light-based bulk 3D printing methods, limited only by resin photopolymerization properties.^[123,129]

Two-photon polymerization (2PP) uses near-infrared femtosecond laser pulses to polymerize a nanoscale voxel at the focal point of the laser.^[123] The laser focal point is then scanned in three dimensions to obtain arbitrary structures. The small working distance between the optics and substrate limits the scalability of 2PP to a few millimeters. However, the addition of scanning optics can overcome this limitation.^[36]

Table 1. Summary and comparison of bulk 3D printing methods.

Method name	Printing materials	Fabrication strategy	Typical resolution and speed
Stereolithography (SLA)	Photocurable resin	Point-wise light projection onto cured-uncured resin interface	Resolution: 50–200 μm ^[125] Speed: 1000 mL h ⁻¹ ^[188]
Digital projection lithography (DLP)	Photocurable resin	A complete 2D pattern is projected onto liquid resin by digital micromirror device or spatial light modulating element	Resolution ^{a)} : 1 μm ^[85] Speed ^{b)} : $\approx 50 \text{ mm h}^{-1}$ ^[423–426]
Continuous liquid interface production (CLIP)	Photocurable resin	Continuous DLP enabled by oxygen-permeable window	Resolution ^{a)} : 10–100 μm ^[86] Speed ^{c)} : 500 mm h ⁻¹ ^[129]
Two-photon polymerization (2PP)	Photocurable resin	Near-IR femtosecond pulse is used to achieve polymerization by two-photon absorption at the focal point of the laser	Resolution: 100 nm ^[125] Speed: 80 nm s ⁻¹ to 2 cm s ⁻¹ ^[85]
Powder bed fusion (PBF)	Polymer, metal, and ceramic powders	High-power laser or electron beam selectively fuse powder on leveled bed	Resolution ^{d)} : 20–100 μm ^[188,427] Speed ^{d)} : 1000 mL h ⁻¹ ^[188,428]
Binder jet	Polymer, metal, and ceramic powders and compatible liquid binder	Ink-jetted liquid binder selectively binds powder on leveled bed	Resolution: 50–400 μm ^[153] Speed: 25 mm h ⁻¹ ^[429]

^{a)}Resolution is pixel size-dependent.^[85] ^{b)}Print speed is independent of print area.^[423–426] ^{c)}Print speed is independent of print area. Print speed is dependent on layer resolution, photon flux, oxygen flux, photoinitiator absorption coefficient, and required resin curing dosage.^[129] ^{d)}Resolution and print speed is based on reported SLS performance.^[188,426,427]

Powder bed fusion (PBF) uses a high-power photon or electron source to selectively fuse metal, ceramic, or polymer powder layer by layer, while fresh powder is spread onto the previously bonded layer. Figure 2d depicts a generalized PBF strategy using photonic power.^[81,82] PBF is a general 3D printing category that includes several unique powder bed technologies: low-temperature, polymer processing PBF printers are commonly referred to as selective laser sintering (SLS), while high-temperature PBF printers are commonly referred to as selective laser melting (SLM). In general, PBF leverages binding mechanisms such as solid-state sintering, liquid phase sintering, and full melting. PBF is capable of producing pure metal and ceramic structures with tunable porosity, but the high temperatures required for fusion can damage biomaterials and induce shrinkage in the part.

In solid-state sintering, the heated bed and high-power laser heat the particles between 50% and 100% melting temperature.^[152] In the solid-state sintering process, the particles remain in solid form and fuse together to reduce the free energy of the system.^[152] The unbonded powder provides support to the sintered parts during the printing process, allowing for the printing of overlaps. Solid-state sintering is used primarily to low-melting-point materials such as polymers. Solid-state sintering is not typically the primary fusion mechanism for PBF as it is slower than fusion by melting.^[152] Further, holding the powder at these elevated temperatures can induce additional undesired fusing of particles around the printed part.

Another primary binding mechanism for PBF is liquid phase sintering (LPS) or partial melting, where binding materials with lower melting temperatures are added (as particles, coatings, composites, or indistinct mixtures) and then melted to bind the target particles at lower temperatures.

Postsintering volatilizes the binding polymer and fuses the remaining particles, reducing the size of voids between particles.

In full melting PBF mechanisms, such as SLM and electron beam melting (EBM), a high power laser and electron beam, respectively, fully melt the powder during the printing process. EBM focuses and scans the electron beam using electromagnetic coils, which have a near-instantaneous response compared to the lenses and galvanometers used in SLM. The elevated temperature during printing also relieves residual stress. However, electron–gas interactions and the buildup of repulsive negative charges can reduce the resolution of the printing. Hence EBM is performed under a partial-pressure vacuum, and special consideration is given to the scanning pattern and material conductivity to reduce charge accumulation.

Finally, binder jet printing jets tiny droplets of binder onto a polymer, metal, or ceramic powder using an inkjet print-head (Figure 2e).^[83] This process can result in low-density, highly porous structures. Similar to PBF, the internal geometry must provide outlets for unbonded powder as the part is removed from the bed. Once extracted from the unbonded powder, the “green” part is postprocessed. One method is infiltration, wherein additional material in liquid form is permeated through the part, filling holes and solidifying the part. Additionally, postprocess sintering is used to volatilize the binder and increase density.^[163,164] The reduction in porosity is driven by free energy, which causes the particle surfaces to diffuse and join together. However, this sintering can induce shrinkage and generate internal stress. After sintering, the part can be infiltrated with a material with a lower melting temperature. This can positively affect stiffness and functional properties. When used with metal or ceramic powder, postprocess sintering

results in a pure metallic or ceramic structure with tunable porosity.

Extrusion methods: Dispensing nozzle diameter and resolution of the driving motors significantly affect the print resolution in extrusion methods. However, without the need to selectively cure microscale regions within an encompassing volume of fluid, extrusion methods exhibit versatility in dispensing techniques and curing strategies that allow 3D printing with a broader selection of materials. Isolated material reservoirs allow many extrusion methods to accommodate multimaterial printing as well as gradual mixing of materials during the printing process.^[165] Furthermore, both FDM and highly viscous DIW can produce overhangs, with inclination and radius of curvature dependent on capillary forces and yield stress.^[31] This reduces the reliance on the support material and enables the production of fully enclosed geometry. **Table 2** summarizes different features for extrusion printing methods.

In general, the rheological properties of the nanocomposite ink in extrusion 3D printing methods is tuned such that it can be extruded from the nozzle, without challenges such as clogging due to nanoparticle aggregation.^[166,167] In high viscosity DIW, inks are often formulated to have shear thinning behavior, which reduces the apparent viscosity with increasing shear rate to promote extrusion through the nozzle.^[167] The shear thinning behavior is dependent upon the particle concentration in ink. For example, fumed silica nanoparticles are used as they have excellent thermal stability and their hydrophobicity is suitable for organic, hydrophobic inks.^[168] The particles form aggregates, which lead to solid-like behavior as the aggregates form a network. When shear stress is applied during a printing process, the aggregates break up, and the inks behave more liquid-like. For aqueous inks, laponite

nanoclay and hydrophilic fumed silica can be used as hydrophilic alternatives.

An overview of extrusion-based 3D printing technologies is summarized below.

Fused deposition modeling (FDM) uses rollers to push thermoplastic filament through a heated metal nozzle (Figure 2f).^[92] The heated polymer is extruded onto the substrate, tracing linear and curved paths to generate a 3D structure layer by layer. Multiple active nozzles with separate feedstocks can enable the fabrication of composite structures with multiple materials.

Direct ink writing (DIW) extrudes liquid ink through a nozzle or needle, some examples use pneumatic pressure as the driving force (Figure 2g).^[93] In general, liquid ink is formulated so that it cures or evaporates in atmospheric conditions and has sufficient yield stress to support its shape until sufficient curing occurs.^[125] Viscoelastic ink with shear thinning behavior is often used to print through small nozzles with lower pressure. Unlike inkjet printing ($2\text{--}10^2$ mPa s^[94,123]), DIW is compatible with a wide range of ink viscosity ($2\text{--}10^6$ mPa s^[125]), capable of printing inks with a high volume fraction of nanoparticles.^[169] Additionally, multiple syringes can be used to print multiple materials,^[170–173] while inline mixers can produce material hybrids and material gradients, which allows for regional differences in functional properties.^[31,174]

Low viscosity materials without sufficient yield stress to form self-supporting structures can be printed in a supportive bath in a DIW process. Specifically, in sacrificial and embedded 3D printing, the nozzle of an ink dispensing system is inserted into a matrix of soft material. The supporting structure allows the ink to be 3D printed by tracing a 3D trajectory, instead of being limited to a layer-by-layer, stacking printing methodology

Table 2. Summary and comparison of extrusion 3D printing methods.

Method name	Printing materials	Fabrication strategy	Typical resolution and speed
Fused deposition modeling (FDM)	Thermoplastic filament	Heated extrusion of solid filament	Resolution: 100 μm ^[188] Speed: 100 mL h ^{−1} ^[188]
Direct ink writing (DIW)	Viscoelastic ink Shear thinning fluid	Liquid ink solution is extruded from a nozzle	Resolution ^{a)} : 1–250 μm ^[125] Speed: 100 mL h ^{−1} ^[188]
Direct inkjet printing	Low-viscosity fluid	Droplets of liquid ink solution are ink-jetted on a substrate	Resolution: 240 nm to 5 μm ^[430] Speed: 500 mL h ^{−1} ^[188]
Sacrificial/embedded printing	Ink: Ink compatible with DIW process. Support: shear thinning fluid, or high viscosity reservoir and low viscosity filler combination	Nozzle injects material into a soft, supporting matrix	Resolution ^{a)} : 1–250 μm ^[125] Speed ^{b)} : 1300 mL h ^{−1} ^[177]
Electrospinning, E-jet	Polymer-based solution	Applied high voltage extrudes nanoscale filaments or individual droplets	Resolution: 100 nm to 20 μm ^[431] Speed ^{c)} : 20–1500 mL h ^{−1} ^[432]
Aerosol	Metal inks, biological inks, adhesives, polymers, and dielectrics	Aerodynamic focusing of aerosolized material	Resolution: 10 μm ^[186] Speed: 1200 mL h ^{−1} ^[433]

^{a)}One to two orders of magnitude larger than constituent materials;^[125] ^{b)}Speed is dependent on nozzle diameter and motor speeds;^[177] ^{c)}Single needle electrospinning, high-speed electrospinning, respectively.^[432]

(Figure 2h).^[168,175–178] Printing parameters such as nozzle diameter, printing speed, and pressure^[179] can be tuned to print each segment in a single pass without coprinting of supporting structure, which dramatically reduces the print time (≈ 140 times faster than SLA).^[177]

In sacrificial 3D printing, the supportive matrix typically consists of shear thinning material with thixotropic behavior, which allows the supportive material to rapidly fill voids left by the moving nozzle. Once the part is printed and cured, it can be removed from the supporting matrix without discarding the support material. Alternatively, a cell-laden hydrogel ink can be printed in a “thermoreversible support bath” such as gelatin microparticles.^[180] Known as freeform reversible embedding of suspended hydrogels (FRESH), the support bath is removed by melting at a biocompatible temperature of 37 °C. In embedded 3D printing (e-3DP), the ink is injected into a shallow reservoir of support material that is cured along with the injected ink.^[176] The simultaneous curing or polymerization of ink and support material produces an embedded functional part, such as embedded circuitry for flexible electronic devices.

Since the printed ink does not require self-supporting characteristics, both sacrificial and embedded 3D printing are applicable with a wide range of materials, including liquid metal,^[175] carbon-based conductive silicone,^[176] and biological materials.^[180] Suspension matrices can include self-healing hydrogel,^[175] granular gels,^[178] silicone elastomer,^[176] and fumed silica suspensions.^[168] Another variant of this method uses the ink as the sacrificial material.^[191,193] The ink is injected into a matrix of cell-laden hydrogel or stem cell “organ building blocks” and evacuated, producing artificial vascular networks.

This printing method is primarily limited by the compatibility between the injected ink and the support material.^[168] For example, the hydrophobicity or hydrophilicity of the injected ink should be matched with the support material to prevent interfacial tension from deforming the injected ink, which is critical to allow the printing of fine features and continuous paths. In addition, the support material must be stable over the working temperature range to provide adequate support.

In electrohydrodynamic printing (EHD), a voltage between the nozzle and substrate is used to eject fluid from the nozzle. Electrical, physical, and rheological properties play an important role in EHD printing. Due to an applied electric field, charges develop in a droplet at the tip of the nozzle. The charges are attracted to the collector electrode, elongating the droplet into a Taylor cone. When the repulsive force of the charged droplet exceeds the surface tension, a fluid jet is formed. A subset of EHD printing, electrospinning printers eject the fluid in a continuous stream, which is pulled toward the substrate in continuous fibers (Figure 2i).^[100,181] Utilizing the charged state of the fluid, a balance between electrostatic force, surface tension, and viscous flow pull the fluid into a filament with a smaller diameter than the extruding nozzle.^[101,182] Based on the distance between the nozzle tip and substrate, electrospinning can be classified as either far-field or near-field. Far-field electrospinning produces highly porous, disorderly mats whereas near-field electrospinning can produce a controlled deposition of individual strands, reminiscent of the lines of filament produced by FDM or DIW.^[55,100] This difference in morphology is due to the short distance over which near-field fibers travel

which limits the effect of bending instability from the interaction between the charged filament and electric field. Another subset of EHD printing, E-jet printing, rapidly ejects individual droplets, with increasing droplet extrusion frequency at higher voltages.^[183] In this variation of EHD printing, the surface tension of the fluid overcomes viscous flow, which causes the fluid jet to form droplets.^[182] Solid metal structures can also be formed with fast evaporation of solvent and postprocess annealing or ion reduction.^[33]

Direct inkjet printing refers to the deposition of droplets by means of a valve inside the printhead, formed by electrostatic, thermal, or piezoelectric plates (Figure 2j).^[94] For example, photopolymer can be jetted and cured using a UV lamp, in a layer by layer approach. Although direct inkjet printing uses a similar technique to binder jet printing, direct inkjet printing uses low viscosity fluids ($2\text{--}10^2$ mPa s) as the primary print material, rather than a binder for granular media.^[94,123] Direct inkjet printing can rapidly print multiple materials simultaneously through an array of nozzles.

Aerosol jet printing (AJP) uses aerodynamic focusing to guide a narrow spray of atomized fluid onto a substrate.^[184] The print material is atomized by either ultrasonic waves or pneumatic pressure, then carried by a flow of gas to the deposition head. A second gas flow (the sheath gas) protects the ink from the walls of the narrowing nozzle and compresses the gas into a focused stream (Figure 2k). Postprocess drying or sintering also affects the final print characteristics, such as pore size and surface finish.^[184,185] Since aerosol printing is a noncontact process that relies on pneumatic jetting, an approximate standoff distance of 1–5 mm between the nozzle and substrate allows omnidirectional printing^[186] with fine features as small as 10 μm . This grants the ability to conform to curved surfaces, ensuring good coverage on nonplanar surfaces.

In summary, the wide range of 3D printing methods available offers flexibility in material selection, geometry, and fabrication strategy when producing complex, multimaterial constructs. Bulk methods are generally more limited in material selection but can often achieve better layer adhesion and smoother surface finishing in printed parts. Extrusion methods have a wider range of material selection and achieve multimaterial printing. However, the print resolution is significantly affected by a wide range of parameters, such as the ink formulation and the nozzle size. For further detailed discussions of 3D printing technologies, the reader is referred to several reviews which further discuss details about these techniques in the context of adjacent fields.^[85,125,152,187,188]

The integration of nanomaterials and 3D printing technologies can transform the paradigm of 3D printing into a multiscale, heterogeneous patterning process. Nevertheless, achieving the multiscale integration of nanomaterial inks and microscale 3D printing technologies to program functional properties in mesoscale devices requires the ability to pattern nanomaterials during the 3D printing process. The following section highlights the recent advances in nanomaterial patterning within 3D printing, organized into fluid shear, evaporative, acoustic, electrical, magnetic, optical, and thermal phenomena. These patterning techniques are critical to extending the scope of 3D printed architecture from passive constructs to functional devices.

5. Fluid Shear Patterning

“Fluid shear patterning” describes the alignment of anisotropic nanoparticles in a deposition process by leveraging the fluid shear forces within the bulk fluid motion. For example, in an extrusion 3D printing method such as DIW, an anisotropic nanoparticle (e.g., nanofibers, nanowires, or nanoplatelets) will experience shear stress to realign its principal axis with the direction of the laminar flow established inside the nozzle, as shown in **Figure 3a**.^[97,189] The fluid shear stresses are a result of the radial fluid velocity gradient, due to the no-slip boundary layer at the inner surface of the nozzle.^[96] Fluid shear alignment can also occur outside the extrusion nozzle. In electrospinning, electrical forces overcome surface tension and accelerate a charged fluid jet toward the collector,^[101] producing a thin filament (sub-micrometer diameter) which achieves a high degree of alignment due to the decreasing fluid cross-section.^[39] Interestingly, in “bulk” resin 3D printing methods, shear alignment is also possible and is affected by the reservoir geometry and shear rate profile.^[190]

Fluid shear patterning can be used to program anisotropic stress-strain behavior in 3D printed structures by introducing regional variation in the orientation of anisotropic nanomaterials. This functional property can be used to program shape deformation in response to external stimuli. For example, Gladman et al. used this method to create shape-changing “4D” structures with programmable swelling.^[48] As shown in **Figure 3a**, DIW was used to print poly(*N,N*-dimethylacrylamide) hydrogel with nanofibrillated cellulose fiber reinforcement. As the ink passed through the nozzle, the cellulose fibers aligned longitudinally with the printed filament, creating an anisotropy in the elastic modulus ($E_{\parallel} \approx 40$ kPa and $E_{\perp} \approx 20$ kPa). This led to an increase in swelling strain in the transverse direction ($\alpha_{\parallel} \approx 10\%$ and $\alpha_{\perp} \approx 40\%$) of the printed filaments (**Figure 3a**). As a result, the structure changed shape when the hydrogel absorbed water. The folding of the printed structure was influenced by the geometry of the structure as well as the direction of the filament that makes up each layer, as predicted by Timoshenko theory.^[48] Filaments were patterned into spirals, grids, and radial spokes. These basic shapes were used to program 4D structures that mimicked the hygromorphism, or water swelling-induced deformation, in flowers.^[116] The folding could be reversed by replacing the hydrogel polymer poly(*N,N*-dimethylacrylamide) with poly(*N*-isopropylacrylamide), which expels water at higher temperatures (32 °C).^[191] Such responsive properties are highly desirable. For example, the ability to program controlled, repeatable movements in a 3D printed structure is an essential prerequisite for the fabrication of customizable devices with environment-responsive abilities, such as smart textiles^[192] and robotics.^[193]

Fluid shear patterning can also be used to print self-supporting structures by providing the fluid shear necessary for shear thinning behavior. To support the extrusion printing of materials with low yield stress, nanoparticle loading can be added to impart stress thinning and yield stress behavior. For example, Jin et al. used laponite nanoclay platelets as an internal scaffold for a nanoclay–hydrogel composite ink.^[194] The addition of 6 wt% laponite nanoclay to poly(ethylene glycol) diacrylate (PEGDA) hydrogel produced a nearly twofold

increase in Young’s modulus. The increased stiffness allows the hydrogel to bridge horizontal gaps and form self-supported inclined planes with a maximum height of roughly 1.3 mm per 10° of inclination. This self-supporting behavior is due to the electrostatic interactions between laponite nanoclay platelets, which form a “house of cards” structure within the gel. As the hydrogel is extruded through a nozzle, fluid shear forces break up the nanoclay structure, reducing the effective viscosity. This shear thinning behavior allows the hydrogel to be extruded through smaller nozzles (1–250 μm ^[125]), then recover its high yield stress after extrusion. Other nonsupported hydrogel printing often requires rapid solidification. These methods are typically limited to temperature-sensitive, ultraviolet (UV) curable, and ion reactive hydrogels, although the range of 3D printed geometry is still limited by the low yield stress of the inks. Without rapid solidification or reinforcement, hydrogels are printed in a suspension bath. The addition of aligned nanoparticle reinforcement eliminates the need for both rapid solidification and suspension baths, allowing for a broader selection of printable hydrogels, as well as providing the ability to fabricate minute and closed geometry without supporting material.

In addition to imparting shape-changing and self-supportive behavior, shear-aligned nanomaterials can also be used for mechanical reinforcement. High particle loading is used to significantly increase mechanical properties and introduce anisotropy. However, higher nanoparticle loading increases yield stress, which can reduce the effect of shear alignment. In the viscous flow through a nozzle, fluid shear stress is highest at the walls and decreases to zero in the center of the flow. Within a fraction of the fluid cross-section, the applied shear stress is lower than the fluid yield stress. Inside this region, plug flow develops which diminishes the shear-induced alignment effect.^[195] For example, Siqueira et al. used DIW shear alignment to produce parallel alignment of 20 wt% cellulose nanocrystals (CNC) in an aqueous ink.^[114] After drying, the pure cellulose structures featured enhanced stiffness and a degree of orientation of up to 84%. Solid loading below 40 wt% was required to avoid plug flow. Siqueria et al. then developed composite monomer-CNC inks with 10 or 20 wt% cellulose nanocrystal loading and with brittle (M1) or soft (M2) matrices. Tensile testing showed improved strain hardening in the reinforced M1 matrix. 10 and 20 wt% cellulose nanocrystal loading increased the elastic modulus of M1 by 32% and 80%. In the M2 matrix, with 10 wt% loading, the tensile strength increased by 34% and 13% in the longitudinal and transverse loading, respectively, while the elastic modulus increased tenfold. This indicates an improvement in shear stress transfer between the long edge of the crystal and the surrounding matrix.

Fluid shear patterning can be used to modulate electrical functional properties. For example, polymers loaded with 2D graphene platelets (3–8 atomic layers thick, 5–20 μm wide) exhibit increased conductivity when printed with higher shear rates.^[53] Jakus et al. fabricated 3D scaffolds with high graphene content (60 vol% after deposition) using an ink composed of a polylactide-*co*-glycolide (PLG, 40 vol%) binder and dichloromethane solvent. The high graphene content produced higher electrical conductivity (875 S m^{-1}) than 3D printed carbon black constructs^[176,196] and exhibited higher ductility than samples with randomly aligned graphene platelets. It was

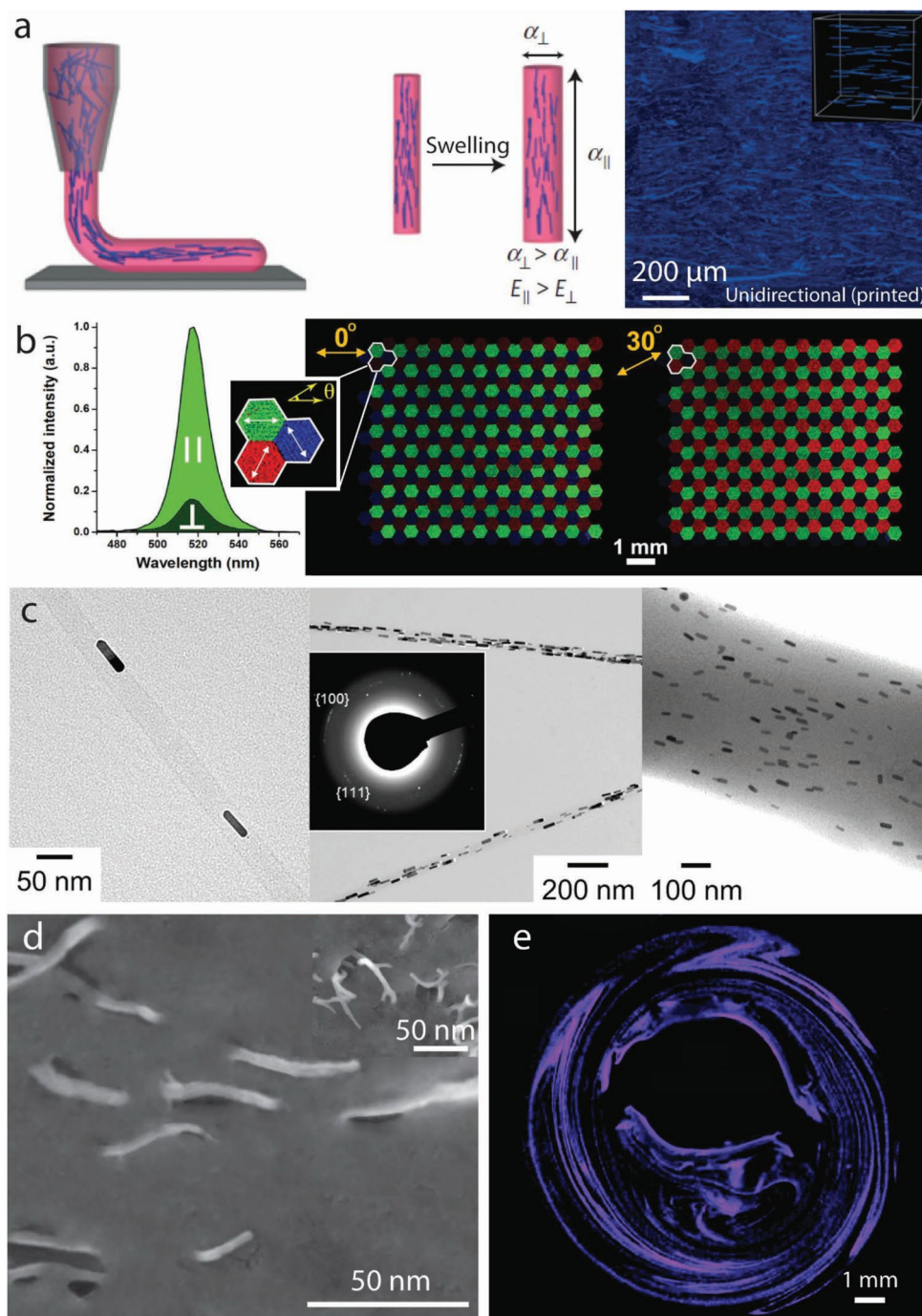


Figure 3. Fluid shear force-induced alignment of nanoparticles during 3D printing. a) Schematic of shear-induced alignment during direct ink writing (left). The anisotropic strain properties of the composite can be used to produce anisotropic swelling (center) and unidirectional cellulose fibrils in shear-induced alignment (right). Reproduced with permission.^[48] Copyright 2016, Nature Publishing Group. b) A pixel array composed of repeating hexagonal units (outlined in white) of lead halide perovskite CsPbBr_3 (green), $\text{CsPb}(\text{Br}_{0.2}\text{I}_{0.8})_3$ (red), and $\text{CsPb}(\text{Br}_{0.2}\text{Cl}_{0.8})_3$ (blue) nanowires with programmed emission angles. Emission intensity depends on the alignment between nanowires (white arrows) and the polarization angle of incident light (yellow arrows). When the polarization is parallel with a single nanowire orientation, the pixel array emits a single color of light (e.g., green). In contrast, when the polarization is aligned 30° with two nanowire orientations and perpendicular to the third, the pixel array emits two colors (e.g., green-red). Reproduced with permission.^[200] Copyright 2019, American Association for the Advancement of Science. c) Gold nanorods aligned within the electrospun polymer. Alignment within fibers of different diameters and concentrations (Left to right: 40 nm and 0.006 vol%, 50 nm and 0.045 vol%, and 650 nm and 0.035 vol%). Reproduced with permission.^[39] Copyright 2011, American Chemical Society. d) SEM image of aligned nanowires in a DLP printer, inset depicts randomly oriented nanowires before alignment. The alignment is performed within the resin tank. Reproduced with permission.^[190] Copyright 2016, IOP Publishing Ltd. e) Experimental result of chaotic printing, the mixing of two dissimilar fluids to create a pattern, matching closely with theoretical results. Reproduced with permission.^[210] Copyright 2018, The Royal Society of Chemistry.

also shown that the electrical conductivity can be maintained after hundreds of loading cycles and that the material does not break down when cut and sutured, demonstrating its possible use as a surgical medium. Further, in vivo experiments demonstrated the ability to maintain cell growth and nucleation within the implantation site without signs of inflammation or graphene accumulation in the filtration organs. After 30 days, the scaffold was integrated with the host tissue and new capillaries had grown into the implantation site, suggesting its potential use in biomedical implants.

Coupling electrical and mechanical anisotropy, fluid shear patterning with DIW can be used to introduce electromechanical anisotropy in piezoelectric nanocrystal-polymer hybrid materials. Due to the crystallographic structure of piezoelectric crystals, the magnitude of the electrical response is dependent on the direction of applied stress.^[197] Nafari and Sodano used DIW to produce a piezoelectric composite made of shear-aligned barium titanate nanowires suspended in polydimethylsiloxane (PDMS).^[198] An electromechanical model and experimental verification demonstrated that aligning the nanowires longitudinally with the applied stress can increase the electromechanical coupling up to 90% that of pure lead zirconate titanate (PZT-7A).^[199] While monolithic piezoelectric crystals have low fracture toughness, embedding the piezoelectric nanowires in a polymer produces a flexible composite that can be 3D printed to create resilient piezo force sensors with tailored shapes.

Fluid shear patterning can also be used to program optical functional properties. For example, DIW can be used to orient nanowires to program an optical response to polarized light. Zhou et al. programmed the alignment of cesium lead halide (CsPbX_3 , $X = \text{Cl, Br, and I}$) nanowires with a perovskite crystal structure to form polarized optical architectures.^[200] The ink consisted of perovskite nanowires suspended in a polystyrene-polyisoprene-polystyrene (SIS) block copolymer matrix. The shear flow within the DIW extrusion causes the SIS to form longitudinal hexagonal domains smaller than 50 nm in diameter. As the alignment and local dielectric environment of the nanowire dictates the angular emission pattern of the nanowires, different regions of the structure can be programmed to emit colored light when excited by UV light with a particular polarization angle. For example, Zhou et al. fabricated a red-green-blue (RGB) color display as shown in Figure 3b. The tri-hexagonal pixels consist of perovskite nanocrystals with different chemical compositions: CsPbBr_3 (green), $\text{CsPb}(\text{Br}_{0.2}\text{I}_{0.8})_3$ (red), and $\text{CsPb}(\text{Br}_{0.2}\text{Cl}_{0.8})_3$ (blue). When aligned unidirectionally, the lead halide films act as polarized photon downshifters (Figure 3b, left). The three lead halide films in each pixel unit are oriented 60° apart, enabling selective color emission by varying the polarization of incident UV light. When the angle of polarization of the excitation light source is parallel with one of the nanowire orientations, the pixel array's emission spectra is that of a single color—green, in the case of Figure 3b, center. When the angle of polarization of the excitation light source is 30° between two nanowire orientations, the pixel array's emission spectra is a combination of the two corresponding colors—green and red, in the case of Figure 3b, right. This demonstrates the ability to leverage fluid shear patterning to program the emission spectrum of an active RGB color display by modulating the orientation of perovskite nanowires.

Fluid shear patterning can also be leveraged in electrospinning to achieve longitudinal alignment of nanofibers and nanorods in a filament with sub-micrometer diameter. In electrospinning, the tangential electric shear stress acting on the surface of the charged fluid jet causes the velocity profile to invert; the maximum fluid velocity resides at the surface of the stream.^[201] Roskov et al. used this phenomenon to align gold nanorods (GNR) within an electrospun polymer to produce nanofibers (40–3000 nm diameter) with an absorbance spectrum that is responsive to the polarization angle of the incoming light.^[39] At low volume fraction (0.6–3.5 vol%), the diameter of the spun fiber has the greatest impact on the GNR alignment as shown in Figure 3c. Larger diameter fibers exhibit less extreme local velocity profiles, allowing the GNR to have greater angular deviation; a diameter of 3 μm produces an angular deviation of 13.3° . In contrast, a smaller diameter of 40 nm produces an angular deviation as low as 3.8° . Further, the use of electrospinning allows the diameter of the extruded filament to be adjusted on-the-fly, which can be used to tailor the absorbance of polarized light by adjusting the angular deviation of GNR as well as the printing direction.

Fluid shear patterning has been primarily incorporated into extrusion 3D printing methods where a continuous, laminar flow of fluid is used to align nanorods. Interestingly, fluid shear patterning can also be achieved with lateral oscillations or continuous rotation in “bulk” resin-based 3D printing methods. This approach to nanomaterial patterning in bulk methods has several attractive attributes. For example, in contrast to an acoustic patterning approach,^[44,202,203] bulk fluid shear patterning can overcome the misalignment challenges that arise from high particle concentration.^[204] In contrast to magnetic patterning,^[29,30,42,77,205] this approach does not require magnetic particles or magnetic fields. Specifically, a “linear harmonic oscillator mechanism” can be joined to the resin reservoir of a stereolithography (SLA) printer. The linear oscillation of the reservoir produces a harmonic shear rate profile within the thin layer of resin between the bottom of the reservoir and the stationary build platform. The width of the channel introduces different alignments in the “core layer” and “skin layer.” In the “skin layer” (a region of fluid close to the surfaces) nanowires orient parallel with the channel. In the “core layer” (a region of fluid at the center of the channel) nanowires orient perpendicular to the channel. The core layer can be eliminated by reducing the thickness of the channel below 200 μm ^[206,207] and maintaining a sufficient shear rate.^[208,209] For example, Yunus et al. developed a method in which a resin tank is subjected to linear oscillation to align all constituent nanowires in a single sheet (Figure 3d).^[190] The maximum shear rate affects the fiber orientation tensor, with a higher shear rate ($\geq 200 \text{ s}^{-1}$) producing more aligned fibers ($\approx 80\%$ parallel). The oscillation frequency and nanowire loading (1–5 wt%) had a negligible effect. As the shear rate and the thickness of the channel affect the regional alignment of nanowires, future study could explore the fabrication of unique heterogeneous composites with a tank of nonuniform geometry.

In addition to manipulating the orientation of nanoparticles, fluid shear patterning has achieved the patterning of particle locations in bulk printing with a so-called “chaotic printing” approach.^[210] Specifically, Trujillo-De Santiago et al. used a

circular tank with an intersecting eccentric cylindrical shaft (resembling a journal bearing) to produce complex mixing patterns of nanoparticles deposited in the tank. The authors demonstrated the ability to print concentric lamellar structures, modeled theoretically with Navier–Stokes equations, as shown in the nanoscale striations in Figure 3e. As the reaction rate can be controlled by modifying the thickness and the number of alternating layers within the structure, this approach can potentially be used to create high-performance catalytic surfaces^[211,212] and cell interaction studies.^[213,214] This method can also be used to create composites with densely packed interfaces, improve tissue regeneration,^[215] and form dense hollow matrices.

In summary, fluid shear patterning leverages shear stresses developed in the flowing ink to program the orientation of anisotropic nanomaterials during a 3D printing process. This approach can be readily integrated with extrusion-based printing methods such as DIW to impart functional properties. While uncommon, this approach can also be extended to bulk resin-based 3D printing by using a unique mechanism such as linear harmonic oscillation or “chaotic printing.” In comparison to other nanomaterial patterning approaches (e.g., magnetic patterning), fluid shear patterning is compatible with a broader range of materials such as cellulose, hydrogels, silicone polymers, gelatin, metallic and ceramic nanorods, and biological cells. This versatility allows the programming of a wide range of constructs and has been demonstrated to produce shape-changing structures, modulate mechanical properties, and impart tunable optical and electrical properties. Indeed, fluid shear patterning allows seamless integration of functional properties to create highly integrated, unique, and multifunctional devices and architecture in a 3D printing process.

6. Evaporative Patterning

“Evaporative patterning” describes patterning approaches that leverage the multiphase interactions between solutes, solvents, substrate, and the microenvironment in an evaporation process to drive the assembly of nanomaterials, with the ultimate goal of generating the desired microstructure. This is typically a complex and dynamic phenomenon that is associated with van der Waals interactions, electrostatic interactions, hydrogen bonding, and surface free energy.^[216] Literature has demonstrated the usage of evaporative patterning to generate a wide range of features: from thin films^[217,218] to high aspect ratio colloidal structures.^[219] For example, in thin films, a myriad of patterns ranging from the so-called “coffee-ring,”^[220] worm-like domains,^[221–223] cellular and lamellar structures,^[224,225] sawtooth patterns,^[225,226] to a uniform monolayer^[227] have been generated, even in a confined construct.^[228] For high aspect-ratio structures, a wide range of architectures has been fabricated, such as 3D freestanding structures,^[229] microwires,^[230] nanoarches,^[45] “joint” structures,^[46] and dome structures.^[231] Significantly, the microstructure can be modulated by a wide range of properties, including—but not limited to—the volume fraction of the nanomaterials in the ink, polydispersity,^[232] surface properties of nanomaterials,^[233–235] surface free energy of the substrate,^[236,237] ink composition,^[238] and by

controlling environmental parameters such as pressure^[239] and temperature.^[240]

Evaporative patterning is predominantly driven by directed assembly processes that leverage interparticle forces, friction forces, and fluid flows to pattern nanomaterial assembly. In contrast to transfer printing,^[241,242] such as stamping^[243,244] or atomic force microscopy,^[245] evaporative patterning can drive nanomaterial assembly without additional tools. This template-free and lithography-free patterning approach can be readily integrated with a wide range of extrusion-based 3D printing technologies. The ability to generate distinct features by modulating the ink and printing parameters is particularly attractive as an approach to enhance the versatility of 3D printing to create functional architectures.

We note that the “directed assembly” process is distinct from what is observed and described as “self-assembly.” Specifically, self-assembly is a complex process where noncovalent interactions, such as van der Waals attraction, steric repulsion, and charge attraction, cause molecular or mesoscale components to spontaneously organize into a quasi-stable structure.^[41] In self-assembly, the particles interacting with each other form patterns based on their local interactions without any external agents dictating the formation of the pattern.^[237] As described by Whitesides and Grzybowski, self-assembly is commonly observed in nature during the creation of multidimensional biological structures such as cells.^[216] Other examples include the one-dimensional (1D) assembly of peptides,^[246] proteins, and nucleic acids.^[247] In contrast, directed assembly, also known as “self-organization,” is described as a process where the nanomaterial’s assembly^[237] is driven with external forces or fields such as electric fields^[248] or magnetic fields.^[249,250]

The ability to control the nanomaterial assembly process requires an understanding of multiphase dynamics and soft matter physics. For example, the so-called “coffee-ring” phenomenon describes a ubiquitous observation where dried colloids are concentrated at the boundary of the droplet area rather than deposited uniformly across the surface. This is because when a droplet evaporates, microscopic physical and chemical irregularities in the substrate can pin the boundary (or “contact line”) between the wet and dry substrate. This will result in a nonuniform curvature of the droplet.^[224] As the contact line is pinned, the evaporation rate at the edge of the droplet increases, resulting in an increase in the outward capillary fluid flow.^[220] This capillary flow will draw the solutes by advection and cause nanoparticle deposition at the edge of the contact line.

Evaporative patterning can be used to control nanomaterial deposition patterns in 3D printed colloids through the introduction of nonequilibrium dewetting processes. **Figure 4a**, right, shows the incorporation of a binary solvent mixture, which can introduce a Marangoni effect^[251–253] due to the differential surface tensions associated with two liquids in the mixture. This can induce a compensating flow towards the center of the printed droplet. For example, quantum dot (QD) solutions with a binary mixture of toluene and dichlorobenzene^[40] yield a microstructure with greater uniformity than those with a solution of pure toluene (Figure 4a, left). Another example of an approach that can reduce the coffee-ring effect is the depinning of the three-phase contact line. For example, by treating silicon and polydimethylsiloxane (PDMS) with plasma,

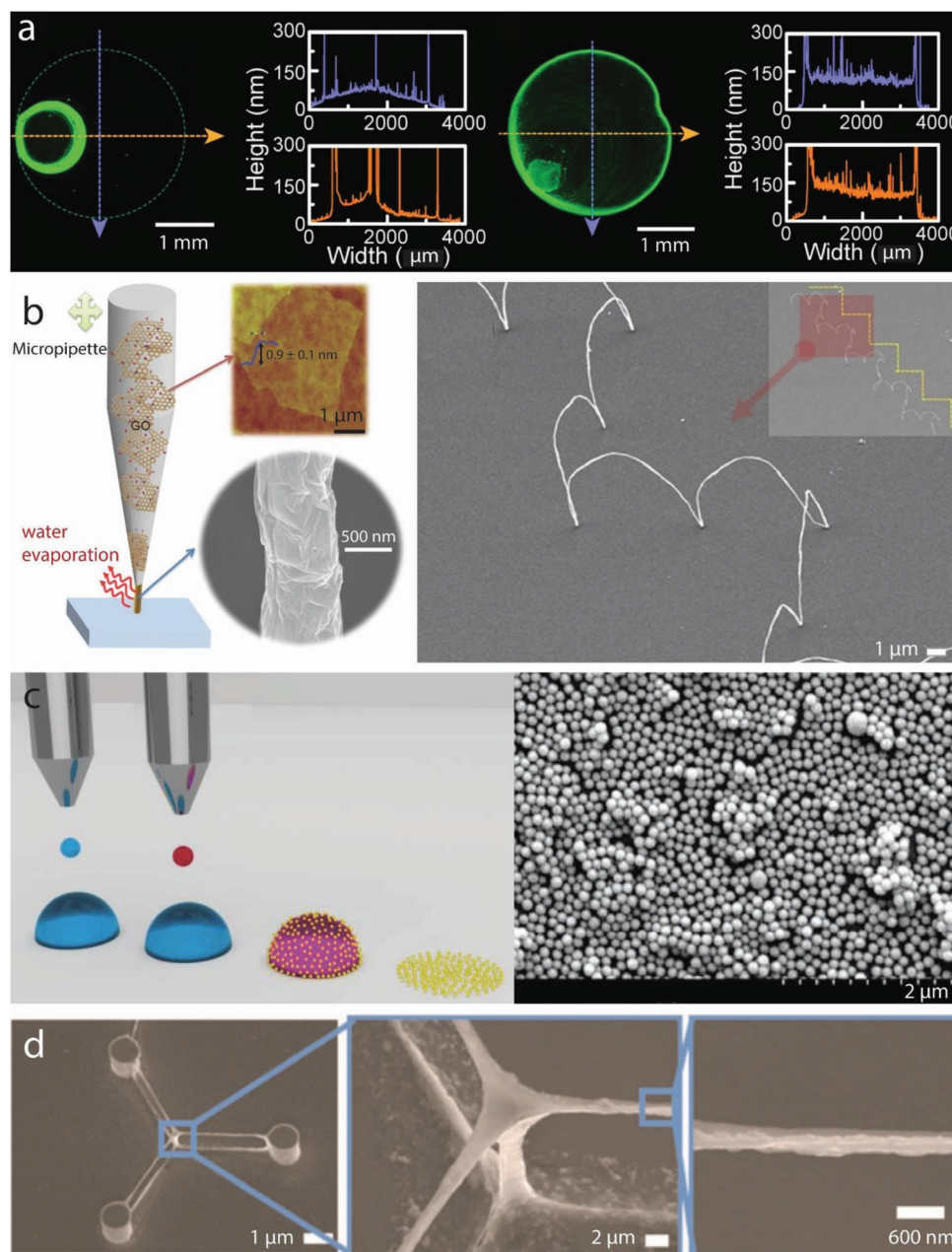


Figure 4. Evaporative patterning of nanoparticles. a) Ink composition is important in printed nanomaterials. For example, 3D printed quantum dots (QDs) with a single solvent formed highly nonuniform "coffee-ring" features (left). In contrast, the uniformity of the printed QDs is significantly improved with the addition of cosolvent (right). Graphs show the profilometry measurements of the QD deposition in two perpendicular directions (blue and orange arrows and graphs). Reproduced with permission.^[40] Copyright 2014, American Chemical Society. b) The interface between a substrate and the meniscus formed at a nozzle tip can be used to control solvent evaporation. Graphene oxide (GO) sheets are patterned into nanowires using the meniscus formed at the tip of a micropipette (left). Inset shows the atomic force microscopy image (AFM) of graphene oxide sheets and the scanning electron microscopy (SEM) image of a nanowire. Nanowires can be patterned spatially, as demonstrated by the zigzagging, reduced graphene oxide (rGO) nanoarch with a constant arch width of 400 nm (right). Reproduced with permission.^[45] Copyright 2015, Wiley-VCH Verlag GmbH & Co. KGaA. c) A dual droplet process can be used to produce a nearly uniform, closely packed deposition of polystyrene nanoparticles (gold) of nearly single-layer thickness, where a high surface tension solvent (blue) is used as a supporting droplet, and a low surface tension solvent (red) is used as a wetting droplet (left). SEM image shows sulfate-functionalized polystyrene nanoparticles deposited on polyethylene terephthalate (PET) substrate with a wetting droplet composition of 50 wt% ethanol/water-diluted ink (right). Reproduced with permission.^[78] Copyright 2018, Wiley-VCH Verlag GmbH & Co. KGaA. d) Assembly of nanomaterials can be guided with a pre-designed template to drive the shape-shaping process via surface minimization in an evaporative process. SEM image shows the side view of triangular structures formed from silver nanoparticles. The inset shows the flow of liquid from the face into the adjacent edge. The zoomed-in images (blue border) shows the details of the assembled "joint" structure of assembled nanoparticles. Reproduced with permission.^[46] Copyright 2017, Wiley-VCH Verlag GmbH & Co. KGaA.

polystyrene, acids, or organic compounds, Song and co-workers created substrates with high receding contact angles.^[231] The three-phase contact line starts to slide over the substrate when it exceeds a critical value of the receding contact angle. The particles are directed inwards when the force acting on the particle by the sliding three-phase contact angle exceeds the adhesive force between the substrate and particles. This can mitigate the coffee-ring phenomenon, which Song and co-workers demonstrated by assembling polystyrene nanoparticles to form a range of microstructures from flat disks to dome structures with an increasing height to diameter ratio.^[231] In addition to counter-acting the coffee-ring effect, nonequilibrium dewetting processes can be leveraged to produce a plethora of patterns through the modification of factors such as nanoparticle concentration in the ink, the solvent used to form printable ink, method of deposition, and the free surface energy of the substrate.^[237] For example, isolated islands,^[254–256] worm-like domains,^[257] interconnected cellular networks with continuous labyrinthine structures,^[258–261] and ring structures^[262–264] have been reported with gold, latex, and silver nanoparticles.

Analytical modeling, as well as numerical simulation, of nonequilibrium dewetting processes is able to provide insights to examine the dependence of evaporative pattern formation on liquid–liquid, nanoparticle–nanoparticle, and nanoparticle–liquid interactions, as well as chemical potential.^[237] For example, Ge and Brus^[265] and Rabani et al.^[266] devised a Monte Carlo model to simulate the 2D assembly of nanoparticles mediated by the drying process, accounting for solvent fluctuations. The model can reproduce a wide range of morphologies due to its sensitivity to parameters such as vapor pressure, density, and temperature. Subsequent work has demonstrated the ability to simulate nanomaterial assembly for the study of relatively complex deposition phenomena, such as binary mixtures of nanomaterials,^[267,268] interactions on a patterned substrate,^[269,270] multimodal patterns^[261] and 3D behavior.^[254,271] Zhang et al. used the Kinetic Monte Carlo approach to investigate the formation of branched aggregates from a sessile nanofluid droplet by assuming that the chemical potential is a function of time and radius of the droplet.^[272] They found that the shrinking velocity of the contact line is faster at the early stage in a drying process. Recently, Hao et al. simulated evaporation-assisted assembly in block copolymers using volumetric lattice Monte Carlo simulations.^[273] In particular, they studied the influence of the solvent selectivity, surface preference, and the rate of evaporation, which influences the film morphology. It was found that the tendency of the formation of perpendicular cylindrical morphology is enhanced when there is strong solvent selectivity.

In addition to patterning 1D nanomaterial patterns in sessile droplets, evaporative patterning can be used to drive the formation of high aspect ratio structures through several strategies. For example, a meniscus formed at the tip of a nozzle or pipette can be used to create architecture with aspect ratios as high as 220. Specifically, freestanding reduced graphene oxide (rGO) nanowires as small as 150 nm in diameter have been 3D printed using a meniscus formed at the tip of a micropipette puller.^[45] The balance of surface tension and gravity forms a meniscus containing graphene oxide (GO) (thickness 0.9 ± 0.1 nm), which is pressed to the substrate. The tip is withdrawn to increase the surface-to-volume ratio as there

is a decrease in the cross-sectional area of the meniscus. This promotes the rapid evaporation of water, allowing the creation of structures without supporting material.^[45] After printing the GO wires, the structure can be either thermally reduced or chemically reduced by treatment with hydrazine. Figure 4b (right) shows the rGO zigzag freeform architecture that can potentially form 3D interconnects for microchips.

Evaporative patterning can also be used to produce uniform depositions of nanomaterials. The coprinting of supporting and wetting droplets has been demonstrated to improve the uniformity of particle deposition, which can modulate the assembly of nanoparticles at the interface between droplets.^[78] In this strategy, first, a solvent with high surface tension is printed to form a “supporting droplet,” followed by a nanoparticle colloid containing solvent with lower surface tension to form a “wetting droplet.” Figure 4c, left, shows the spreading of a wetting droplet (red) on a supporting droplet (blue), producing a uniform deposition of polystyrene nanoparticles (gold). The spreading of the wetting droplet on the supporting droplet creates a surface tension gradient, which creates a Marangoni flow that traps the nanoparticle film on the surface of the supporting droplet. The nanoparticles assemble into islands due to particle–particle interactions and subsequently form a nearly uniform monolayer after the evaporation process. Figure 4c, right, shows such a uniform film, composed of polystyrene nanoparticles (100 nm). Interestingly, it was shown that smaller particles (100 nm) show some order of overlapping while larger particles (300 nm) showed more ordered assembly. This is likely due to the greater influence of van der Waals interactions on smaller particles, which increases the tendency to form agglomerates.

Evaporative patterning can be integrated with mechanical templates to guide the assembly of particles into 3D nanomaterial structures through the minimization of surface free energy. For example, Su et al. used a so-called “3D self-shaping strategy” to create a wide range of 3D assemblies of organic and inorganic nanomaterials. Specifically, a colloidal nanomaterial solution was printed over a substrate patterned with micropillars.^[46] As the solvent evaporated, the three-phase contact line was pinned by the pillars, forming 3D architectures dictated by the patterns in the template. Using this method, Su et al. were able to print silver nanoparticles in triangular, tetragonal, pentagonal, and hexagonal patterns (Figure 4d), tens of micrometers in size (60–80 μm).^[46] They also demonstrated the capability of this process to create micro and nanostructures with electrical conductivity and fluorescence properties. These structures can be used to create 3D circuits and fluorescent displays. In another example, Li et al. have demonstrated the creation of highly aligned deoxyribonucleic acid (DNA) nanowires up to 1.6 mm long by inducing an aqueous solution of λ -DNA to evaporate between a flat substrate and a curved or cylindrical lens.^[274] The DNA forms patterns resembling branched bicycle spokes, straight spokes, or planar bands controlled by microenvironment parameters such as temperature and pH during the evaporation process.

Evaporative patterning can also be used to create 3D macro-scale structures with tunable optical properties. For example, structures with reflectance spectra ranging from violet to red can be obtained by modulating the arrangement of colloidal crystals.^[275,276] The arrangement is modulated by changing the

size of the constituent particles and tailoring the packing of the nanomaterial assembly. Tan et al. used DIW of a colloidal solution of polystyrene, silica, and gold nanoparticles to fabricate macroscale freestanding structures.^[219] Initially, the nanoparticle suspension was dispensed to form a liquid bridge of $\approx 200\ \mu\text{m}$ between the substrate and nozzle. The micrometer-sized bridge acts as a confinement space for the particles to assemble at its bottom, allowing structures with high aspect ratios (≈ 10) to be fabricated. This approach is compatible with a wide range of particle sizes (radius $\geq 1\ \mu\text{m}$ for polystyrene, $\approx 200\ \text{nm}$ for silica, and $\approx 50\ \text{nm}$ for gold). However, the particle size must be optimized to ensure no sedimentation occurs. For example, larger particles precipitate more readily, which prevents long-range ordering, while smaller particles were observed to produce a more organized assembly. This capability to direct-ink writing high aspect ratio structures is an attractive method to fine-tune the optical properties of 3D microstructures via the change of the size and composition of the particles. For example, freestanding colloidal structures with the ability to reflect violet, blue, green, and red light, with polystyrene particle radius of 95, 105, 110, and 140 nm respectively, were demonstrated.

In summary, evaporative patterning is a highly versatile nanomaterial patterning technique that can generate a wide range of thin-film patterns, high aspect-ratio structures, and freestanding architectures. It is an attractive method to fabricate architectures with tunable functional properties without the requirement of additional transfer substrates or stamps. This is achieved by leveraging different control methods, including the introduction of binary solvents to induce Marangoni flow, substrate modification, meniscus-guided printing, coprinting of supporting and wetting droplets, and templated 3D self-shaping strategies. The fabrication of freestanding structures is also possible with direct writing of a colloidal solution by controlling the growth of colloidal structures with respect to the evaporation rate. Such a patterning approach is an attractive method to fabricate structures with tunable optical functionality by merely varying particle size. Fundamentally, evaporative patterning is achieved with the understanding of multiphase dynamics and soft matter physics such as evaporation kinetics and drying of colloidal solutions. Understanding the drying of colloids and evaporation kinetics can improve the ability to control the morphology and assembly of nanomaterials and ultimately lead to functional nanodevices. While current work has demonstrated analytical models, numerical simulations, and the fabrication of diverse structures, it has yet to realize macroscale, defect-free structures. This is limited by the inability to fully mitigate defects caused by phenomena such as the coffee-ring effect and agglomeration in the nanomaterial assembly. Further, the ability to fabricate hierarchical structures ranging from the nanoscale to the microscale, as seen in nature, is generally limited by the resolution of a 3D printing method. For further reading, the reader is referred to several excellent reviews which highlight the latest understanding of the assembly of nanomaterials during an evaporation process.^[277–282]

7. Acoustic Patterning

“Acoustic patterning” refers to the organization of particles dispersed in a fluid medium through the application of acoustic

energy.^[99] Acoustic radiation forces generated by the acoustic waves transfer momentum to the particles and fluid. This transfer depends upon the physical characteristics of the particles such as density, compressibility, and size, as well as the properties of the fluid.^[283] The pattern of pressure nodes in an acoustic field will drive particle assembly based on the relationship of density and compressibility between the dispersed particles and the fluid medium.^[203,284] Acoustic patterning is applicable to a broad range of materials. In contrast to patterning techniques such as electric field-assisted patterning and magnetic field-assisted patterning, acoustic patterning does not require particles to be electrically conductive or possess magnetic properties.^[99]

Acoustic patterning in 3D printing has been used to create conductive microstructures,^[44] nanoparticle–polymer composites,^[203] and to transport domain walls in nanowires.^[285,286] Literature has also demonstrated the ability of acoustic patterning to pattern nanomaterials in unidirectional features, such as parallel lines,^[44] and heterogeneous features, such as curves and crisscross patterns.^[202,203]

Most acoustic patterning methods harness acoustic tweezers^[287,288] to pattern an assembly of nanomaterials. Acoustic tweezers are a versatile set of tools that are used to manipulate, localize, or concentrate the distribution of particles using the interaction between acoustic waves and the surrounding solid, liquid, or gaseous media.^[287] When an ultrasound field is directed through a particle dispersion, an acoustic radiation force emanates from the scattering of waves from the particles.^[289] This force depends upon the size and position of the particles, as well as the energy associated with the wave.^[290] More specifically, the acoustic force is positively affected by increases in particle volume, particle density and speed of sound in the particle, as well as decreases in fluid density and speed of sound in the fluid, as described with the equation

$$F = kVE_{\text{ac}}\phi \sin(2kx) \quad (1)$$

where k is the wavenumber, V is the particle volume, E_{ac} is the acoustic energy density, ϕ is the acoustic contrast factor, and x is the position of the particle on the x -axis.^[291]

The resulting pattern is influenced by a property of the dispersion known as “acoustic contrast.” Acoustic contrast describes the relationship between the density and compressibility of the fluid and dispersed solid. The acoustic contrast increases with greater particle density and speed of sound, and it decreases with greater fluid density and speed of sound. The sign of the acoustic contrast factor often dictates where the particles will be driven.^[290] When the acoustic contrast factor is positive, the particles migrate toward pressure nodes (displacement antinodes), and when it is negative, the particles move toward pressure antinodes (displacement nodes).

The most common types of acoustic tweezers—standing-wave tweezers—can be divided into two subtypes based on the waves they generate: bulk acoustic waves (BAWs) and surface acoustic waves (SAWs). Typically, lateral vibration of a piezoelectric ceramic element is used with a resonator to generate BAWs and manipulate particles. The resonant frequency of BAWs is under 10 MHz; such waves manipulate particles suspended in a relatively large fluid medium. On the other hand,

SAWs oscillate in the range of tens to hundreds of megahertz, localized to the surface of the element. They are often generated by patterned interdigitated transducers (IDT), which expand and contract a piezoelectric material.^[287,292] This continuous deformation generates SAWs that propagate along the longitudinal and transverse directions. Waves vibrating at higher frequency have a shorter wavelength rendering them suitable for attaining superior spatial resolution.^[292] For instance, the frequency of SAWs vibrating at 100 MHz corresponds to a wavelength of less than 100 μm , making them desirable for higher resolution patterning. It has been shown that higher frequency acoustic waves can be used to precisely pattern cells and nanoparticles.^[287,293–297] Wu demonstrated the use of acoustic tweezers to trap latex microparticles and clusters of frog eggs in a potential well (regions of minimum potential energy) generated by two collimated, focused ultrasonic beams.^[298] Subsequently, acoustic tweezers have been used in the fabrication of polymer composites,^[299] microparticle collection,^[300] cell-patterning,^[288] single-molecule analysis,^[301] and printing of electronic components.^[44]

When designing an acoustic patterning system, it is vital to consider the range of particle sizes that can be manipulated at a given pressure amplitude. Moreover, analytical models that account for interparticle interactions and secondary acoustic radiation forces could predict the limit of particle size that can be manipulated acoustically. Reyes et al. analytically and experimentally investigated the size limit of gold nanoparticles that can be focused on a fluid using ultrasonic radiation forces.^[291] It was shown experimentally that the distribution of larger particles (100–200 nm) features a narrow full width at half-maximum (FWHM) (43.2–25 μm) and smaller sized particles (60 nm) exhibit a wider distribution, with an FWHM of 140 μm under 700 kPa. This is because the acoustic radiation force is proportional to the volume of the particle. Thus, larger particles experienced a greater magnitude of force. Furthermore, Brownian motion is more pronounced in smaller particles. This often inhibits focusing smaller particles, resulting in a wider FWHM. Reyes et al. extended this observation to polystyrene and silica nanoparticles, concluding that the FWHM of the distribution of the nanoparticles decreased as the acoustic contrast factor, pressure amplitudes, and size of the nanoparticles increased.^[291] With this knowledge, an acoustic field-assisted nanomaterial patterning system can be designed to target certain particle size ranges.

With the ability to pattern regional distributions of nanomaterials, acoustic patterning has been used to construct composites with heterogeneous electrical conductivity. Fabrication of polymer composites with electrical signal transmission capability is especially important for printed electronics, optoelectronic devices,^[302] sensors,^[303] and wearable technology.^[304] Yunus et al. incorporated hexagonal acoustic tweezers with a DLP printer to align nanoparticles and print parts with embedded conductive microstructures.^[44] A low-viscosity photocurable resin was subjected to BAWs generated by two piezo plates located opposite to each other in the hexagonal tweezer. Since the BAW affects the entire resin reservoir, selective photocuring is used to produce a spatial variance in nanoparticle patterning. Once the pattern is formed, the region is cured, and the BAW is relaxed, allowing uncured regions to

form uniform dispersions before photocuring. Different weight fractions (0.0–9.0 wt%) of carbon nanofibers of outer diameter (OD) 200–600 nm, copper nanoparticles (OD 300 nm), and magnetite nanoparticles (OD 300 nm) reinforcements were used to produce electrically conductive samples (Figure 5a, bottom left). It was found that the resistivity of the patterned samples was 13–15 times lower than those without acoustic patterning. This decrease in resistivity was attributed to the loss of contact between the layers patterned with particles. Figure 5a, bottom right, shows an embedded zig-zag pattern, produced by stacking eight layers of acoustically aligned nanoparticles and insulating resin. This stacking results in two insulated, separate conductive wires that cross over each other. In this way, the acoustic patterning technique has been shown to be a promising technique to fabricate microstructures with embedded electrical functionalities.

Acoustic patterning approaches can be leveraged to fabricate particle–polymer composites using nanoparticles as mechanical reinforcement agents. In bulk printing methods, particles can be dispersed in a fluid or resin and patterned using acoustic waves, which are transmitted through the entire resin reservoir. Introducing a novel method to pattern anisotropic particles, Llewellyn-Jones et al. used SAWs to fabricate composite structures of glass fibers (14 μm diameter and 50 μm length) dispersed in SPOT-A (registered product of Spot-A Materials) resin.^[305] It was anticipated that the anisotropy gained after particle manipulation could lead to enhanced mechanical strength in the composites. Later work applied similar strategies to anisotropic nanoparticle reinforcement, advancing the study of acoustically patterned nanocomposites. For example, Greenhall et al. embedded 10 wt% carbon nanotubes in urethane resin and used ultrasound to pattern nanocomposites with enhanced mechanical strength.^[306] Nanocomposites with multiwalled carbon nanotube reinforcement (weight fraction <2.5%) had a 40% higher ultimate tensile strength as compared to the ultimate tensile strength of virgin polymer material. In a similar approach, Lu et al.^[202] used acoustic field-assisted projection stereolithography (A-PSL) to pattern microscale structures. In A-PSL, particles are premixed in a resin vat, while embedded piezo elements generate acoustic waves. The particle pattern for each layer is defined in a digital model. The pattern is subsequently fixed by digital photolithography images, and the process is repeated for each layer. It is possible to program the local composition and the externally applied field to obtain a heterogeneous particle–polymer composite. Lu et al. used tungsten nanoparticles (70 nm) mixed in a SPOTE (registered product of Spot-A Materials) elastic resin to fabricate heterogeneous polymer composites.^[202] Various patterns such as parallel lines, concentric curves, a grid of crisscrossing lines, and a grid of crisscrossing curves were generated. It was found that the rectangular piezo plates form parallel lines (Figure 5a), while round piezo disks form concentric curves (Figure 5b). The ability to print parts with heterogeneous particle distribution could lead to the fabrication of composites with complex reinforcement patterns. For example, dense grids of nanomaterial reinforcement could serve as crack inhibitors, while programming the direction and density of reinforcement could tune mechanical anisotropy and steer crack propagation.^[29,307–310] This level of precision could lead to the fabrication of architecture with tunable microstructures of high geometric complexity.

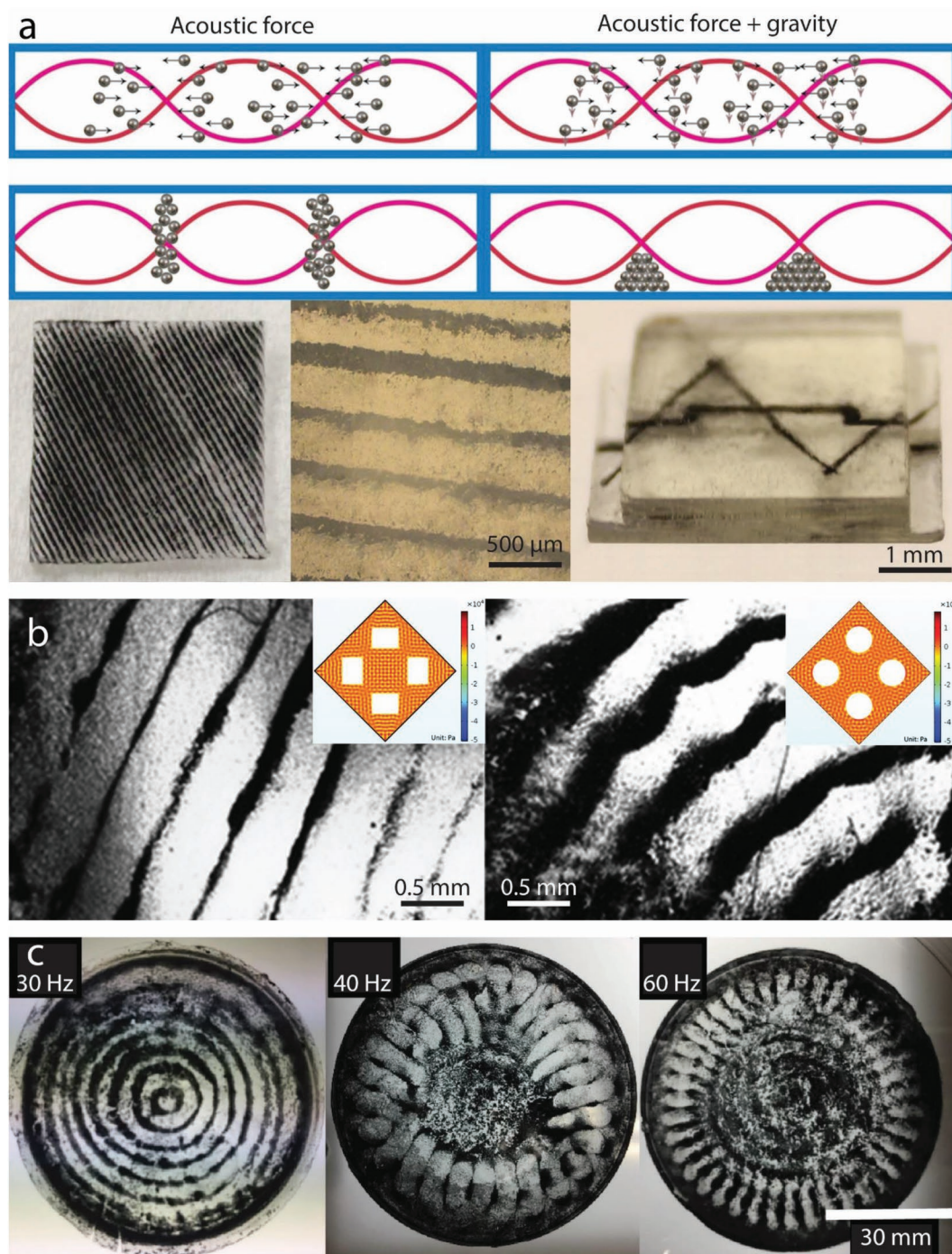


Figure 5. Acoustic patterning of nanoparticles. a) Acoustic forces can align nanoparticles in a polymer matrix to fabricate structures with embedded conductive elements. The top left image shows the patterning of nanoparticles using bulk acoustic waves (BAWs), while the top right image shows the pattern under the influence of both acoustic and gravitational forces. The center image is a micrograph of aligned copper nanoparticles. The bottom left image shows unidirectional patterning of magnetite particles at an angle of 60° ; the bottom right image shows an embedded zig-zag stitch wire pattern of electrically conductive copper nanoparticles. Reproduced with permission.^[44] Copyright 2017, IOP Publishing Group. b) Acoustic field-assisted projection stereolithography can be used for the fabrication of particle–polymer composites. The left image is a micrograph of tungsten nanoparticles (black) embedded in a polymer matrix of SPOT-E elastic resin, patterned in parallel lines. Inset shows the numerical simulation of acoustic pressure field patterns produced by piezoelectric plates. The right image is a microscopic image of the particles in concentric curves, and the inset image shows a simulation of the acoustic pressure field. Reproduced with permission.^[202] Copyright 2018, Mary Ann Liebert, Inc. c) Pressure waves produced by a vibrating substrate can pattern nanoparticles in a fluid medium. The images from left to right show patterns generated with iron oxide nanoparticles in a poly(ethylene glycol) diacrylate (PEGDA) hydrogel solution at the vibrational frequencies of 30, 40, and 60 Hz. Different vibration frequencies achieve different patterns. Reproduced with permission.^[203] Copyright 2018, Elsevier Ltd.

Acoustic patterning can also be achieved through the physical vibration of a substrate. This approach excludes the direct use of acoustic tweezers—the particle assembly is driven by the formation of 2D SAW. Shabaniverki et al. demonstrated the ability of the vibration-driven assembly to align particles in an area as large as 3000 mm².^[203] The acoustic radiation force and vibrational fluid flow create localized displacement nodes and anti-nodes as well as localized shear rates. Glass microparticles (150–212 μm) migrated to displacement anti-nodes, whereas iron oxide nanoparticles (50–100 nm) migrated toward the displacement nodes of the SAW. At 30 Hz, the fluid's viscous drag inhibits the transport of relatively large microparticles (200 μm), while the movement of nanoparticles is dominated by the flow of displaced fluid. Figure 5c shows the heterogeneous patterns formed by the iron oxide nanoparticles at vibrational frequencies of 30, 40, and 60 Hz. It was also shown that the nanoparticles are sensitive to lower frequencies (30–60 Hz), but beyond 60 Hz, there was no apparent change in the generated patterns.

Acoustic patterning can also be used to influence the magnetic microstructure of ferromagnetic materials, which could be coupled with magnetic patterning to create a novel nanomaterial patterning method. A novel method for the remote actuation of memory and communication devices used an acoustic waveform to create an array of domain wall pinning sites within a ferromagnetic nanowire.^[286] Racetrack memory devices make use of the orientation of magnetic domains in a ferromagnetic nanowire to store data.^[311] Dean et al. have demonstrated that by applying small shifts to the frequency of the acoustic transducers, multiple domain walls can be transported through nanowires.^[286] They reported that the domain walls are attracted to and then pinned at the antinodes of standing acoustic waves due to ratcheted motion toward positions of lower stress gradients.^[286] This ability to manipulate domain walls with high speed could potentially advance the development of “racetrack” memory devices.^[285]

Additionally, the acoustically driven, remote actuation of magnetic domains could be used to augment magnetic patterning in the production of 3D printed composites. A key area of study in magnetic patterning is the use of local magnetic gradients to produce nonuniform reinforcement alignment and particle distributions.^[77,205] Acoustic patterning may enable fine control over magnetic gradients, thereby providing a method for the fabrication of smart structures with intricate magnetic response programming and magnetic actuation abilities.^[49,312,313]

In summary, acoustic field-assisted patterning offers a promising method for the scalable, contact-free assembly of nanoparticles in a 3D printed structure. This approach is highly versatile, with the ability to generate a wide range of patterns—from the unidirectional alignment of nanomaterials to complex heterogeneous patterns wherein the particles are arranged to form microstructures with anisotropic functional properties. This is achieved by incorporating acoustic tweezers or direct substrate vibration to produce a patterned waveform in a 3D printing process. Fundamentally, acoustic patterning requires an understanding of the complex interactions between acoustic energy, particles, and fluid, as well as the limit on particle sizes that can be manipulated in a given pressure range. Acoustic

patterning uses ultrasonic waves, which have low attenuation in a fluid medium, excluding the need for ultrahigh field strengths. Acoustic field-assisted patterning has been used to develop particle–polymer composites with electrically conductive features and enhanced mechanical strength. While current works have demonstrated the ability to model nanoparticle assembly and construct functional devices, significant effort is needed to establish a standard protocol. This standard protocol could advance the fabrication of multifunctional devices with tunable functional properties and heterogeneous nanomaterial composition.

8. Electrical Patterning

“Electrical patterning” leverages electric fields during printing to control the deposition of ink and to pattern suspended nanomaterials. Electrical patterning can produce nanoscale fibers^[32,100] and droplets,^[314] or engineer the composition of nanomaterials.^[33,34] The first subset of electrical patterning uses an applied voltage to extrude ink and directly form nanomaterial building blocks. The extruded nanomaterials are then patterned to form a 3D construct. Known as electrohydrodynamic (EHD) printing, this subset of electrical patterning can be split into two categories based on the morphology of the extruded ink: electrospinning and electrohydrodynamic inkjet (e-jet) printing. In both methods, a voltage across an air gap between a nozzle electrode and a collector electrode is applied. Backpressure in the nozzle causes a droplet to form at the nozzle tip, held in place by surface tension. The voltage potential generates static charges within the droplet, which migrate toward the collector, causing the droplet to elongate and form a Taylor cone. When the voltage reaches a critical value, electrostatic repulsion overcomes surface tension, and a charged fluid jet is ejected from the tip of the Taylor cone.^[182] In electrospinning, the viscosity of the fluid is sufficient to form a continuous filament whose morphology is dependent on the air gap, voltage, and flow rate.^[100,181] In contrast, the low viscosity ink used in e-jet printing allows surface tension to overcome viscous flow, resulting in the ejection of a rapid succession of droplets; droplet frequency and volume are closely related to the applied voltage.^[183] The second subset of electrical patterning uses electric fields to impart anisotropic alignment in the nanomaterial reinforcement within the composite ink. In this method, the major axis of anisotropic nanoparticles will align parallel with the electric field to minimize the free energy of the system, producing structures with uniform parallel alignment of spun nanofibers or platelets.

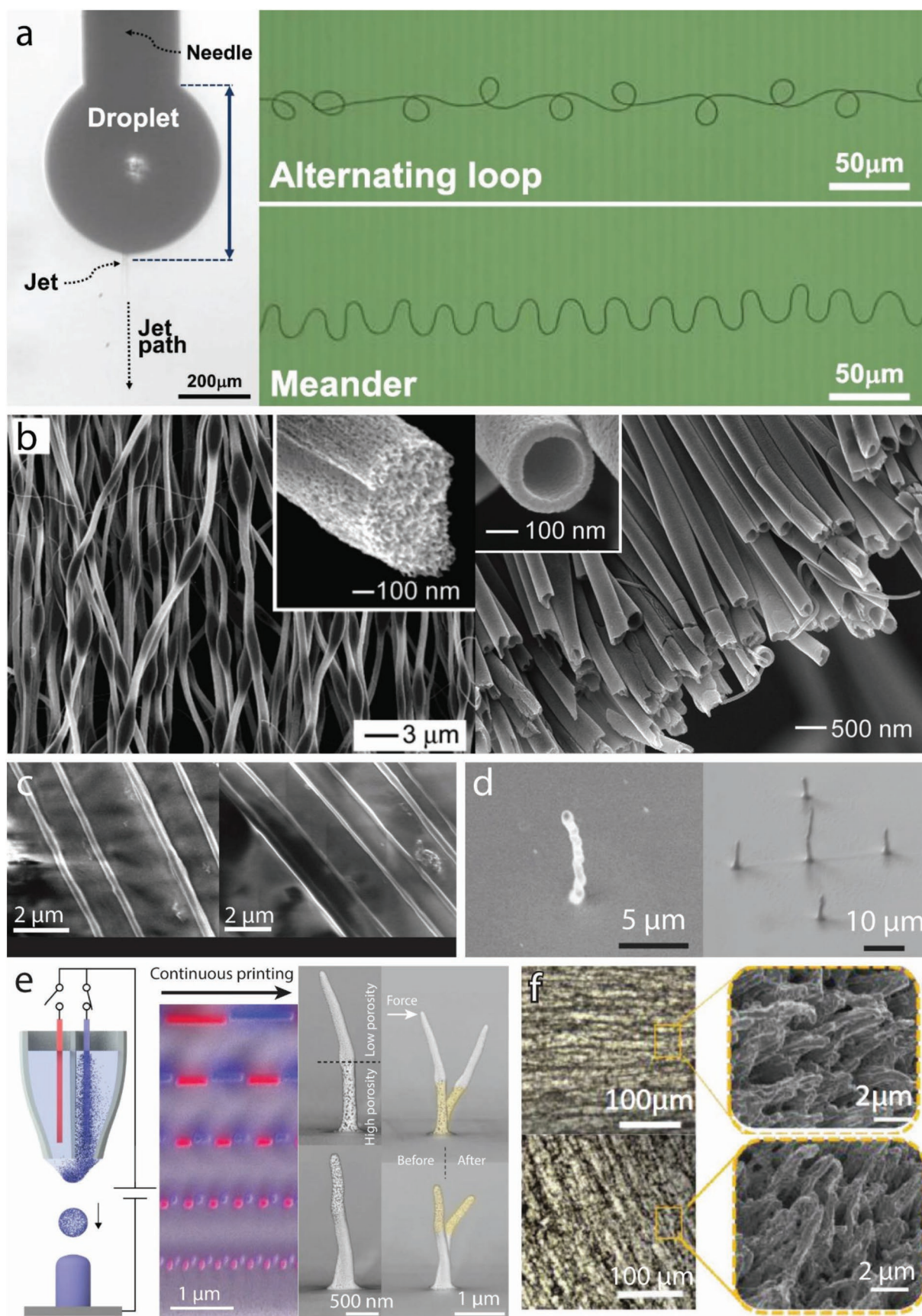
While most nanomaterial patterning techniques modulate the deposition and/or orientation of pre-synthesized nanomaterials in a carrier fluid, electrospinning can directly produce continuous nanofibers.^[32,55,100] To produce a continuous stream of filament, the viscosity of the fluid must be tuned to provide a balance between surface tension and viscous flow. If the spun fluid is a polymer solution, the jet is further stabilized as the viscosity increases due to strain hardening or evaporation.^[182] As the jet exits the Taylor cone, bending instability causes the fluid stream to form loops. In those initial loops, a net outward electric force pulls the stream into larger loops as it descends

toward the collector.^[101] The overall shape of the fluid stream path is described by the “envelope cone”—a volume that encloses the path of the fluid stream, which widens near the collector. Different modes of jetting, such as cone jet, tilted jet, and multijet, are achieved through variations in the electrostatic force and fluid flow rate.^[181,315]

In the repertoire of electrical patterning, cone-jet mode is a standard form of electrospinning capable of generating continuous nanofibers.^[100,316] Cone-jet mode utilizes a steady Taylor cone produced by a balance between normal electric stress and surface tension.^[100,317] High voltages are needed to generate the electric forces necessary to overcome the surface tension. This high voltage places a lower limit on the air gap to prevent arcing.^[100] Reducing the air gap, and thus shortening the jet travel distance, can eliminate the bending instability in the fluid stream and reduce the coiling diameter. Electrospinning with a sub-millimeter jet travel distance is labeled “near-field electrospinning”; larger distances are labeled “far-field electrospinning.”^[318] To produce electrospun nanofibers with sub-10 μm coiling diameters, Shin et al. developed droplet jet mode near-field electrospinning (DJ-NFES).^[100] DJ-NFES uses low voltages (300–1000 V) to achieve sub-500 μm jet travel distance. This voltage is not strong enough to overcome surface tension, so the jet is initiated by a mechanical drawing method that disrupts the surface tension of the droplet. Once initiated, a microscale Taylor cone forms at the air-liquid interface and ejects a fluid stream that forms a filament 94 nm in diameter (Figure 6a, left). The jet travel distance can be changed by moving the nozzle tip or changing the droplet size by increasing backpressure. By controlling the nozzle travel speed and jet travel distance, Shin et al. modified the coiling formation in the printed filament. They printed helical coils, alternating loops, and meandering lines—some achieving sub-10 μm coiling diameter (Figure 6a, right). Similarly, Min et al. developed a near-field electrospinning setup for controlled large-scale assembly of highly aligned, organic semiconducting nanowires (OSNWs).^[319] These nanowires were individually extruded from the Taylor cone, allowing for precise control over the diameter and orientation of the printed wires. In this system, the nozzle tip (inner diameter $\approx 100\ \mu\text{m}$) was positioned less than 1 cm above the collector. This reduction in tip-to-collector distance decreased the perturbation of the jetted solution, facilitating precise control over nanowire orientation. By decreasing the polymer concentration ($<3\ \text{wt}\%$), the diameter of the nanowires was reduced to $<100\ \text{nm}$. Parallel arrays of OSNWs were utilized to fabricate an array of field-effect transistors (FETs) with channel widths of $\approx 300\ \text{nm}$. The FETs achieved a maximum field-effect mobility of up to $9.7\ \text{cm}^2\ \text{V}^{-1}\ \text{s}^{-1}$ with a low contact resistance ($<5.53\ \Omega\ \text{cm}$). Liu et al. also leveraged a near-field electrospinning technique (nozzle-collector gap $\approx 300\ \mu\text{m}$) to fabricate parallel arrayed ZnO granular nanowires (GNWs).^[320] After deposition, thermal calcination produced polycrystalline ZnO GNWs with diameters of $\approx 100\ \text{nm}$. The authors used these GNWs to fabricate photodetectors on a flexible substrate and demonstrated that the GNW photodetectors possessed ultrahigh detectivity (3.3×10^{17} Jones) and a gain (2.6×10^7) that is comparable to single-crystalline ZnO NW photodetectors (gain of 2×10^8) grown by chemical vapor deposition.^[321]

Electrical nanomaterial patterning can also be achieved with far-field electrospinning. Far-field electrospinning has been used to tune the morphology of spun nanofibers and produce parallel arrays of nanofibers. Li and Xia leveraged far-field electrospinning to fabricate hollow nanofibers (Figure 6b).^[32] Dispensing two immiscible liquids through a coaxial spinneret under a strong electric field,^[322] they fabricated two types of hollow nanofibers: titania/polymer and anatase. To fabricate titania nanofibers, Li and Xia ejected an ethanol solution containing both poly(vinyl pyrrolidone) (PVP) and titanium tetraisopropoxide ($\text{Ti}(\text{OiPr})_4$), surrounded by an ethanol sheath layer. By varying the PVP/ $\text{Ti}(\text{OiPr})_4$ ratio, electric field strength, and feeding rate, they produced nanofibers with diameters ranging from 20 to 200 nm. The ability to engineer nanofibers with hollow or multimaterial core-shell morphology could be used to 3D print nanoscale fluid conduits and fiber optics, with applications in fluidic devices and optical waveguides. Typically, far-field electrospinning produces disorderly fibrous mats. With a super-millimeter air gap, a specialized collector is needed to pattern the deposition of spun fibers. Theron et al. constructed a highly parallel array of functional nanofibers by leveraging the sharpened edge of a spinning wheel as a collector (Figure 6c).^[55] The 1D profile of the collector caused the envelope cone to take on a diamond shape, narrowing as the fluid stream approached the collector. Additionally, the charged nanofibers repel one another, producing a 1–2 μm periodic spacing. This modified far-field electrospinning technique enabled Theron et al. to achieve highly oriented fibers over 20 cm distances. In another approach, a horizontal magnetic field was used to align ultralong silver nanowires (AgNWs) within PVP.^[323] Zhang et al. positioned two permanent magnets on either side of the fluid stream path, spaced 5 cm apart. As the extruded fibers approached the magnets, they aligned parallel with the magnetic field and bridged between the magnet faces, forming a dense, nonwoven mat of composite nanofibers. Additional fiber mats were stacked to form grids with a tunable cross-angle. The AgNWs exhibit surface plasmon resonance, with an emission intensity that is strongest when the nanowires are parallel with the polarization angle of the incident light. Due to the highly parallel formation of the AgNW mat, the structure featured an anisotropic transmission spectrum ranging from ultraviolet to visible—whose magnitude could be tuned by varying the cross-angle between the stacked AgNW mats.

Electrical patterning can also be used to pattern nanomaterials with sub-micrometer droplets. Electrohydrodynamic inkjet (e-jet) printing leverages electric fields to eject micrometer and sub-micrometer sized droplets from micro/nanocapillary nozzles for 3D printing.^[183,314] In e-jet printing, the surface tension of the fluid overcomes viscous flow.^[182] This results in the rapid ejection of individual droplets, with increasing frequency at higher voltages.^[183] Metallic nanomaterials can be formed into solid metal structures with rapid evaporation of solvent and postprocess annealing or ion reduction.^[33] The small size of the droplets produced in e-jet printing exhibits large surface-to-volume ratios. The minimal solvent volume within the colloidal droplets evaporates quickly while falling toward the substrate, significantly increasing the viscosity of the droplet, which reduces the spread of the droplet



on the substrate, enabling droplets to be stacked in towers with sub-micrometer diameters.^[314]

E-jet printing can be used with a broad range of metallic, semiconducting, and dielectric materials (10^{-13} to 10^{-3} S m⁻¹).^[324] An et al. printed arbitrary patterns of solid pillars composed of anthracene, Ag, Cu, and Co nanoparticles (Figure 6d).^[314] The application of an electric field during the jetting induces an autofocusing effect on the charged droplets, resulting in the precise printing of complex 3D structures, including arrays of pillars, walls, helices, and freestanding bridges. Utilizing separate nozzles, different formulations of colloidal droplets can be printed side-by-side or stacked, forming hybrid metal-polymer architectures. Using an entire array of semiconducting, dielectric, insulating, and conductive materials, Molina-Lopez et al. e-jet printed arrays of stretchable field-effect transistors (FETs) to create flexible, stretchable electronics.^[325] The transistors could be stretched up to 20% before diminishing in electrical performance, upon which contact separation and electrode cracking occurred. The transistors achieved electron mobility of 27 cm² V⁻¹ s⁻¹, an on-off current ratio of four orders of magnitude, and a transconductance of 47 μ S. The voltage memory of the dielectric allowed the transistors to mimic the short-term synaptic plasticity in neurons. Rapid voltage pulses (–80 mV, 25 Hz) caused migrating ions to accumulate at the dielectric interface and raise the channel current tenfold (50–500 nA). The higher concentration of ions remained at the interfaces for a longer period of time, producing a current “memory” that sustained a channel current for \approx 2 s after voltage application. This ionic nature, coupled with their flexibility and customizable fabrication suggests the usage of these transistors a potential neuron interface for wearable electronics,^[326] machine–brain interfaces,^[327] or neuron simulation devices.^[328,329]

Electrical patterning can also fabricate material hybrid structures by varying the composition of the ink within a single deposition nozzle in situ. Reiser et al. developed “electrohydrodynamic redox printing” (EHD-RP) by inducing a redox reaction on multiple sacrificial electrodes to print a multimaterial metal structure.^[33] The electrical potential was routed through several metal electrodes inside the print head (Figure 6e,

left). Switches controlled the flow of electric charge, changing which metal was printed. Absorption of positive charge in the electrode produces positive metal ions in solution. This e-jet method achieved features down to 250 nm, while rapid switching between electrodes achieved chemical separation down to 400 nm (Figure 6e, center). The collector acts as a substrate and reduces the positive ions in the printed droplet to zero charge metal nanoparticles. As the solvent evaporates, an argon atmosphere prevents oxidation. In their work, copper was printed into a nanocrystalline structure with greater than 90% density and 12% conductivity relative to bulk copper. The lowered conductance is attributed to a high number of point defects and small grain size (<100 nm), though the electric field can be adjusted to tune morphological characteristics, including grain size and density. 3D microstructures were printed using bimetal printing and selective wet etching, including silver conductive bridges with sacrificial copper supports. By exploiting the dissimilar valence shells of copper and gold, copper was selectively etched to tune the mechanical properties of bimetal copper–gold pillars (Figure 6e, right). The removal of copper from the copper–gold section produced a porous region that exhibited lower yield strength. After applying a horizontal force, the copper region showed no signs of permanent deformation, while the porous gold regions plastically deformed. Using this method, it is possible to produce metallic nanocrystalline structures with tuned chemical and physical properties. This method could incorporate three or more channels to expand the range of materials that can be printed at once. Furthermore, multiple voltages could be leveraged to finely tune the concentration of metal ions in each droplet, producing mixtures with higher fidelity than what can be achieved with a binary control.

Electric fields can be used to pattern nanomaterials beyond EHD printing. By applying a horizontal electric field across the resin reservoir of a bulk 3D printing method, anisotropic conductive nanomaterials can be aligned to produce biomimetic composites with programmed reinforcement orientation. Similar to electrospinning and e-jet printing, the presence of a direct current (DC) electric field induces surface charges in the conductive nanoparticles, causing the charged anisotropic

Figure 6. Patterning of nanoparticles with electric fields. a) Near field electrospinning reduces bending instability, producing a precisely controlled nanofiber pattern with droplet-jet mode. The left image depicts droplet jet. The right image shows a nanofiber meander and alternating loop, controlled by adjusting print speed. Reproduced with permission.^[100] Copyright 2019, IOP Publishing, Ltd. b) Hollow nanofibers can be fabricated using a spinneret with concentric nozzles. The left image shows a scanning electron microscope (SEM) image of titanium dioxide fibers electrospun with a dimethylformamide/tetrahydrofuran (DMF/THF) solution of polystyrene as the core material and ethanol as the sheath material. Inset is a cross-sectional SEM image of the fiber fractured from the bright region showing the highly porous nature of the fibers. The right image shows an SEM image of a uniaxially aligned array of anatase hollow fibers, and the inset shows the cross-section SEM image of a single fiber. Reproduced with permission.^[32] Copyright 2004, American Chemical Society. c) The sharpened edge of a rotating wheel can be used to collect electrospun nanofibers in a highly parallel fashion. Left and right images show SEM images of polyethylene oxide nanofibers, diameters 100–300 and 200–400 nm. Reproduced with permission.^[55] Copyright 2001, IOP Publishing, Ltd. d) SEM image of e-jet printed pillars using copper nanoparticle suspensions and anthracene (left). The electric field induces an “autofocusing” effect, allowing precise deposition of microscale constructs, such as a cross-shaped array of five anthracene pillars (right). Reproduced with permission.^[314] Copyright 2015, Wiley-VCH Verlag GmbH & Co. KGaA. e) Electrohydrodynamic redox printing (EHD-RP): metal ions are dissolved from electrodes in the printhead and deposited in droplets to be reduced into pure metal nanocrystals and porous structures (left). Multiple metals are printed simultaneously or in rapid succession, forming structures with chemical separation smaller than 400 nm (center). Copper (gray) and copper–gold alloy (yellow) structures, with selective dealloying and removal of copper producing porous regions of gold (yellow) with lower yield strength (right). An applied force results in elastic deformation of the solid copper region and plastic deformation of the porous gold region. Reproduced under the terms of a Creative Commons Attribution 4.0 International License.^[33] Copyright 2019, The Authors, published by Springer Nature. f) Horizontal electric fields can be rotated to direct the alignment of nanoparticles. Example optical and SEM images of the fracture surface of multiwalled carbon nanotube composites, aligned 0° to the horizontal (top) and 45° to the horizontal (bottom). Reproduced with permission.^[34] Copyright 2017, Wiley-VCH Verlag GmbH & Co. KGaA.

nanoparticles to become polarized along their principal axis. Three pivotal forces—torque, Coulombic, and electrophoresis forces—orient the nanoparticles.^[330] Upon application of a directional electric field, the misalignment between the anisotropic nanoparticles and the field direction induces a torque that rotates the nanoparticles, causing parallel alignment between field and nanoparticle. In addition, Coulombic forces can cause the electrically polarized nanoparticles to migrate toward one another to form a network. However, electrophoresis was not observed in the highlighted works, likely due to the low permeability of the surrounding polymer resin.^[34,54,331] The result is a highly aligned composite that can be layered to form biomimetic materials. For example, Yang et al. patterned multi-wall carbon nanotubes (MWCNTs) in an SLA printing process by generating an electric field with two parallel electrodes mounted on a rotating base.^[34] A DC voltage was applied to the two electrodes to create an electric field, and the direction of alignment of the MWCNTs was controlled by rotating the base (Figure 6f). By varying the alignment of the MWCNTs, rotating by 45° while printing consecutive layers about the normal axis, they achieved bioinspired Bouligand MWCNT laminates. These Bouligand structures force crack propagation paths to follow the helical structure, dissipating more energy and significantly increasing toughness.^[4] Tensile tests revealed that the alignment of MWCNTs increased the anisotropic elastic modulus in comparison to a randomly distributed structure.^[34] Furthermore, the use of DLP to selectively cure regions of the print enabled Yang et al. to construct an artificial structure that mimics human meniscus with both radial and concentric reinforcement.

Moreover, the magnitude of the electric field, as well as the direction, has a significant effect on the functional properties of the structure. Similar to the method utilized by Yang et al., Chavez et al. aligned dispersed MWCNTs by applying an electric field during SLA printing to fabricate MWCNT-photopolymer nanocomposites.^[331] Samples with MWCNTs aligned parallel as well as perpendicular to the test direction improved mechanical and electrical properties with respect to samples with randomly aligned MWCNTs. The alignment of MWCNTs increased the conductivity of the composite by 26%. Similarly, the alignment of MWCNTs improved the tensile strength by about 40% compared to samples with random orientation. However, simply incorporating nanomaterials without patterning was detrimental—randomly aligned composites exhibited stress concentrations due to agglomeration of MWCNTs, leading to premature failure. Similarly, careful control over the patterning voltage is critical, as high voltages (1000 V cm⁻¹) can lead to agglomeration and premature failure. The high voltages produced electrical percolation sites, regions of electrical energy concentrations, and increased Coulombic attraction, forming MWCNT agglomerates.

Through the careful control of the direction and magnitude of the electric field, electrical and mechanical properties can be tuned. Building on their previous method, Yang et al. printed a nacre-like structure of aligned graphene nanoplatelets (GNs), which not only enhanced the toughness and strength of the matrix polymer but also introduced the ability to sense damage due to a change in resistance.^[54] Natural nacre, with its hierarchical “brick and mortar” structure of aragonite lamina and protein matrix, is a critical component in seashells due

to its ability to resist crack propagation.^[104] The 2D geometry of GN produces anisotropy in the dipole moments; the dipole moment parallel to the plate is stronger than the perpendicular dipole moment, producing a torque that rotates the GN in line with the electric field. The parallel lamellar arrangement of the GNs was leveraged to produce a biomimetic composite with similar crack-arresting behavior to natural nacre, as well as to impart anisotropy in electrical conductivity. π - π bonding between aligned GNs enables fast electron transport parallel to the reinforcement direction, resulting in a 100-fold increase in electrical conductivity in the parallel direction relative to the perpendicular direction. Crack formation further increases the electrical resistance, which can provide a method for real-time damage monitoring in military and sports protective gear. As seen in these highlighted works, electrical patterning can be used to program anisotropy in electrical and mechanical properties and to produce biomimetic composites.

In summary, electrical patterning leverages electric fields to program the morphology of extruded ink and pattern nanomaterials reinforcement. Electrical patterning is used to directly produce patterned nanomaterials, including nanoscale fibers^[32,100] and droplets^[314] or to program the alignment of nanomaterial reinforcement.^[33,34,54,331] Electrical patterning is used to produce functional structures with anisotropic electrical, optical, and mechanical properties due to tailored anisotropy, as well as fine microstructures of highly aligned nanofiber grids. Exploiting the charged state of the fluid jet while controlling fluid flow rate and print speed, EHD printing can produce patterned nanofibers and nanodroplets directly from a liquid medium, resulting in high-resolution, multimaterial 3D constructs. Furthermore, parallel electrode plates are used to produce horizontal electric fields across bulk printing methods to orient nanomaterials during the printing process. Electrical patterning produces structures with highly uniform, parallel alignment of spun nanofibers or nanotube and nanoplatelet composites. For further reading, the readers are referred to these reviews on nanoscale construct fabrication using electrical forces.^[101,332–336]

9. Magnetic Patterning

“Magnetic patterning” describes the alignment and distribution of magnetically active nanoparticles within a 3D printing process by leveraging external, directional magnetic fields. This patterning method can impart magnetic functional properties to printed structures or tune mechanical properties via control over the orientation and location of reinforcing nanomaterials. Magnetically active nanomaterials consist of ferromagnetic particles or nonmagnetic particles with a magnetically active coating. Within a single material class, the magnetic properties of nanomaterials are size-dependent. At the smaller size range (<15 nm), cubic magnetite (Fe₃O₄) particles are superparamagnetic,^[337] larger particles (15–76 nm) have a single magnetization direction, and the largest particles (>76 nm) have multiple regions with independent magnetization directions. Large external magnetic fields (18–180 Oe, magnetite)^[337] are required to induce a permanent magnetic polarization in multidomain particles.

The relationship between particle size and magnetic properties is explained in domain theory.^[338] A magnetic domain is a discrete region of material in which the direction of magnetization is uniform. Consider a single, large (>100 nm) crystal of magnetite with a single magnetic domain. This crystal will have high magnetostatic energy due to its magnetic polarization. To reduce the total energy in the system, the single domain splits into two domains with opposite directions of magnetization. However, a greater number of domains results in decreased domain wall width, which increases the total energy. At equilibrium, the number of domains is dependent on composition and temperature. As the size of a particle decreases, the domain walls become too thin, and the particle becomes a single-domain particle. The coercivity of a single-domain particle is size-tunable. Coercivity peaks at the boundary between multidomain and single-domain then decrease along with particle diameter.^[338]

Thermal energy also plays a role in the observed magnetism of a particle. For any ferromagnetic material, there exists a Curie temperature, above which thermal fluctuations cause it to transition from ferromagnetic to paramagnetic (580 °C for magnetite).^[339] For single-domain particles and grains, this transition occurs below the Curie point.^[340,341] Above this “blocking temperature,” the domains have enough energy to randomly reorient their magnetism; when measured, the particle appears to have a net-zero magnetization. This blocking temperature decreases with particle size, so that very small (<15 nm) magnetite particles are superparamagnetic above −133 °C.^[342]

The particle sizes of magnetic nanomaterials can be tuned for the desired magnetic characteristics. Superparamagnetic particles exhibit stable magnetic moments only in the presence of a magnetic field—an ideal choice for nanomaterial patterning when no magnetic remanence is desired.^[337,338] Nonmagnetic alumina platelets can be coated with superparamagnetic iron oxide particles to induce magnetic functionality.^[29,31,77] Anisotropic nanoparticles, nanorods, and platelets align parallel with the magnetic field to reduce the total energy of the system. Permanently magnetized multidomain ferromagnetic particles and single-domain particles align with respect to their domain polarization, programming the magnetic remanence of the construct.^[337] This attribute allows for shape-changing, magnetically actuated structures.^[343]

The modulation of the magnitude and direction of the external magnetic field enables a high level of control over nanomaterial patterning.^[77,344] Electromagnetic solenoids and permanent magnets are used to control the magnitude and direction of the magnetic field. When the magnetic field is generated by electromagnetic solenoids, multiple orthogonal solenoids generate a 3D magnetic field, where the strength of each solenoid controls the resulting magnetic vector.^[29,77,344] When the magnetic field is generated by a permanent magnet, the magnet is physically rotated and translated in space to adjust the field.^[31,49,77,205]

Magnetic patterning can be used to mimic highly complex, hierarchical multiscale architectures exhibited in nature^[2] such as sheet nacre,^[3,103] stomatopod dactyl club,^[4] and cortical bone^[5,345] that have excellent resistance to abrasive wear, crack propagation, and out-of-plane stress.^[105] This can be achieved by varying the orientation of nanoparticle reinforcement to

produce superior mechanical properties than that of conventional monolithic composites.

For example, composite architectures inspired by osteonal bone (**Figure 7a**, left) exhibit isotropic tensile strength due to the concentric reinforcement of ceramic platelets.^[29] Cracks face high resistance at the interfaces of composite reinforcement structures;^[307–310] regions with perpendicular reinforcement to the crack front provide greater resistance. The concentric reinforcement of the osteon-inspired composite resists crack propagation in all directions. The concentric composite exhibits a threefold increase in tensile strength relative to a monolithic composite with transverse reinforcement. To fabricate this composite, three orthogonal solenoids produced a 3D magnetic field to align anisotropic ceramic platelets (thickness 350 nm, diameter 7.5 μm) that were coated with superparamagnetic nanoparticles (10 nm). For each layer, regions of nanoparticles were aligned, then selectively cured by DLP. This process was repeated until all unique orientations were achieved. To further demonstrate this method's crack steering properties, Martin et al. programmed a nonuniform reinforcement pattern consisting of a square plate with 0° or 90° reinforcement, and “islands” of perpendicular reinforcement (90° or 0°). In specimens with island reinforcement oriented perpendicular to the primary crack direction, the crack propagated around the islands (**Figure 7a**, center and right). In specimens with island reinforcement oriented parallel to the primary crack direction, the crack propagated through several islands. This technique could be used to direct cracks around critical parts in a structure, protecting sensitive components such as sensors and fuel storage.

A dynamic magnetic field can be used to improve the axial alignment of magnetically tuned platelets to further improve the mechanical properties. The alignment of reinforcing platelets is dependent on the magnitude of the magnetic field, the magnetic response of the material, the particle loading, and the fluid viscosity.^[344] For example, the size of the particles can affect the balance of energy in the system when patterning with low magnetic fields. For a platelet with a diameter of less than a few micrometers, thermal energy dominates the free energy of the system and causes the platelets to randomize their alignment. At a diameter greater than a few micrometers, gravity dominates and causes the platelets to lie flat. At a diameter of about 5 micrometers, the platelets exhibit an ultrahigh magnetic response (UHMR), which allows magnetic patterning with low magnetic fields. Most reinforcing particles are diamagnetic particles that require very high magnetic fields (≈1 T) for alignment.^[115] As such, modulating the size of the alumina platelets and coating their surfaces with superparamagnetic magnetite particles can enable the patterning to be achieved with a low magnetic field of ≈10 mT.^[77]

The concentration and location of the magnetite nanoparticles also affect the magnetic response. Reducing the concentration from 0.5 wt% Fe₃O₄ to 0.01 wt% increases the required field strength from 10 to 30 mT. Additionally, platelets with iron oxide nanoparticles concentrated on their surface can be patterned with a field that is 40% weaker than if the nanoparticles are evenly distributed throughout their volume. To illustrate this, Erb et al. produced an ink composed of polyurethane and alumina platelets with 13% and 1% iron oxide surface coverage

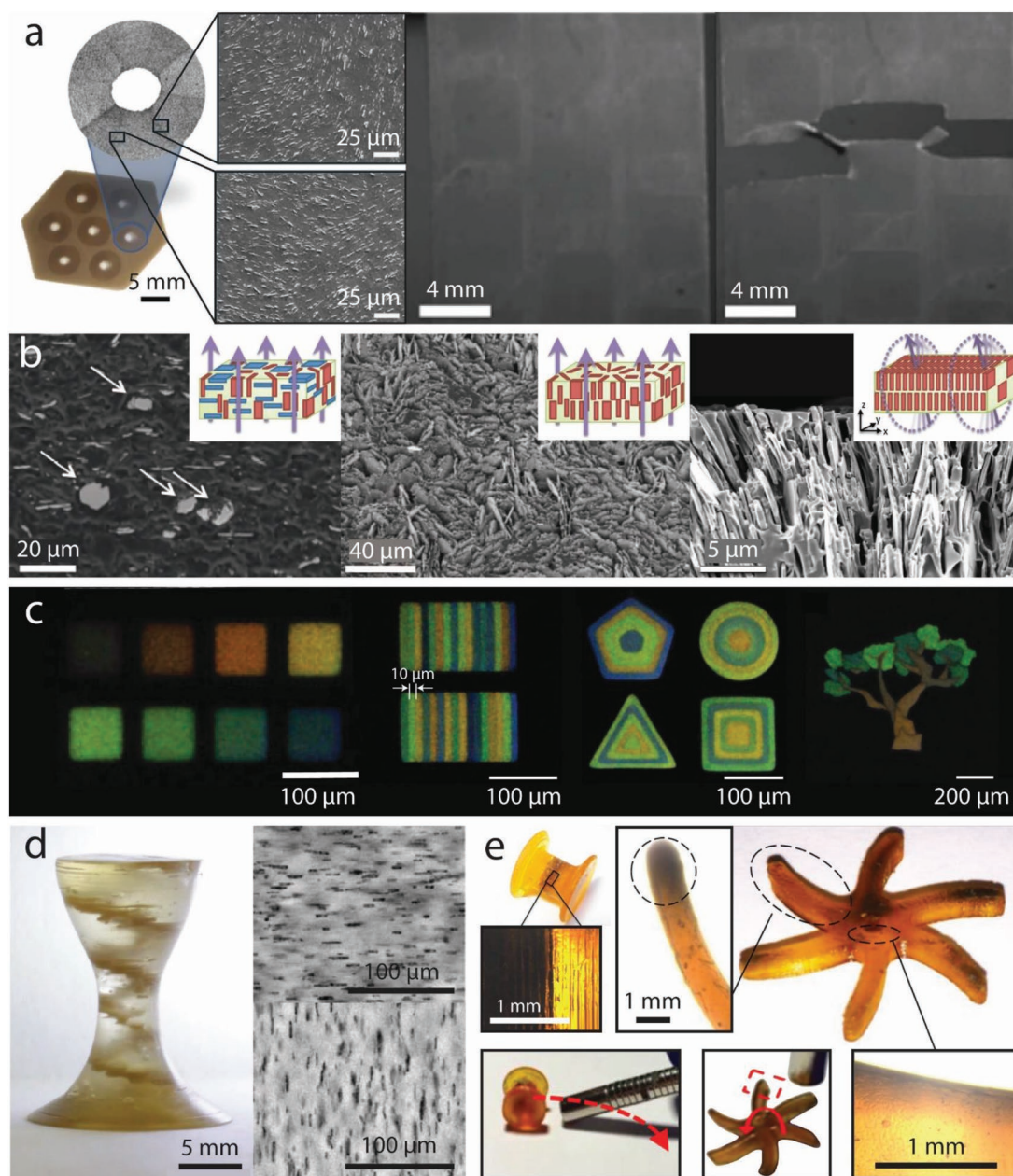


Figure 7. Patterning of nanoparticles with magnetic fields. a) Magnetic patterning of bioinspired composites. Schematic and 3D printed result of the concentrically reinforced osteons of cortical bone (left). 3D printed plate subjected to vertical tension, programmed to steer cracks around the darker colored islands (center, right). Lighter colored sections contain platelets oriented parallel to crack propagation, and darker sections contain platelets oriented perpendicular to crack propagation. Reproduced under the terms of a Creative Commons Attribution 4.0 International License.^[29] Copyright 2015, Macmillan Publishers Limited. b) Scanning electron microscope (SEM) images of magnetically aligned platelets with a schematic inset of the magnetic field direction (blue arrows) and aligned platelets (red or blue plates). A sample with highly magnetized (red) and weakly magnetized (blue) platelets (left). Magnetized platelets subjected to an out-of-plane magnetic field (center). Further alignment and packing of platelets are achieved by rapidly rotating the magnetic field (right). Reproduced with permission.^[77] Copyright 2012, The American Association for the Advancement of Science. c) Printed structures composed of planar-normal chains of superparamagnetic magnetite colloidal crystals with tuned interparticle distances to produce structural colors. The left image depicts reflection micrographs demonstrating the change in structural color, red to blue, with an increasing magnetic field. The other three images depict reflection micrographs of printed structures with various structural colors. Reproduced with permission.^[42] Copyright 2009, Springer Nature. d) A multimaterial print containing viscoelastic “shaping” ink (transparent) to constrain low-viscosity ink containing the composite reinforcement. Micrographs highlight the uniform alignment of reinforcing particles. Reproduced under the terms of a Creative Commons Attribution 4.0 International License.^[31] Copyright 2015, Macmillan Publishers Limited. e) Local magnetic gradients can be coupled with multimaterial DIW to produce regional variation in nanomaterial concentration. This is leveraged to produce active constructs, to be remotely actuated by local magnetic fields. A band of magnetically active nanoparticles provides a mechanism to accelerate, decelerate, and steer a wheel (top left and bottom left). A “smart” impeller (top right) composed of magnetically active blade tips (top center) and pure resin body (bottom right) is driven clockwise or anticlockwise by a reversible magnetic field (bottom center). Reproduced with permission.^[49] Copyright 2017, American Society of Mechanical Engineers.

(1 and 0.1 wt% Fe_3O_4 respectively) and subjected it to magnetic fields of different magnitudes (Figure 7b, left).^[77] The diagrams in Figure 7b are colorized to show the strongly magnetized platelets in red (1 wt% Fe_3O_4) and the weakly magnetized platelets (0.1 wt% Fe_3O_4) in blue. After exposure to an 80 mT horizontal field for 5 min, all platelets were aligned horizontally. Then, the sample was subject to a 10 mT vertical field for 10 min, to which only the strongly magnetized platelets aligned. However, a static magnetic field can only pin a single axis, resulting in misalignment in the second axis (Figure 7b, center). Steric hindrance limits the concentration of aligned platelets to about 20 vol%. This can be increased to 50 vol% with the use of dynamic magnetic fields.^[344] A magnetic field rotating at a high frequency pins the two principal axes of the platelets to the plane of the rotating field. This causes biaxial alignment, which can be used to align composites with high concentrations (Figure 7b, right). The field is rotated at high frequency to overcome the synchronous rotation of the platelets as gravity, fluid viscosity, and the magnetic field induce torques on the platelet.

Inspired by the high loading content of nacre microstructures in abalone shells, Martin et al. and Erb et al. used this biaxial alignment to create highly concentrated composites with tunable mechanical properties.^[29,77] Composites with 0° alignment (parallel with loading) exhibited 63% and 86% higher yield strength compared to pure polymer and composites with 90° alignment. The reinforcement alignment can also be used to tune wear resistance and hardness: vertical platelets are firmly anchored within the polymer matrix by shear stresses along their principal axes, improving wear resistance—while horizontal reinforcement increases platelet removal rate due to the increased surface area that is exposed to abrasive materials. Likewise, wear testing indicates a 45% reduction in wear volume for 0° alignment and a 32% increase in wear volume for 90° alignment, with respect to samples composed of pure resin. Vickers hardness testing indicates a 41% increase in hardness for 0° alignment and a 25% increase in hardness for 90° alignment. Composites that feature additional reinforcement alignments can be tuned to exhibit multiple anisotropic mechanical properties. For example, Erb et al. produced a composite with both high Vickers hardness and high flexural modulus by printing a top layer of vertically aligned platelets and a bottom layer of horizontally aligned platelets.^[77]

Magnetic patterning can also be used to impart structural color, which are unique nanostructures found in nature.^[6–9,17,346,347] In nature, the wavelengths of reflected light, metallic effects, and iridescent effects are tuned by manipulating the microstructure of biological materials. For example, peacock feathers contain only melanin rods, yet the spacing of the internal lattice structures produces thin-film interference and reflects vibrant colors.^[348] Structural color has several advantages over chemical pigmentation. First, structural color has high resistance to photobleaching, while the color saturation of pigments degrades over time. Second, structural color can be produced using a single material—simplifying manufacture and allowing for fine-tuning of the resulting color.

Using a magnetic field, superparamagnetic colloidal nanocrystal clusters can be patterned to produce a photonic crystal by modulating the distance between particles. When subjected to an external magnetic field, the magnetic moments

of the magnetite clusters increase, which in turn increases the magnetic dipole interaction energy.^[349] The clusters align in vertical chains with the magnetic streamlines, and the interparticle separation in the chains is tuned by balancing the attractive magnetic force with repulsive electrostatic and solvation forces. From Bragg diffraction theory, the interparticle distance determines the photonic crystal's structural color (Figure 7c). Kim et al. developed a three-phase ink ("M-Ink") consisting of superparamagnetic colloidal nanocrystal clusters capped with silica shells, solvation liquid, and photocurable resin to produce structural color.^[42] Using an SLA printer and a uniform magnetic field, this ink is printed in vertical layers to produce a tunable lamellar structure. Increasing the magnetic field reduces the interparticle spacing, which reduces the wavelength of reflected light. The sequence of small squares in Figure 7c (read from left to right, top to bottom) show the shift in color from red to blue that accompanies an increase in magnetic field strength. The color output of the photonic crystals is also sensitive to mechanical deformation. Bending a flexible film of M-Ink changes the angle of the internal lamellae with respect to the incident light, which allows the characterization of the curvature by measuring the shift in color. Furthermore, despite a limited palette of colors, Kim et al. produced high-quality images through spatial modulation of reflection intensity and color. Specifically, 16.7 μm pixels were grouped into 4×4 matrices, where each matrix supported 4-bit intensity modulation by varying the number of pixels that reflect light. The matrices were programmed to mix colors and produce gradients in a process similar to halftone color.^[350] This method can create high resolution (≈ 1500 dpi) images with high color tunability via the separation and angle of lamellae in the final structure.

The integration of magnetic nanomaterials with 3D printing can also impart magnetic properties and actuation abilities. These actuation abilities allow the structure to be rotated, translated, and deformed by an external magnetic field or a change in environmental conditions. An active structure can be produced by patterning the distribution of magnetic nanomaterials within the structure to program deformation behavior and tailor magnetic remanence. For example, the orientation of ferromagnetic fibers changes the residual magnetic flux density.^[205] Using an SLA printer with five orthogonal electromagnets, Nakamoto and Marukado printed samples with varying ferromagnetic fiber (40 nm \times 320 nm) orientations. The fibers were then magnetized by a 100 mT field for 1 min. An out-of-plane alignment doubled the magnetic flux density on the surface of a sample with respect to an in-plane alignment.

A nonuniform magnetic field of a permanent magnet can be used to form concentrated regions of magnetic nanomaterials. Erb et al. used a permanent magnet to create a spatial gradient of magnetic strength and direction.^[77] The magnetic particles were drawn to the origin of the magnetic field, concentrating the reinforcing nanomaterials in a specific area. This technique can stabilize geometric discontinuities that form stress concentrations. In one sample, functional alumina platelets surrounded a hole, providing concentric reinforcement for the weakened area. In another sample, an array of fixed, "rotating" magnets similar to a Halbach array^[351] was used to align the platelets in a "rolling" gradient. This gradual change in orientation from

vertical to horizontal produces parallel regions in the material that exhibit different stress–strain behavior. Upon absorption of water, the composite swells in a wavy pattern.

Local magnetic gradients can also be coupled with multimaterial DIW to produce regional variation in the programmed orientation and concentration of reinforcing nanomaterials. Kokkinis et al. used DIW to create a multimaterial print that was reinforced with alumina platelets and coated with ferromagnetic particles to create the UHMR effect.^[31] To reduce the manufacturing time for the multimaterial printing, the viscosity of the magnetic nanoparticle–polymer composite ink is kept below a few Pascal-seconds^[77] and a polymer ink with a higher concentration of fumed silica was printed alongside the magnetic ink to provide a supportive shell. As a proof of concept, a helical structure is demonstrated in Figure 7d, where each level of the darker colored helix features a different platelet orientation. This variation in the local orientation of reinforcing platelets was used to produce active structures with programmable deformation. For example, when the composite absorbs a solvent, it exhibits 30% greater swelling strain in the direction perpendicular to the reinforcement by the principles of hygromorphism.^[116] Similarly, composites exhibiting dissimilar swelling were printed next to each other as bilayers, resulting in either convex or concave curvature. These bilayers were used to build 4D structures such as an interlocking cuboid structure that slides together when dry and locks together when swollen. This enables the fabrication of dynamic systems without hinges or bearings.

In addition to absorption-driven, “4D” structures, programmable magnetism can be used for remote actuation with external magnetic fields. For example, using an SLA printer with five orthogonal electromagnets and a ferromagnetic short fiber composite ink, Nakamoto and Marukado produced a horizontal cantilever beam with vertical fiber alignment.^[205] Introducing a permanent magnet below the beam produced a vertical deflection that increased with higher loading percentages. As a result, tailoring the local concentration of magnetic nanomaterials enables the production of smart structures (Figure 7e).^[49] These smart structures produce complex motion in response to a magnetic field.

In another example, using a combination of SLA and DIW, Lu et al. produced a magnetically actuated impeller, wheel, and flexible film.^[49] The devices were composed of photopolymer with discrete regions of iron particle reinforcement. To incorporate discrete patterns of magnetic nanomaterials within the resin, a magneto-rheological fluid was injected through a DIW nozzle, then kept in place and magnetized by a permanent magnet while the resin was cured by SLA. This technique can provide heterogeneity in single-material printing methods,^[125] such as an impeller with magnetic material at the tips of the blades (Figure 7e, right). This allows the magnetic propulsion of the structure by changing the magnetic fields due to the attraction or repulsion of the blade tips. In another example, a rolling motion can be triggered with an external magnetic field applied on a “smart” axel where there is an offset region of magnetic material rigidly connected to two wheels (Figure 7e, left). The offset magnetic material produces a dissimilar normal force on the wheels, causing the structure to turn while rolling. Similarly, a magnetic field applied nonuniform force to

regions of iron reinforcement, causing local bending in a flexible film. The deflection of the film was controlled by printing a discrete pattern of magnetic material. These “smart” structures could form the basic components of more complicated, remotely actuated robots with a tailored magnetic response and freeform, 3D printed architecture.

In summary, magnetic patterning utilizes an external magnetic field to program the distribution and alignment of magnetically active nanoparticles. Anisotropic particles will align their principal axes with an applied magnetic field, providing a method for programming multiscale, heterogeneous composites. High frequency, rotating magnetic fields will program biaxial alignment in 2D nanomaterials by pinning both principal axes in the plane of rotation, enabling the production of composites with higher particle loading. In addition, the distance between magnetic particles can be tuned by balancing magnetic dipole attraction with electrostatic and steric repulsion, which can be used to engineer structural color. Further localization of magnetic nanomaterials can produce smart structures with actuation properties and heterogeneous composition. Indeed, having the ability to fine-tune mechanical properties, optical anisotropy, and magnetic domain orientations, magnetic patterning is a powerful method to create magnetically controllable structures^[312,313] as well as to enable further customization for 3D printed devices.

10. Optical Patterning

“Optical patterning” leverages photonic energy to catalyze reactions on the surface of nanoparticles or to polymerize resins with nanoscale resolution. For example, photonic energy can be used to move nanoparticles by optical trapping. When the localized surface plasmon resonance (LSPR) of the particle is similar to the wavelength of the projected laser, enhanced interaction between the particle and the light gives rise to plasmon-enhanced optical forces, which confines the particle to the center of the laser spot.^[352] Since the introduction of laser writing in recent decades, optical printing has spawned a variety of scientific applications^[352] and has been used to fabricate metal nanolattices,^[353] photonic crystals,^[354] microlens systems,^[43] biomimetic structures,^[355] and triboelectric nanogenerators (TENG).^[47]

The ability to manipulate nanoparticles with nanoscale precision via optical tweezers through optical trapping could enable the fabrication of nanoscale devices. In 1970, Ashkin discovered that radiation pressure from a continuous wave (CW) laser could be used to manipulate micrometer-sized particles and predicted that this could be extended to move atoms and molecules on the nanoscale.^[356] When a milliwatt laser strikes at an offset of a few micrometers from the center of a micrometer- or sub-micrometer particle, the optical radiation pressure accelerates the particle forward and toward the axis of the beam. The main challenge in accurately moving the trapped particles is separating the radiation pressure from thermal forces, which are several orders of magnitude greater. To avoid these radiometric effects, which are generated from laser-induced temperature gradients in the medium, Ashkin used relatively transparent particles and fluid to reduce the absorption of

thermal energy. Having isolated the radiation pressure, particles can be migrated from one location to another and trapped on a surface.

The use of optical tweezers in optical patterning is demonstrated in its extensive use in gold nanoparticle manipulation. Urban et al. focused a laser beam on a suspension of gold nanoparticles (AuNPs) (80 nm) that were stabilized by a coating of cetyltrimethylammonium bromide (CTAB) molecules; optical forces were thereby applied to the AuNPs which overcame the electrostatic repulsion and bound them to the substrate using van der Waals interactions.^[357] The particle could be positioned with a precision of 50 nm. However, the increase in laser power will decrease precision due to the faster diffusion of nanoparticles. The authors proposed that this method of optically manipulating at the molecular level is applicable to a wide range of AuNPs and can be used to fabricate nanoscale electronics one nanoparticle at a time.

Optical patterning can also be used to create photonic crystals (PC) with optical properties that can be tuned by modulating the physical crystal structure in the 3D printed constructs. PC are highly ordered structures of materials that can confine and control the propagation of light due to the existence of photonic bandgaps.^[358,359] This property makes PCs excellent candidates for a wide range of applications, from gas sensing to the creation of optical fibers, photonic papers and flat displays.^[151,360] Optical-based 3D printing can produce spatially variant photonic crystals, in which the size of the unit cells is varied to control the propagation of light.^[361] For example, two-photon polymerization (2PP) can be used to fabricate high-quality 3D PCs. These PCs can incorporate different resin materials and be tuned to operate in a wide range of emission spectra with excellent optical properties.^[362–364] Deubel et al. fabricated large-scale face-centered cubic structures with bandgaps ranging from 1.3 to 1.7 μm ,^[354] Kaneko et al. fabricated diamond-lattice photonic crystal structures which they described as a covalent-bond type crystal with pronounced band-gap effect^[365] and Guo et al. used a homemade femtosecond laser microfabrication system to fabricate 3D log-pile photonic crystals in S-3 resin, with an absorption peak of around 380 nm.^[366]

Optical patterning can also be used to fabricate piezoelectrical nanoparticle–polymer composites with enhanced piezoelectric behavior. However, the interaction between nanoparticles and the polymer matrix must be optimized in order to enhance the stress transfer efficiency. Kim et al. used images projected from a DLP printing process to sequentially polymerize layers of photolabile polymer solution.^[367] This method incorporates chemically modified barium titanate (BTO) nanoparticles to fabricate 3D structures. **Figure 8a** shows a rolled-up honeycomb pattern of the nanoparticle composite after polymerizing a solution of BTO nanoparticles embedded in a poly(ethylene glycol) diacrylate (PEGDA) matrix. The crosslinking of the polymer with the chemical groups on the piezoelectric nanoparticles enhanced the piezoelectric output of the composite films by channeling mechanical stress to the piezoelectric crystals. The authors have also recently shown that fine-tuning the size of the nanoparticles and linker molecules can increase stress transfer between the composite matrix and the surface of the nanoparticles.^[368] For example, when a polymer with higher molecular weight is used, the increased

molecular interactions between the nanoparticles and polymer increases stress transfer through the material by increasing the number of functionalized deformation modes. More recently, Cui et al. demonstrated that anisotropy in the electromechanical coupling properties of a piezoelectric metamaterial could be achieved through variations in unit cell morphology.^[369] 3D structural node units (unit cells) are designed with different strut configurations, then tessellated to create a mesoscale material. For example, by changing the strut angle from 75° to 90° in the unit cell of a surface-functionalized lead zirconate titanate (PZT) metamaterial, the manipulation of the electric displacement map was shown to achieve directional sensing. In addition, a lattice could be constructed with regional differences in the cell structure. Coupled with voltage sensing for each region, this device could map the magnitude and location of applied strain throughout the lattice.

High-resolution optical patterning via two-photon polymerization (2PP) is a powerful method for producing hierarchical microarchitectures with nanoscale features. Hensleigh et al. used projection micro-stereolithography (PμSL) to create 3D structures of graphene foams by synthesizing photocurable graphene oxide (GO).^[370] The fabricated structures had a hierarchical assembly of microarchitected graphene with structural features from a few micrometers to hundreds of micrometers. In contrast, 2PP 3D printing can create significantly higher resolution (≈ 100 nm) with tightly focused, femtosecond-pulsed near-infrared laser radiation.^[371] The energy of the photons is insufficient to cause polymerization individually, so complete excitation only occurs in a narrow focal point, where two photons excite the resin in quick succession. This produces microscale structures with nanoscale voxels with a length scale as small as 100 nm.^[372,373]

2PP has been shown to be a propitious method for the fabrication of functional devices such as optical meta-materials, microlens systems, photonic devices, nanoparticle-composite matrices, as well as hierarchical structures with nanoscale features. Furthermore, this ability of 2PP to precisely pattern a photopolymer in spatially pre-defined regions could be leveraged to fabricate micro imaging, micro focusing, and beam shaping systems.^[374] For example, the fabrication of ultracompact multilens objectives can be realized by utilizing 2PP to produce parts with increased optical performance. Gissibl et al. demonstrated that through layer-by-layer writing using a highly transparent, ultraviolet sensitive photoresist (IP-S), high performance, complex multilens optical systems can be fabricated.^[43] **Figure 8b** contains scanning electron microscopy (SEM) images of the singlet, doublet, and triplet lens objectives, which show the ability of 2PP to fabricate complex compound objectives with 100 nm layer resolution. They reported that these miniaturized lens systems could potentially be used in the creation of miniaturized microscopes and endoscopic applications.

Optical patterning can also be used to 3D print metallic and ceramic microlattices with a linear stiffness-to-density ratio using the polymer resin as a sacrificial template. For example, fugitive ceramic nanoparticles can be incorporated into the polymer itself, which is later sintered to create a purely metallic structure.^[353] In another approach, pure polymer structure can first be printed, then plated with nickel or alumina 100 nm to 2 μm thick.^[35] The polymer is thermally decomposed to leave a structure composed of pure metallic hollow struts.

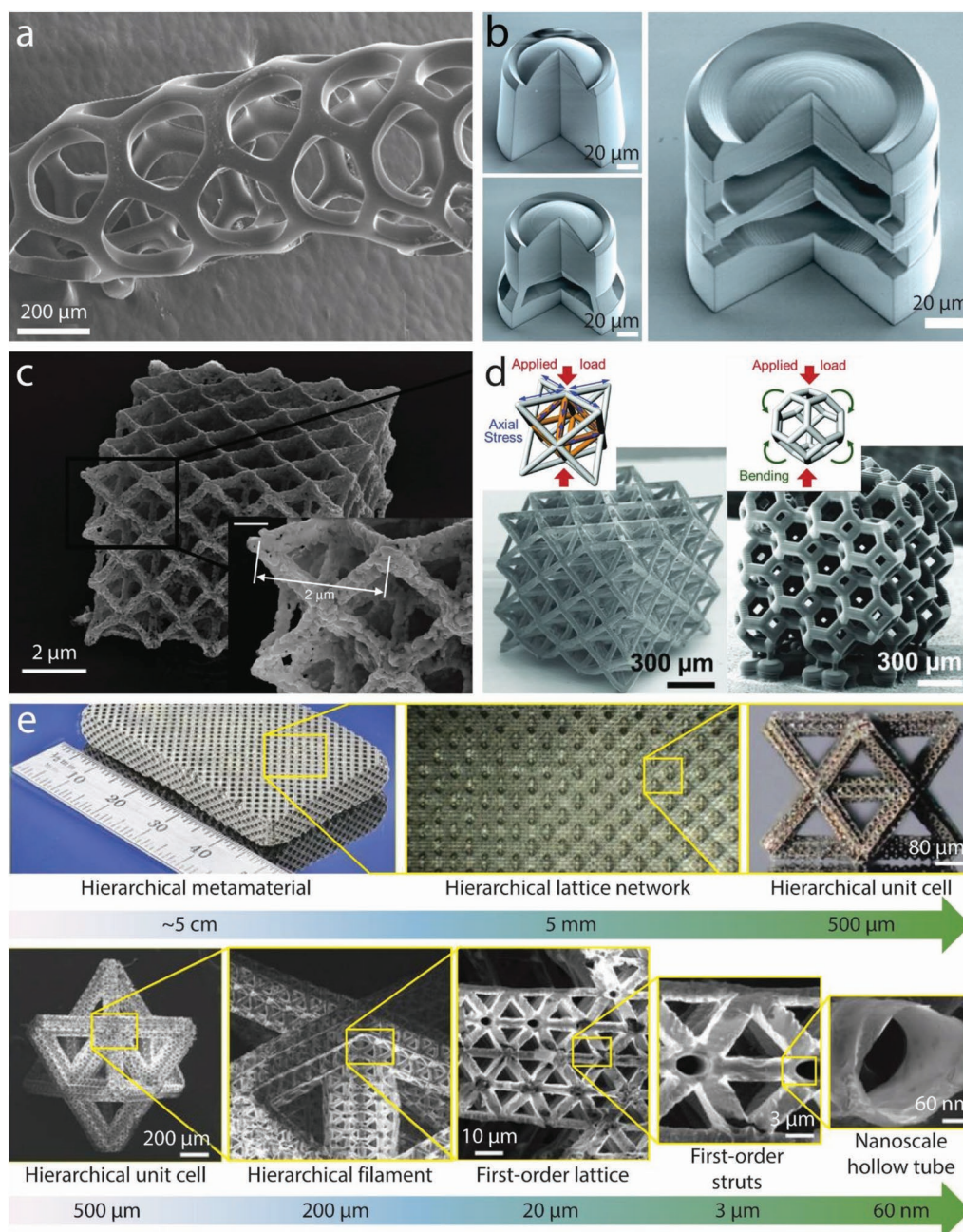


Figure 8. Optical patterning of nanoparticles and nanoscale features. a) Digital projection lithography (DLP) can be used to produce freeform piezo-electronics. Scanning electron microscopy (SEM) image of a barium titanate (BTO)–polymer composite honeycomb array, spontaneously curled into a microtubule structure. Reproduced with permission.^[367] Copyright 2014, American Chemical Society. b) Optical patterning allows for the fabrication of miniaturized imaging devices. Two-photon direct laser writing produces singlet, doublet, and triplet objective lenses with 1, 2, and 3 refractive surfaces, shown in SEM images, anti-clockwise from top. Reproduced with permission.^[43] Copyright 2016, Springer Nature Limited. c) Optical patterning allows for the fabrication of nanolattices by incorporating metal nanoparticles in a photocurable resin. SEM reveals the pure nickel construction of a nanolattice that was fabricated using two-photon polymerization, then thermally treated to remove the organic photopolymer. Reproduced under the terms of a Creative Commons Attribution 4.0 International License.^[353] Copyright 2018, The Authors, published by Springer Nature Publishing AG. d) Optical patterning allows for the fabrication of microscale structural components that convert compression into tension. Cubic microlattices of octet-truss (left schematic) and tetrakaidecahedron (right schematic) unit cells are periodically repeated to form a lattice, then sintered to produce stiff, ultralow density structures of pure metals or ceramics (left and right SEM images, respectively). Geometry impacts stiffness: the octet-truss transduces compression into strut tension, producing a superior stiffness-density relationship over the tetrakaidecahedron, which transduces compression into strut bending. Reproduced with permission.^[35] Copyright 2014, The American Association for the Advancement of Science. e) Optical patterning can fabricate critical feature sizes that expand into multiple length scales. A scanning-DLP process enables the fabrication of a multiscale hierarchical metamaterial, composed of a fractal microlattice geometry with critical feature sizes spanning from 5 cm to 50 nm (SEM images, left to right). Leftmost and rightmost scale bar values (200 μm , 60 nm) were approximated from the text. Reproduced with permission.^[36] Copyright 2016, Springer Nature.

High-resolution optical patterning can be used to produce lattice structures with nanoscale struts and unit cells, enabling the realization of architectures such as optical metamaterials^[375–378] or structures with enhanced mechanical properties.^[379,380] Vyatskikh et al. used 2PP to create 3D metal geometries with a resolution of 25–100 nm.^[353] A metal-rich photoresist containing nickel acrylate as the metal precursor was patterned with 2PP, followed by postprocessing with pyrolysis at 1000 °C in an inert atmosphere and reduction at 600 °C to volatilize the organic constituents. They reported that the printed structures were ≈80% smaller in linear dimensions compared to the original 3D digital design and were composed entirely of metal. It is shown that using a layer thickness as low as 120 nm, metal nanolattices with 10 μm octet unit cells can be synthesized (Figure 8c). The inset of Figure 8c shows a magnified view of the porous metal nanolattice. It was found that the pyrolysis process is accompanied by an approximate five times linear shrinkage in feature size: the 2 μm diameter of the beams in the printed polymer-metal structure shrank to produce 300–400 nm beams in the nickel nanolattice.

This optical patterning approach for producing metallic lattices with high-resolution unit cells can be leveraged to fabricate mechanical metamaterials, where the mechanical properties of the structure depend on their geometrical configuration rather than their composition. For example, tuning the morphology of the unit cell can create ultralow-density lattices with a nearly constant stiffness-density relationship over three orders of magnitude in density. Zheng et al. used projection micro-stereolithography (PμSL) to fabricate metallic unit cells that could be infinitely joined to make multiscale microlattice structures (Figure 8d).^[35] As the density of a cellular solid decreases, its stiffness decreases. Typically, in cellular solids with random porosity, this relationship is quadratic because the struts and cell walls undergo bending when subjected to stress. The unit cell geometry was based on the octet-truss of Deshpande et al.^[381] and the tetrakaidekahedron (or Kelvin foam cell) used by Jang^[382] and Takahashi et al.^[383] The geometry of each unit cell causes the macroscale tension and compression loading to translate into pure tension and compression within the micro to nanoscale struts. This significantly increases the stiffness and load capacity of ultralow density structures.

Zheng et al. also used a custom stereolithography printer to manufacture fractal lattice structures with geometry spanning seven orders of magnitude, from nanometers to centimeters (Figure 8e).^[36] These sponge-like macro structures were more flexible than the solid form of their metallic constituents, even exhibiting a compressive elastic compression 50% greater than all other metal foams and lattices. This 3D printing method was able to produce parts with dimensions rivaling that of 2PP, but with much greater scalability using DLP and scanning optics to create a high-resolution projection of a single unit cell and scan it across the build surface, thus creating macroscale objects out of nanoscale components. In contrast to the octet-truss unit cells, the geometry of this metal lattice was designed to be dominated by truss bending, which reduces stiffness and results in a more elastic structure. In addition to creating a metal foam with enhanced elasticity and near-constant specific strength, this metamaterial fabrication strategy could be a harbinger for advanced biomimicry. Many

biological materials—from bone to gecko setae—exhibit hierarchical structures that span several orders of magnitude.^[384] This nanomaterial patterning technique could enable the production of gecko-inspired adhesives^[355] and durable, porous building materials.^[385,386] For a further detailed analysis of the properties and capabilities of nanolattices, the reader is referred to Bauer's progress report.^[379]

“Dip-in” direct laser writing is another method for improving the scalability of multiscale optical patterning while retaining the ability to produce high-resolution features. A variant of 2PP, standard direct laser writing (DLW) focuses a beam of light through a transparent substrate and into the photolabile resin, with an immersion oil between the lens and substrate to match refractive indexes. However, the height of the printed part is limited by dissimilarities in the refractive index between substrate and resin, as well as the working distance between the lens and substrate. To overcome these issues and create a DLW system with more scalability, Bückmann et al. developed “dip-in” direct laser writing, forgoing immersion oil and dipping the microscope lens directly into the photolabile resin.^[373] This eliminates any refractive boundaries between materials and enables the fabrication of structures several millimeters in height with sub-micrometer features. These larger fabricated structures allowed for direct compression and strain characterization of a metamaterial with tailorable Poisson's ratio. The sub-micrometers features allowed for the production of small unit cells, which are favorable in harmonic loading.^[387] They envision that such metamaterials could be used for tissue regeneration by tuning a printed scaffold to match the anisotropic Poisson's ratios found naturally occurring within bone tissue, forming a mechanically seamless graft.

2PP has also been demonstrated to be a powerful tool for the fabrication of biomimetic materials and structures, which often exhibit hierarchical assembly from the nanoscale to the mesoscale.^[388] For example, Marino et al. fabricated trabecula-like structures, which mimic the microenvironment of trabecular bone cells with a biocompatible hybrid photoresist—Ormocomp (registered product of micro resist technology).^[389] This biomimetic structure was used to regulate the behavior of human osteosarcoma cells (Saos-2), reducing cell proliferation and increasing osteogenic differentiation. 2PP also provides faster design iteration in addition to superior biomimicry, enabling innovation of high-performance adhesives. Röhrig et al. reported the fabrication of gecko-inspired structures from acrylic-based negative tone resist (IP-G 780) using DIW, with widths from 500 nm to 5 μm, and surface roughness of 35 nm.^[355] 3D printing allowed the usage of stiff resin to enable the matching of Young's modulus and the relevant length scales of the structures with the properties exhibited by the gecko setae.^[390,391] This was an improvement over conventional molding techniques, which can be limited to softer polymers^[392,393] and involve lengthy fabrication times.

In summary, optical patterning leverages photonic power to induce photopolymerization of resin and fabricate nanoscale and hierarchical structures. This is accomplished by employing different strategies such as optical trapping, two-photon polymerization, and microstereolithography. The integration of nanomaterials expands the range of optical patterning, allowing light-based 3D printing to fabricate structures with features from the microscale to the nanoscale, using a broad variety

of materials.^[352] Given the highly controlled nature of photon emission, the ability of optical trapping to build nanostructures at single-particle resolution, and advances in multiscale production, optical patterning is a propitious nanofabrication tool to overcome the limitations of conventional techniques. The high surface quality of optically printed structures enables the fabrication of micro-optics with minimal optical aberrations. Printed metamaterials consisting of unit cells with 100 nm resolution can exhibit tailored mechanical properties. While some promising steps have been taken to scale nanoscale prints to the millimeter and centimeter scale, improvements in overall print size,^[373] material selection, and throughput are necessary to expand its applications.^[394]

11. Thermal Patterning

“Thermal patterning” leverages thermal energy to modulate material system phase changes and crystal effects to guide the distribution of nanomaterials. For example, the phase changes in a material system can be manipulated to tune the resulting microstructure in situ with 3D printing.^[37,38,106,230] Additionally, the thermal effects of crystal structures can be used to manipulate the deposition of nanomaterials.^[102] Pyroelectricity can be used for an electrode-free method of electrohydrodynamic printing, allowing an electric charge to control fluid droplets. Finally, thermal patterning can be readily integrated with other nanomaterial patterning processes as a complementary control mechanism to enhance control over the formation of complex microstructures.

Thermal energy can be used to modulate phase transitions to govern nanomaterial patterning behavior and the formation of microstructures. For example, increasing the ambient temperature increases the rate of solvent evaporation of an inkjet-printed colloidal ink, which increases the viscosity of the droplet and decreases the droplet diameter. Using a heated substrate, Kullmann et al. were able to control the aspect ratio (mean wire diameter to wire height) of inkjet-printed, vertical gold microwires assisted with in situ laser annealing (Figure 9a).^[230] The ink consisted of colloidal gold nanoparticles (2–4 nm) and toluene, a volatile solvent. As the temperature increased from 20 to 80 °C, the diameter of the printed wires decreased by 60%. As the height of the wire increased, the influence of the heated bed decreased, resulting in a larger diameter at the top of the wire.

The inclusion of in situ simultaneous (ISS) laser annealing can further reduce the diameter from 197 to 144 μm. ISS laser annealing also reduces the difference between the diameters of the top and bottom of the wire during droplet deposition from 23.6% to 8.6%. Further, reducing the printing voltage can also increase the feature aspect ratio. The left image in Figure 9a shows a wire with an aspect ratio over 50, having been printed at 90 °C and ±6 V. The ISS laser annealing also increases the probability of forming pocketed wires. The right image in Figure 9a shows the top of a pocketed wire when printed at 70 °C, ±20 V, and ISS laser annealing. The pocket is ≈200 μm in diameter, with a crack that reveals gold nanofilaments, indicating that the ISS laser alters the microstructure of the wire. Furthermore, Kullmann et al. show that the modulation of temperature can create a wide range of microstructures: below

25 °C for pocketed wires, 25–50 °C for walls, and 70–90 °C for solid wires and bridges.^[102] Overall, this study suggests that the adjustment of temperature, voltage, and in situ laser annealing during inkjet printing can improve the control over the microstructure, surface quality, and geometry of freeform structures formed from metal nanoparticle colloids.

The controlled cooling of a material system can also be used to program anisotropic properties in a printed structure. During the solidification process, a cold sink removes heat from the material system. When the temperature of the material drops below its melting point, it begins to crystallize, forming a solid structure. The formation of crystals can be controlled to manipulate the resulting microstructure. For example, freeze casting is a physical process wherein an aqueous slurry of micro or nanoscale particulates and a freezing agent such as water can be used to fabricate porous structures.^[395–397] As the water crystallizes, the nanoparticles are pushed by the solidification front, forming regions of concentrated solute. Depending on the method of freezing, the ice crystals can form an isotropic or anisotropic microstructure.^[398] If the aqueous solution is placed in an insulated container and cooled from all directions equally, the ice crystals form randomly throughout the solution. As the ice crystals grow, they form an isotropic porous structure. If the aqueous solution is placed on a cooled substrate (–25 °C) and insulated in all other directions, the ice crystals grow upward and form vertical columns. Eventually, the entire structure solidifies. The ice crystals are then sublimated from the fully solidified structure to leave a “green scaffold,” which is then sintered to form a final scaffold of pure nanomaterial composition.^[399] The resulting porous microstructure is composed of dense walls of fused particles and voids where the ice crystals once grew. Indeed, the ability of freeze casting to produce highly porous and stiff structures is useful to create complex, hybrid biomaterials that mimic the structural and mechanical performance of natural structures, which have significant applications in tissue engineering.^[397]

The integration of freeze casting and extrusion-based 3D printing can produce multiscale scaffolds with programmed porosity in the micro- and macroscale. Zhang et al. developed a freeze casting DIW printer that used an aqueous graphene oxide (GO) suspension to produce highly porous graphene aerogels (GA).^[37,38] In this process, GO ink is extruded onto a cooled build plate and subsequently freezes. As the next layer of nonfrozen ink is printed on top of the previous layer, it partially re-melts the previously frozen layer, forming strong hydrogen bonds between layers as they refreeze. As the ice crystals grow, the GO sheets align along the solidification front and are compressed between crystals, aligning along the crystal boundaries.^[400] The reduced GO sheets bind together due to π – π attraction and form a crosslinked microstructure that eliminates layer boundaries (Figure 9b). The printed part is freeze-dried then thermally annealed to create an ultralight (0.5 to 10 mg cm^{–3}) lattice cube of porous graphene aerogel. The GA is resilient to compressive loading cycles and exhibits piezo-resistivity and good conductivity (≈15.4 S m^{–1}). Enabled by three-dimensional transport of thermally activated electrons across conjugation domains within the highly cross-linked network of GO sheets, the GA also exhibits semiconductor behavior with a negative temperature

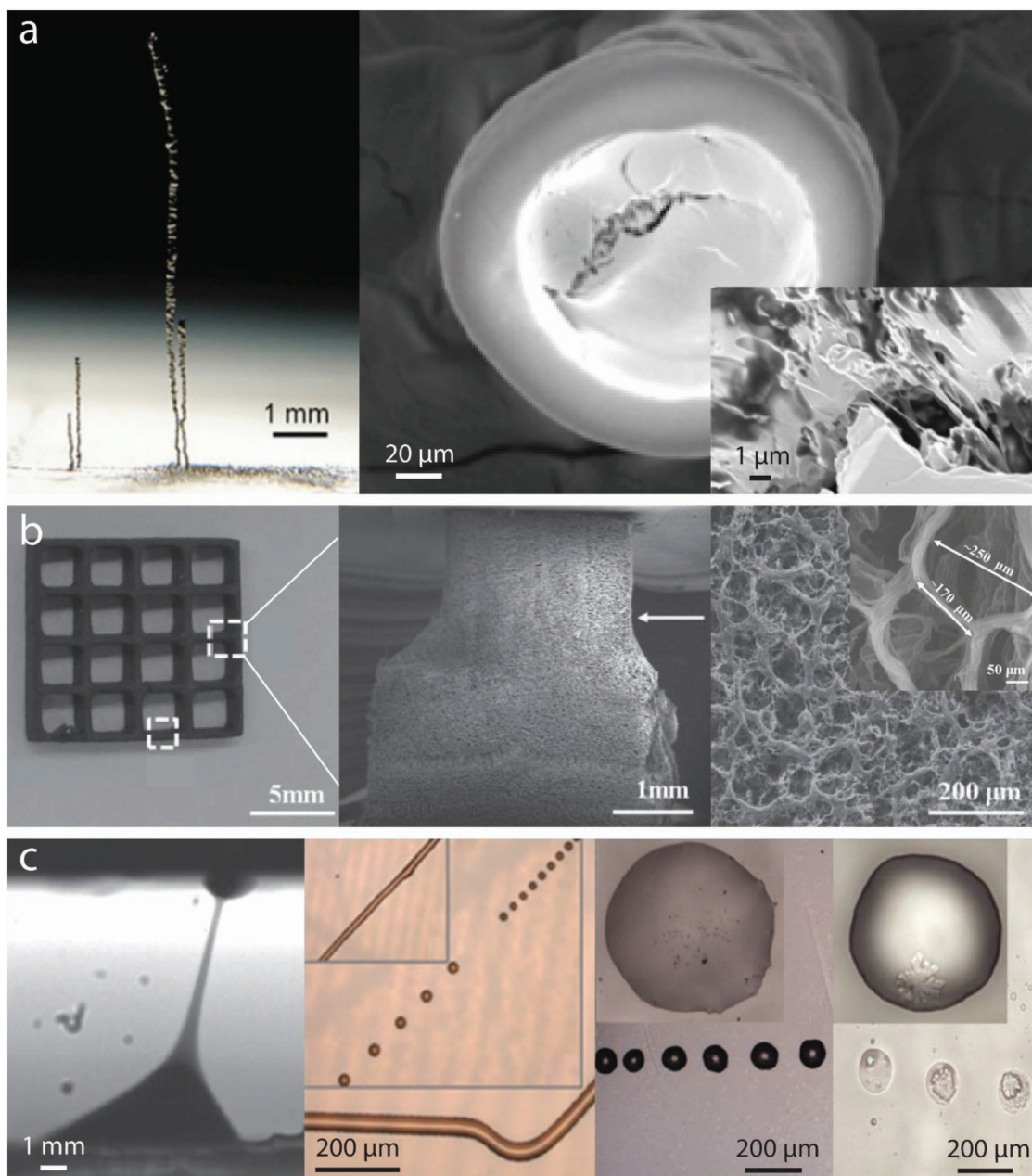


Figure 9. Thermal patterning of nanoparticles. a) Thermally controlled evaporation can modulate the viscosity of jetted droplet colloids. The heating of the substrate can assist the printing of vertical wires with aspect ratios greater than 50:1 (left). In situ laser annealing provides further control over structure morphology (right). A scanning electron microscope (SEM) image of the top view of a wire printed with in situ laser annealing reveals nanowire microstructure. Reproduced with permission.^[230] Copyright 2012, IOP Publishing Ltd. b) Freeze casting during inkjet printing can produce fine porous microstructures. An aqueous graphene oxide (GO) ink was printed onto a cold sink to form a 3D graphene aerogel (left). Droplets remelt the previous layer before freezing, creating a seamless transition between layers and producing a lattice with high structural integrity (center). The fractal growth of ice crystals produces a microscale porous structure of crosslinked GO sheets (right). Reproduced with permission.^[37] Copyright 2016, Wiley-VCH Verlag GmbH & Co. KGaA. c) A thermal stimulus can activate a pyroelectric crystal, producing an electric field to pattern sessile droplets. Moving the point-wise heat source causes an almond oil drop to shoot at an angle (right). Continuous lines and separate droplets can be printed by moving the collection plate (center left). This patterning technique can print a variety of materials, including a suspension of carbon nanotubes in mineral oil (center right), and a mixture of cell cultivation medium and oleic acid (right). Reproduced with permission.^[102] Copyright 2010, Nature Publishing Group.

coefficient of expansion (NTCE). The resistance increases by 97% at $-192\text{ }^{\circ}\text{C}$ and decreases to 48% at $350\text{ }^{\circ}\text{C}$, relative to room temperature. The loading-to-weight ratio of the GA is as high as 16100 while also exhibiting nonlinear, superelastic

behavior up to 50% strain. The unique capabilities of freeze casting as a thermal patterning method enable the production of microarchitected GAs with exceptional superelastic, semiconductor properties, which are attractive materials for

strain-sensitive and temperature-sensitive sensors with high resistance to fatigue.

Thermal patterning can also be used to program the microstructure of eutectic systems. A eutectic system is a homogenous mixture of two or more materials with a lower melting temperature than that of its constituents.^[401] As a eutectic alloy is cooled, its components undergo solidification and diffusion, forming a metal alloy.^[402] This process can be integrated with 3D printing to fabricate freeform structures with a programmable eutectic microstructure. The eutectic metal alloys are heated in the DIW nozzle to a molten state, then upon extrusion are cooled, causing their constituents to organize into lamellar or periodic structures.^[403] Boley et al.^[106] used a so-called “high-operating-temperature DIW” (HOT-DIW) to print a molten eutectic ink composed of silver chloride (AgCl) and potassium chloride (KCl) to fabricate mesoscale architectures with aligned lamellar features. The alternating AgCl and KCl lamellae form at the solidification front just behind the HOT nozzle. The spacing between the lamellae is dictated by the rate of solidification of the ink and the diffusion of molecules before solidification. Boley et al. were able to vary the periodic spacing between the lamella in the printed parts between 100 nm and 2 μm by modulating the printing speed. Below a critical speed, the temperature gradient within the filament thickness is constant, producing optimum parallel lamellae. This lamellar architecture forms a Bragg reflector, giving the filament structural color, where the modulation of the lamellar spacing results in the reflection of a different wavelength of visible or infrared light. Further, the diffraction efficiency can be increased from 1.6% to 15% by selectively etching the KCl and coating the resulting AgCl–air structure with silver, potentially increasing its commercial viability. In comparison to Kim et al.’s magnetic patterning of M-Ink,^[42] this is a facile method that can produce customized Bragg reflectors and freeform structures with tailored optical functional properties.^[404,405]

Thermal patterning can also be achieved by leveraging pyroelectric phenomenon. Pyroelectricity refers to the generation of electric charge on the surface of a crystal due to spontaneous polarization in response to a change in temperature.^[406,407] For example, below its Curie temperature (1483 K) lithium niobate (LiNbO_3 , LN) is a ferroelectric, trigonal crystal composed of repeating, planar sheets of $\text{Nb-O}_3\text{-Li}$ in the Z direction.^[408] Heating the crystal causes the lithium and niobium ions to move relative to the oxygen layers, which increases the polarity of the crystal.^[409] This produces an electric field in the Z direction, whose magnitude is dependent on temperature. Z-cut LN crystal wafers can be used in conjunction with a pointwise thermal stimulus for 3D printing.^[409–411]

Known as “pyroelectrohydrodynamic shooting,” the localized pyroelectric effect operates similarly to electrohydrodynamic (EHD) printing. Developed by Ferraro et al., this method uses an LN crystal wafer which is positioned above a glass slide.^[102] The glass slide is used as a reservoir, upon which a drop of almond oil, mineral oil, oleic acid, or polydimethylsiloxane (PDMS) is placed. An infrared laser heats the wafer from above, where a temperature increase of 100 $^\circ\text{C}$ generates a 10 kV localized electric field that attracts the sessile droplet. The surface of the droplet is pulled toward the wafer until it forms a fluid jet and deposits onto the wafer (Figure 9c). This

process is comparable to Shin et al.’s droplet-jet electrospinning,^[100,318] but without high voltage electrodes or specialized dispensing tips. In this process, the fluid is separate from the patterning apparatus, which offers superior protection from contamination. Additionally, the laser can be split to produce multiple heated points, which increases the throughput of this method. The position of the laser spot can be moved to change the shooting angle up to 20°. This allows a single drop reservoir to dispense in a 23 mm^2 area. A thin substrate can be placed in front of the LN wafer and translated in the x-y directions to draw 2D patterns of repeating droplets or continuous, freeform lines (Figure 9c, center). The reduction of the drop reservoir can also decrease the size of the printed droplets where droplets as small as 3.6 aL (300 nm radius) have been demonstrated.

In addition, thermocapillary action can be created from the generation of a thermal gradient by reducing the gap between the heated spot and the glass walls. The droplets are moved by thermocapillary action, making this printing technique a potential candidate for transport and mixing of cellular-scale fluids. In the rightmost image of Figure 9c, Ferraro et al. patterned mineral oil and oleic acid with dispersions of carbon nanotubes and cell cultivation medium, respectively, where salt crystallization can be seen in the cell cultivation mixture. Ferraro et al. envision this method as a high-throughput bioassay tool, where attoliter droplets could house individual cells, and together with the mixing of transport droplets, could facilitate studies of nanomaterial biocompatibility in a single cell.^[412,413] The printer can be designed such that two glass slides are the only contact surfaces. This method can handle multiple parent fluids simultaneously with no risk of contamination from nozzles, and no high voltage electrodes or complex mechanisms are required.

The simplicity of thermal patterning makes it an excellent candidate to augment other patterning processes as a means to provide complementary control mechanisms that can increase the precision and degree of control in nanomaterial patterning. First, thermal motion can be used to tune the alignment of anisotropic nanomaterials when combined with fluid shear patterning. For example, Gantenbein et al. used a combination of fluid shear and thermal patterning to extrude a polymer with heterogeneous reinforcement.^[414] In this process, a liquid crystal polymer (LCP) consisting of the rigid monomers p-hydroxybenzoic acid and 2-hydroxy-6-naphthoic acid is extruded by FDM. The LCP contains domains of randomly oriented rod-like polymer chains which align parallel to the filament axis due to fluid shear when passing through the FDM nozzle. As the filament is deposited on the substrate, it is no longer subjected to fluid shear. As it cools, residual heat drives thermal motion in the polymer, randomly orienting the polymer chains. The core of the filament remains at a higher temperature for a longer period, causing increased randomization. Hence, the difference in the degree of polymer chain alignment between the outer and inner layers of the filament gave the appearance of a core–shell structure where the highly aligned shell layer was stiffer than the core layer. A reduction in filament diameter and print head temperature can increase the cooling rate, which results in higher stiffness. For example, an 80% reduction in nozzle diameter results in a threefold increase in Young’s modulus, while an 88% reduction in layer height results in a sevenfold increase in Young’s modulus. As a

proof of concept, Gantenbein et al. were able to produce a composite polymer structure with tunable stiffness by integrating thermal patterning to modify the degree of fluid shear alignment. Similar to the constructs produced by Gladman et al.^[48] and Reiser et al.,^[33] this patterning method could be used to program heterogeneous and anisotropic deformation in smart structures and reinforcement scaffolding.

Second, the integration of freeze casting and an external magnetic field allows for organized nucleation of ice and control over the distribution of the particles. The distribution is governed by the competition of forces caused by supercooled, dendritic ice growth and the external magnetic field.^[415] Nelson et al. used a Helmholtz coil to subject surface-magnetized magnetite particles to a uniform magnetic field.^[416] The magnetic field influences both the orientation and porosity of the structure by increasing the dipole energy and drawing the particles together, increasing the density of the lamellae. While ice crystal growth concentrated the nanoparticles into a porous scaffold, the uniform field aligned the nanoparticles into vertical columns and prevented agglomeration, which resulted in a 55% increase in ultimate compressive strength and elastic modulus. The magnetic field also influences the microstructure by aligning the parallel lamellar walls in a single direction where the alignment of the lamellae is influenced by the magnitude of the magnetic field, increasing from 38% alignment without a magnetic field to 84% with a 5.2 mT field. The integration of magnetic patterning and freeze casting can be used to produce denser freeze casted structures with a programmed, lamellar microstructure.

In summary, thermal patterning uses thermal energy to control heat-sensitive material processes, including particle interactions, phase changes, and pyroelectric effects. For some applications, thermal patterning is limited by temperature-sensitive samples, such as cell-infused tissue regenerative scaffolds. Nevertheless, the thermal patterning approach can enable effective modulation of nanomaterial patterns and the creation of microstructures. It is also compatible with a broad range of materials and can be readily integrated into a broad range of extrusion or bulk 3D printing technologies.

12. Conclusions and Outlook

We have highlighted the synergistic integration of nanomaterials and 3D printing technologies, wherein the patterning of nanomaterials can be achieved with a wide range of physical phenomena. This multiscale approach represents a powerful strategy that can potentially create highly heterogeneous, multi-material architectures and devices. However, the full potential of this synergistic integration has yet to be achieved. We discuss several fundamental limitations and also propose strategies to advance the multiscale 3D printing approach.

First, the control of nanoscale materials with predominantly micrometer-scale 3D printing processes is challenging. Indeed, improving the spatial resolution of nanomaterial patterning can provide the opportunity to create more complex constructs.^[417] This improvement could allow for the fabrication of hierarchical constructs that mimic the complexity of the biological system. Strategies to improve spatial resolution have been

demonstrated with technologies such as droplet-jet near-field electrospinning,^[100,318] dip-pen lithography,^[373] and 2PP.^[43,123] However, as anticipated from the nature of additive manufacturing, the increase of spatial resolution often has a competing relationship with the scalability of this fabrication approach.

Hence, patterning methodologies that can achieve a more scalable patterning of nanomaterials in micro or mesoscale is highly desirable. For example, evaporative assembly^[40,45,46,78] has been demonstrated to be capable of creating a highly controlled pattern of microstructures at that span from the nanoscale to the centimeter scale.^[254–264] Nevertheless, evaporative colloidal assembly remains a complex and dynamic phenomenon that is extremely sensitive to a wide range of properties. Significant fundamental questions remain unanswered due to the long-standing challenges in elucidating the confounding relationships between governing parameters typically coupled with dynamic, multiphase phenomenon.^[216,281] Future fundamental studies, for instance, with a confined construct,^[228] or floating thin film^[232] can potentially elucidate various mechanisms of such complex assembly.

Second, the compatibility between nanomaterials and the fundamental mechanism of a specific 3D printing technology often limits its potential applications. Despite their attractive properties, the integration of nanomaterials may introduce interfering factors or pose additional requirements or constraints to the corresponding 3D printing process.

For example, in a powder bed fusion process (PBF) such as SLS and SLM, while smaller particles can often result in higher print resolution and surface finish, the reduction of powder sizes can produce challenges in PBF printing.^[152] Specifically, as the size of constituent powder particles decreases ($<1\ \mu\text{m}$), van der Waals forces can cause agglomeration, which leads to uneven spreading of the powder.^[89] The smaller particles also have the tendency to become airborne, compromising the reliability of the optics and moving parts. Furthermore, the increase in surface-area-to-volume ratio corresponds to an increase in reactivity which, for some materials, may result in spontaneous combustion in the presence of oxygen. Indeed, nanomaterials integration may require extensive instrumentation modification, such as an atmospheric control system to provide an inert printer environment.

In another example, the addition of nanomaterials to improve photolabile resins-based 3D printing processes can have potential side effects. Specifically, the addition of nanowires to improve the resilience to deformation^[159] can increase light scattering at higher fill content ($>50\%$ for nanowires). This leads to the degradation of the laser selectivity, a reduction in curing depth and an increase in the curing width. Further, the light scattering is affected by the size and shape of the nanoparticles, the loading of the nanoparticles, and the refractive index of the nanoparticles and resin.^[161] In a similar optical nanopatterning phenomenon, the efficacy of optical trapping is improved by using relatively transparent particles and fluid to reduce radiant heat and thermal gradients.^[356]

Likewise, in an extrusion printing (e.g., DIW) process, high loading of nanomaterials for shear force patterning can lead to a substantial increase in viscosity that limits the resolution of the printing process. This constraint can be alleviated by developing unique ink formulations to impart shear thinning

behavior. For example, Wang et al. proposed a solution to this problem by formulating an ink containing polymer chains that form transient networks of hydrogen bonds and hydrophobic interactions.^[169] These bonds are disrupted by shear forces and quickly reconstitute after printing, imparting a shear-thinning behavior that allowed direct ink writing of a 90 wt% nanothermite construct. Indeed, material advancement and ink formulation play a critical role in overcoming the fundamental limitations in a broad range of multiscale 3D printing, such as DIW.

Third, we envision that the synergistic integration of multiple patterning phenomena can overcome the fundamental limitations of a specific patterning methodology. For example, we highlighted cases of hybrid nanopatterning processes (Section 11) that integrated thermal phenomena with fluid shear or magnetic phenomena. Gantenbein et al.^[414] leveraged a combination of fluid shear and substrate heating to create a core-shell liquid crystal polymer with heterogeneous reinforcement. Nelson et al. demonstrated a combination of magnetic patterning and freeze casting^[416] to achieve better control of the parallel lamellae formation during dendritic ice growth.

Indeed, developing the ability to pattern and control nanomaterials in a 3D printing process can enable a multiscale, multimaterial additive manufacturing strategy that can create devices and architecture with unprecedented complexity and functional integration, which has a broad and long-lasting impact on a wide range of fields—from bioprinting^[25,50,179,418] to space exploration.^[419–422]

In summary, in this review, we first introduced the unique properties of nanomaterials and their attractive attributes as building blocks to program and modulate a wide range of features for 3D architectures and devices. We then provided an overview of the selected classes of 3D printing technologies that have significant potential to achieve multiscale integration. Most importantly, we highlighted the development of multiscale, multimaterial additive manufacturing approaches by leveraging mechanical, electrical, magnetic, optical, or thermal phenomena. The ability to spatially modulate and program material properties in a hierarchical architecture extends the reach of 3D printing to create highly functional constructs, which represents an auspicious evolution that fundamentally overcomes the limitations of conventional manufacturing methodologies. Excitingly, these advances could lead to the creation of next-generation devices and architectures that cannot be produced with conventional manufacturing technologies.

Acknowledgements

The authors acknowledge funding support in part from the Department of Mechanical Engineering of the University of Utah, Ralph E. Powe Junior Faculty Enhancement Award by Oak Ridge Associated Universities (ORAU) as well as the National Science Foundation under Emerging Frontiers in Research and Innovation (EFRI) Program (Grant No. EFRI 1830958).

Conflict of Interest

Y.L.K. is an inventor on multiple patents and patent applications describing 3D printing technologies, including active electronic materials and devices, and multifunctional hybrid devices and structures. Y.L.K. is

also an inventor of gastric-resident systems, including gastric-resident electronics. All other authors declare no conflict of interest.

Keywords

micrometer-scale patterning and assembly, multiscale 3D printing, nanomaterials

Received: October 31, 2019

Revised: December 18, 2019

Published online: March 4, 2020

- [1] M. Haslam, A. Hernandez-Aguilar, V. Ling, S. Carvalho, I. de la Torre, A. DeStefano, A. Du, B. Hardy, J. Harris, L. Marchant, T. Matsuzawa, W. McGrew, J. Mercader, R. Mora, M. Petraglia, H. Roche, E. Visalberghi, R. Warren, *Nature* **2009**, 460, 339.
- [2] Y. Yang, X. Song, X. Li, Z. Chen, C. Zhou, Q. Zhou, Y. Chen, *Adv. Mater.* **2018**, 30, 1706539.
- [3] A. P. J. Acksion, J. F. V. Vincent, R. M. T. Urner, *Proc. R. Soc. London, Ser. B* **2006**, 234, 415.
- [4] J. C. Weaver, G. W. Milliron, A. Miserez, K. Evans-Lutterodt, S. Herrera, I. Gallana, W. J. Mershon, B. Swanson, P. Zavattieri, E. DiMasi, D. Kisailus, *Science* **2012**, 336, 1275.
- [5] T. Hoc, L. Henry, M. Verdier, D. Aubry, L. Sedel, A. Meunier, *Bone* **2006**, 38, 466.
- [6] P. Vukusic, J. R. Sambles, *Nature* **2003**, 424, 852.
- [7] K. Michielsen, D. Stavenga, *J. R. Soc., Interface* **2008**, 5, 85.
- [8] A. L. Ingram, V. Lousse, A. R. Parker, J. P. Vigneron, *J. R. Soc., Interface* **2008**, 5, 1387.
- [9] S. Kinoshita, S. Yoshioka, K. Kawagoe, *Proc. R. Soc. London, Ser. B* **2002**, 269, 1417.
- [10] P. Romano, H. Fabritius, D. Raabe, *Acta Biomater.* **2007**, 3, 301.
- [11] U. Cerkvenik, B. van de Straat, S. W. S. Gussekloo, J. L. van Leeuwen, *Proc. Natl. Acad. Sci. USA* **2017**, 114, E7822.
- [12] O. F. Chernova, *Dokl. Biol. Sci.* **2005**, 405, 437.
- [13] X. Gao, X. Yan, X. Yao, L. Xu, K. Zhang, J. Zhang, B. Yang, L. Jiang, *Adv. Mater.* **2007**, 19, 2213.
- [14] A. G. Domel, G. Domel, J. C. Weaver, M. Saadat, K. Bertoldi, G. V. Lauder, *Bioinspir. Biomim.* **2018**, 13, 056014.
- [15] C. E. Killian, R. A. Metzler, Y. Gong, T. H. Churchill, I. C. Olson, V. Trubetskoy, M. B. Christensen, J. H. Fournelle, F. De Carlo, S. Cohen, J. Mahamid, A. Scholl, A. Young, A. Doran, F. H. Wilt, S. N. Coppersmith, P. U. P. A. Gilbert, *Adv. Funct. Mater.* **2011**, 21, 682.
- [16] M. A. Meyers, Y. S. Lin, E. A. Olevsky, P.-Y. Chen, *Adv. Eng. Mater.* **2012**, 14, B279.
- [17] L. M. Mäthger, E. J. Denton, N. J. Marshall, R. T. Hanlon, *J. R. Soc., Interface* **2009**, 6, S149.
- [18] Y. Zheng, H. Bai, Z. Huang, X. Tian, F.-Q. Nie, Y. Zhao, J. Zhai, L. Jiang, *Nature* **2010**, 463, 640.
- [19] V. C. Sundar, A. D. Yablon, J. L. Grazul, M. Ilan, J. Aizenberg, *Nature* **2003**, 424, 899.
- [20] Y. Forterre, J. M. Skotheim, J. Dumais, L. Mahadevan, *Nature* **2005**, 433, 421.
- [21] S. Armon, E. Efrati, R. Kupferman, E. Sharon, *Science* **2011**, 333, 1726.
- [22] A. Miserez, T. Schneberk, C. Sun, F. W. Zok, J. H. Waite, *Science* **2008**, 319, 1816.
- [23] G. V. Lauder, D. K. Wainwright, A. G. Domel, J. C. Weaver, L. Wen, K. Bertoldi, *Phys. Rev. Fluids* **2016**, 1, 060502.

- [24] J. C. Weaver, Q. Wang, A. Miserez, A. Tantuccio, R. Stromberg, K. N. Bozhilov, P. Maxwell, R. Nay, S. T. Heier, E. DiMasi, D. Kisailus, *Mater. Today* **2010**, 13, 42.
- [25] Y. L. Kong, M. K. Gupta, B. N. Johnson, M. C. McAlpine, *Nano Today* **2016**, 11, 330.
- [26] A. H. Espera, J. R. C. Dizon, Q. Chen, R. C. Advincula, *Prog. Addit. Manuf.* **2019**, 4, 245.
- [27] M. C. McAlpine, M. Sebastian-Mannoor, Y. L. Kong, B. N. Johnson, US9517128B2, **2014**.
- [28] S. Hales, E. Tokita, R. Neupane, U. Ghosh, B. Elder, D. S. Wirthlin, Y. L. Kong, *Nanotechnology* **2019**, <https://doi.org/10.1088/1361-6528/ab5f29>.
- [29] J. J. Martin, B. E. Fiore, R. M. Erb, *Nat. Commun.* **2015**, 6, 8641.
- [30] T. Nakamoto, S. Kojima, *J. Adv. Mech. Des. Syst. Manuf.* **2012**, 6, 849.
- [31] D. Kokkinis, M. Schaffner, A. R. Studart, *Nat. Commun.* **2015**, 6, 8643.
- [32] D. Li, Y. Xia, *Nano Lett.* **2004**, 4, 933.
- [33] A. Reiser, M. Lindén, P. Rohner, A. Marchand, H. Galinski, A. S. Sologubenko, J. M. Wheeler, R. Zenobi, D. Poulikakos, R. Spolenak, *Nat. Commun.* **2019**, 10, 1853.
- [34] Y. Yang, Z. Chen, X. Song, Z. Zhang, J. Zhang, K. K. Shung, Q. Zhou, Y. Chen, *Adv. Mater.* **2017**, 29, 1605750.
- [35] X. Zheng, H. Lee, T. H. Weisgraber, M. Shusteff, J. DeOtte, E. B. Duoss, J. D. Kuntz, M. M. Biener, Q. Ge, J. A. Jackson, S. O. Kucheyev, N. X. Fang, C. M. Spadaccini, *Science* **2014**, 344, 1373.
- [36] X. Zheng, W. Smith, J. Jackson, B. Moran, H. Cui, D. Chen, J. Ye, N. Fang, N. Rodriguez, T. Weisgraber, C. M. Spadaccini, *Nat. Mater.* **2016**, 15, 1100.
- [37] Q. Zhang, F. Zhang, S. P. Medarametla, H. Li, C. Zhou, D. Lin, *Small* **2016**, 12, 1702.
- [38] Q. Zhang, F. Zhang, X. Xu, C. Zhou, D. Lin, *ACS Nano* **2018**, 12, 1096.
- [39] K. E. Roskov, K. A. Kozek, W. C. Wu, R. K. Chhetri, A. L. Oldenburg, R. J. Spontak, J. B. Tracy, *Langmuir* **2011**, 27, 13965.
- [40] Y. L. Kong, I. A. Tamargo, H. Kim, B. N. Johnson, M. K. Gupta, T. W. Koh, H. A. Chin, D. A. Steingart, B. P. Rand, M. C. McAlpine, *Nano Lett.* **2014**, 14, 7017.
- [41] Y. Xia, B. Gates, Z. Y. Li, *Adv. Mater.* **2001**, 13, 409.
- [42] H. Kim, J. Ge, J. Kim, S. Choi, H. Lee, H. Lee, W. Park, Y. Yin, S. Kwon, *Nat. Photonics* **2009**, 3, 534.
- [43] T. Gissibl, S. Thiele, A. Herkommer, H. Giessen, *Nat. Photonics* **2016**, 10, 554.
- [44] D. E. Yunus, S. Sohrabi, R. He, W. Shi, Y. Liu, *J. Micromech. Microeng.* **2017**, 27, 045016.
- [45] J. H. Kim, W. S. Chang, D. Kim, J. R. Yang, J. T. Han, G.-W. Lee, J. T. Kim, S. K. Seol, *Adv. Mater.* **2015**, 27, 157.
- [46] M. Su, Z. Huang, Y. Li, X. Qian, Z. Li, X. Hu, Q. Pan, F. Li, L. Li, Y. Song, *Adv. Mater.* **2018**, 30, 1703963.
- [47] K. Chen, L. Zhang, X. Kuang, V. Li, M. Lei, G. Kang, Z. L. Wang, H. J. Qi, *Adv. Funct. Mater.* **2019**, 29, 1903568.
- [48] A. Sydney Gladman, E. A. Matsumoto, R. G. Nuzzo, L. Mahadevan, J. A. Lewis, *Nat. Mater.* **2016**, 15, 413.
- [49] L. Lu, P. Guo, Y. Pan, *J. Manuf. Sci. Eng.* **2017**, 139, 071008.
- [50] E. A. Guzzi, M. W. Tibbitt, *Adv. Mater.* **2019**, 1901994.
- [51] D. Chimene, K. K. Lennox, R. R. Kaunas, A. K. Gaharwar, *Ann. Biomed. Eng.* **2016**, 44, 2090.
- [52] G. Gao, A. F. Schilling, T. Yonezawa, J. Wang, G. Dai, X. Cui, *Biotechnol. J.* **2014**, 9, 1304.
- [53] A. E. Jakus, E. B. Secor, A. L. Rutz, S. W. Jordan, M. C. Hersam, R. N. Shah, *ACS Nano* **2015**, 9, 4636.
- [54] Y. Yang, X. Li, M. Chu, H. Sun, J. Jin, K. Yu, Q. Wang, Q. Zhou, Y. Chen, *Sci. Adv.* **2019**, 5, eaau9490.
- [55] A. Theron, E. Zussman, A. L. Yarin, *Nanotechnology* **2001**, 12, 384.
- [56] K. Apro, *Secrets of 5-Axis Machining*, Industrial Press, South Norwalk, Connecticut **2009**.
- [57] Y. Takeuchi, Y. Yoneyama, T. Ishida, T. Kawai, *CIRP Ann.* **2009**, 58, 53.
- [58] M. J. Madou, *Manufacturing Techniques for Microfabrication and Nanotechnology*, CRC Press, Boca Raton, FL **2018**.
- [59] J. W. Judy, *Smart Mater. Struct.* **2001**, 10, 1115.
- [60] G. Boothroyd, *Comput. Des.* **1994**, 26, 505.
- [61] X. Zha, H. Du, J. Qiu, *Eng. Appl. Artif. Intell.* **2001**, 14, 61.
- [62] H. Kexin, in *Dev. Modul. Prod.* (Eds: K. A. Henry, C. R. Mackenzie), Frontiers, Lausanne, Switzerland **2004**, pp. 85–90.
- [63] L. Kyjaková, R. Bašková, *Tech. Trans.* **2016**, 2016, 35.
- [64] R. B. Stone, *Towards a Theory of Modular Design*, The University of Texas at Austin, Austin, TX **1997**.
- [65] G. Erixon, *Modular Function Deployment: A Method for Product Modularisation*, The Royal Institute of Technology, Department of Manufacturing Systems, Assembly Systems Division, Stockholm, Sweden **1998**.
- [66] R. Clancy, V. Jamalabad, P. Whalen, P. Bhargava, C. Dai, S. Rangarajan, S. Wu, S. Danforth, N. Langrana, A. Safari, in *Proc. 8th Annu. Int. Solid Free. Fabr. Symp.*, Austin, TX **1997**, p. 185.
- [67] J. Oeffner, G. V. Lauder, M. A. Grosenbaugh, *J. Exp. Biol.* **2012**, 215, 785.
- [68] M. Fulekar, *Nanotechnology: Importance and Applications*, I.K. International Publishing House Pvt. Ltd., New Delhi **2010**.
- [69] A. K. Nair, A. Mayeen, L. K. Shaji, M. S. Kala, in *Charact. Nanomater.* Woodhead Publishing **2018**, pp. 269–299.
- [70] H. Goesmann, C. Feldmann, *Angew. Chem., Int. Ed.* **2010**, 49, 1362.
- [71] A. P. Alivisatos, *Science* **1996**, 271, 933.
- [72] S. L. Lai, J. Y. Guo, V. Petrova, G. Ramanath, L. H. Allen, *Phys. Rev. Lett.* **1996**, 77, 99.
- [73] P. R. Couchman, W. A. Jesser, *Nature* **1977**, 269, 481.
- [74] K. S. Moon, H. Dong, R. Maric, S. Pothukuchi, A. Hunt, Y. I. Li, C. P. Wong, *J. Electron. Mater.* **2005**, 34, 168.
- [75] J. S. Kang, J. Ryu, H. S. Kim, H. T. Hahn, *J. Electron. Mater.* **2011**, 40, 2268.
- [76] A. Z. Moshfegh, *J. Phys. D: Appl. Phys.* **2009**, 42, 233001.
- [77] R. M. Erb, R. Libanori, N. Rothfuchs, A. R. Studart, *Science* **2012**, 335, 199.
- [78] K. N. Al-Milaji, R. R. Secondo, T. N. Ng, N. Kinsey, H. Zhao, *Adv. Mater. Interfaces* **2018**, 5, 1701561.
- [79] Y. Min, M. Akbulut, K. Kristiansen, Y. Golan, J. Israelachvili, *Nat. Mater.* **2008**, 7, 527.
- [80] J. Israelachvili, *Intermolecular and Surface Forces*, Academic Press, Cambridge, Massachusetts **2011**.
- [81] C. R. Deckard, J. J. Beaman, J. F. Darrah, US5155324, **1990**.
- [82] I. S. Kinstlinger, A. Bastian, S. J. Paulsen, D. H. Hwang, A. H. Ta, D. R. Yalacki, T. Schmidt, J. S. Miller, *PLoS One* **2016**, 11, e0147399.
- [83] ASTM International, *Standard Terminology for Additive Manufacturing Technologies—ISO/ASTM 52900:2015(E)*, ASTM International, West Conshohocken, PA **2015**.
- [84] C. Sun, N. Fang, D. M. Wu, X. Zhang, *Sens. Actuators, A* **2005**, 121, 113.
- [85] H. H. Hwang, W. Zhu, G. Victorine, N. Lawrence, S. Chen, *Small Methods* **2018**, 2, 1870021.
- [86] R. Januszewicz, J. R. Tumbleston, A. L. Quintanilla, S. J. Mecham, J. M. DeSimone, *Proc. Natl. Acad. Sci. USA* **2016**, 113, 11703.
- [87] T. D. Ngo, A. Kashani, G. Imbalzano, K. T. Q. Nguyen, D. Hui, *Composites, Part B* **2018**, 143, 172.
- [88] X. Wang, M. Jiang, Z. Zhou, J. Gou, D. Hui, *Composites, Part B* **2017**, 110, 442.
- [89] B. Utela, D. Storti, R. Anderson, M. Ganter, *J. Manuf. Process.* **2008**, 10, 96.

- [90] A. K. Miri, D. Nieto, L. Iglesias, H. Goodarzi Hosseinabadi, S. Maharjan, G. U. Ruiz-Esparza, P. Khoshakhlagh, A. Manbachi, M. R. Dokmeci, S. Chen, S. R. Shin, Y. S. Zhang, A. Khademhosseini, *Adv. Mater.* **2018**, *30*, 1800242.
- [91] J. J. Schwartz, A. J. Boydston, *Nat. Commun.* **2019**, *10*, 791.
- [92] J. Barna, J. Torok, L. Novakova-Marcincinova, I. Kuric, *Manuf. Ind. Eng.* **2012**, *11*, 1338.
- [93] J. A. Lewis, *Adv. Funct. Mater.* **2006**, *16*, 2193.
- [94] P. Calvert, *Chem. Mater.* **2001**, *13*, 3299.
- [95] Y. L. Kong, in *Micro-Nanotechnol. Sensors, Syst. Appl. XI* (Eds: M. S. Islam, T. George), SPIE, Bellingham, WA **2019**, p. 11.
- [96] F. M. White, *Fluid Mechanics*, McGraw-Hill Higher Education, Boston, MA **1999**.
- [97] G. B. Jeffery, *Proc. R. Soc. London, Ser. A* **1922**, *102*, 161.
- [98] M. D. Haslam, B. Raeymaekers, *Composites, Part B* **2014**, *60*, 91.
- [99] J. Greenhall, F. Guevara Vasquez, B. Raeymaekers, *Appl. Phys. Lett.* **2016**, *108*, 103103.
- [100] D. Shin, J. Kim, S. Choi, Y. Lee, J. Chang, *J. Micromech. Microeng.* **2019**, *29*, 045004.
- [101] D. H. Reneker, A. L. Yarin, *Polymer* **2008**, *49*, 2387.
- [102] P. Ferraro, S. Coppola, S. Grilli, M. Paturzo, V. Vespini, *Nat. Nanotechnol.* **2010**, *5*, 429.
- [103] J. Sun, B. Bhushan, *RSC Adv.* **2012**, *2*, 7617.
- [104] H. D. Espinosa, A. L. Juster, F. J. Latourte, O. Y. Loh, D. Gregoire, P. D. Zavattieri, *Nat. Commun.* **2011**, *2*, 173.
- [105] D. Liu, H. D. Wagner, S. Weiner, *J. Mater. Sci.: Mater. Med.* **2000**, *11*, 49.
- [106] J. W. Boley, K. Chaudhary, T. J. Ober, M. Khorasaninejad, W. T. Chen, E. Hanson, A. Kulkarni, J. Oh, J. Kim, L. K. Aagesen, A. Y. Zhu, F. Capasso, K. Thornton, P. V. Braun, J. A. Lewis, *Adv. Mater.* **2017**, *29*, 1604778.
- [107] A. Kamyshny, S. Magdassi, *Small* **2014**, *10*, 3515.
- [108] Y. Sun, *Science* **2002**, *298*, 2176.
- [109] F. Xu, Y. Zhu, *Adv. Mater.* **2012**, *24*, 5117.
- [110] T. Sekitani, H. Nakajima, H. Maeda, T. Fukushima, T. Aida, K. Hata, T. Someya, *Nat. Mater.* **2009**, *8*, 494.
- [111] M. Kubo, X. Li, C. Kim, M. Hashimoto, B. J. Wiley, D. Ham, G. M. Whitesides, *Adv. Mater.* **2010**, *22*, 2749.
- [112] A. E. Aliev, J. Oh, M. E. Kozlov, A. A. Kuznetsov, S. Fang, A. F. Fonseca, R. Ovalle, M. D. Lima, M. H. Haque, Y. N. Gartstein, M. Zhang, A. A. Zakhidov, R. H. Baughman, *Science* **2009**, *323*, 1575.
- [113] D. H. Kim, N. Lu, R. Ma, Y. S. Kim, R. H. Kim, S. Wang, J. Wu, S. M. Won, H. Tao, A. Islam, K. J. Yu, T. Il Kim, R. Chowdhury, M. Ying, L. Xu, M. Li, H. J. Chung, H. Keum, M. McCormick, P. Liu, Y. W. Zhang, F. G. Omenetto, Y. Huang, T. Coleman, J. A. Rogers, *Science* **2011**, *333*, 838.
- [114] G. Siqueira, D. Kokkinis, R. Libanori, M. K. Hausmann, A. S. Gladman, A. Neels, P. Tingaut, T. Zimmermann, J. A. Lewis, A. R. Studart, *Adv. Funct. Mater.* **2017**, *27*, 1604619.
- [115] D. van der Beek, A. V. Petukhov, P. Davidson, J. Ferré, J. P. Jamet, H. H. Wensink, G. J. Vroege, W. Bras, H. N. W. Lekkerkerker, *Phys. Rev. E* **2006**, *73*, 041402.
- [116] B. Bar-On, X. Sui, K. Livanov, B. Achrai, E. Kalfon-Cohen, E. Wiesel, H. Daniel Wagner, *Appl. Phys. Lett.* **2014**, *105*, 033703.
- [117] A. K. Gaharwar, N. A. Peppas, A. Khademhosseini, *Biotechnol. Bioeng.* **2014**, *111*, 441.
- [118] J. R. Xavier, T. Thakur, P. Desai, M. K. Jaiswal, N. Sears, E. Cosgriff-Hernandez, R. Kaunas, A. K. Gaharwar, *ACS Nano* **2015**, *9*, 3109.
- [119] S. R. Shin, S. M. Jung, M. Zalabany, K. Kim, P. Zorlutuna, S. B. Kim, M. Nikkhah, M. Khabiry, M. Azize, J. Kong, K. T. Wan, T. Palacios, M. R. Dokmeci, H. Bae, X. Tang, A. Khademhosseini, *ACS Nano* **2013**, *7*, 2369.
- [120] E. A. Guzzi, G. Bovone, M. W. Tibbitt, *Small* **2019**, *15*, 1905421.
- [121] M. Lee, K. Bae, P. Guillon, J. Chang, Ø. Arlov, M. Zenobi-Wong, *ACS Appl. Mater. Interfaces* **2018**, *10*, 37820.
- [122] M. Attaran, *Bus. Horiz.* **2017**, *60*, 677.
- [123] U. Ghosh, S. Ning, Y. Wang, Y. L. Kong, *Adv. Healthcare Mater.* **2018**, *7*, 1800417.
- [124] E. M. Sachs, J. S. Haggerty, M. J. Cima, P. A. Williams, *US5204055A*, **1995**.
- [125] R. L. Truby, J. A. Lewis, *Nature* **2016**, *540*, 371.
- [126] C. Hull, *US4575330A*, **1986**.
- [127] Z. Gan, Y. Cao, R. A. Evans, M. Gu, *Nat. Commun.* **2013**, *4*, 2061.
- [128] W. Xiong, Y. S. Zhou, X. N. He, Y. Gao, M. Mahjour-Samani, L. Jiang, T. Baldacchini, Y. F. Lu, *Light Sci.: Appl.* **2012**, *1*, e6.
- [129] J. R. Tumbleston, D. Shirvanyants, N. Ermoshkin, R. Januszewicz, A. R. Johnson, D. Kelly, K. Chen, R. Pinschmidt, J. P. Rolland, A. Ermoshkin, E. T. Samulski, J. M. DeSimone, *Science* **2015**, *347*, 1349.
- [130] S. Crump, *Apparatus and Method for Creating Three-Dimensional Objects*, Stratasys, Inc., Minneapolis, Minn. **1989**.
- [131] J. Hornick, D. Roland, Many 3D Printing Patents Are Expiring Soon: Here's A Round Up & Overview of Them—3D Printing Industry, <https://3dprintingindustry.com/news/many-3d-printing-patents-expiring-soon-heres-round-overview-21708/> (accessed: October 2019).
- [132] E. Malone, H. Lipson, *Rapid Prototyping J.* **2007**, *13*, 245.
- [133] J. West, G. Kuk, *Technol. Forecast. Soc. Change* **2016**, *102*, 169.
- [134] K. C. Wong, S. M. Kumta, N. V. L. Gee, J. Demol, *Comput. Aided Surg.* **2015**, *20*, 14.
- [135] A. Cohen, A. Laviv, P. Berman, R. Nashef, J. Abu-Tair, *Oral Surg., Oral Med., Oral Pathol., Oral Radiol. Endodontol.* **2009**, *108*, 661.
- [136] Y. L. Kong, *Homel. Def. Inf. Anal. Cent.* **2019**, *6*, 34.
- [137] R. S. Langer, C. G. Traverso, Y. L. Kong, *US20190209090A1*, **2018**.
- [138] P. Nadeau, D. El-Damak, D. Glettig, Y. L. Kong, S. Mo, C. Cleveland, L. Booth, N. Roxhed, R. Langer, A. P. Chandrakasan, G. Traverso, *Nat. Biomed. Eng.* **2017**, *1*, 0022.
- [139] K. H. Herrmann, C. Gärtner, D. Güllmar, M. Krämer, J. R. Reichenbach, *Med. Eng. Phys.* **2014**, *36*, 1373.
- [140] R. J. Morrison, S. J. Hollister, M. F. Niedner, M. G. Mahani, A. H. Park, D. K. Mehta, R. G. Ohye, G. E. Green, *Sci. Transl. Med.* **2015**, *7*, 285ra64.
- [141] Y. L. Kong, X. Zou, C. A. McCandler, A. R. Kirtane, S. Ning, J. Zhou, A. Abid, M. Jafari, J. Rogner, D. Minahan, J. E. Collins, S. McDonnell, C. Cleveland, T. Bense, S. Tamang, G. Arrick, A. Gimbel, T. Hua, U. Ghosh, V. Soares, N. Wang, A. Wahane, A. Hayward, S. Zhang, B. R. Smith, R. Langer, G. Traverso, *Adv. Mater. Technol.* **2019**, *4*, 1800490.
- [142] S. Y. Chin, Y. C. Poh, A. C. Kohler, J. T. Compton, L. L. Hsu, K. M. Lau, S. Kim, B. W. Lee, F. Y. Lee, S. K. Sia, *Sci. Rob.* **2017**, *2*, eaah6451.
- [143] S. Mellor, L. Hao, D. Zhang, *Int. J. Prod. Econ.* **2014**, *149*, 194.
- [144] L. E. Murr, *J. Mater. Sci. Technol.* **2016**, *32*, 987.
- [145] L. Li, A. Haghighi, Y. Yang, *J. Manuf. Process.* **2018**, *33*, 150.
- [146] L. Sabantina, F. Kinzel, A. Ehrmann, K. Finsterbusch, *IOP Conf. Ser.: Mater. Sci. Eng.* **2015**, *87*, 012005.
- [147] W. Oropallo, L. A. Piegl, *Eng. Comput.* **2016**, *32*, 135.
- [148] X. You, J. Yang, Q. Feng, K. Huang, H. Zhou, J. Hu, S. Dong, *Int. J. Light. Mater. Manuf.* **2018**, *1*, 96.
- [149] H. Kodama, *Rev. Sci. Instrum.* **1981**, *52*, 1770.
- [150] X. Zheng, J. Deotte, M. P. Alonso, G. R. Farquar, T. H. Weisgraber, S. Gemberling, H. Lee, N. Fang, C. M. Spadaccini, *Rev. Sci. Instrum.* **2012**, *83*, 125001.
- [151] B. H. Cumpston, S. P. Ananthavel, S. Barlow, D. L. Dyer, J. E. Ehrlich, L. L. Erskine, A. A. Heikal, S. M. Kuebler, I. Y. S. Lee, D. McCord-Maughon, J. Qin, H. Röckel, M. Rumi, X. L. Wu, S. R. Marder, J. W. Perry, *Nature* **1999**, *398*, 51.

- [152] I. Gibson, D. W. Rosen, B. Stucker, in *Addit. Manuf. Technol.* (Ed: C. Glaser), Springer US, Boston, MA, **2010**, pp. 120–159.
- [153] A. Bournias Varotsis, Introduction to Binder Jetting 3D Printing, <https://www.3dhubs.com/knowledge-base/introduction-binder-jetting-3d-printing#what> (accessed: December 2019).
- [154] B. J. De Gans, P. C. Duineveld, U. S. Schubert, *Adv. Mater.* **2004**, 16, 203.
- [155] B. Derby, *Annu. Rev. Mater. Res.* **2010**, 40, 395.
- [156] F. Alifui-Segbaya, S. Varma, G. J. Lieschke, R. George, *3D Print. Addit. Manuf.* **2017**, 4, 185.
- [157] A. Ovsianikov, B. Chichkov, P. Mente, N. A. Monteiro-Riviere, A. Doraiswamy, R. J. Narayan, *Int. J. Appl. Ceram. Technol.* **2007**, 4, 22.
- [158] V. C.-F. Li, X. Kuang, A. Mulyadi, C. M. Hamel, Y. Deng, H. J. Qi, *Cellulose* **2019**, 26, 3973.
- [159] Y. Han, C. C. J. Yeo, D. Chen, F. Wang, Y. Chong, X. Li, X. Jiao, F. Wang, *New J. Chem.* **2017**, 41, 8407.
- [160] Y. Zhang, H. Li, X. Yang, T. Zhang, K. Zhu, W. Si, Z. Liu, H. Sun, *Polym. Compos.* **2018**, 39, E671.
- [161] J. Z. Manapat, Q. Chen, P. Ye, R. C. Advincula, *Macromol. Mater. Eng.* **2017**, 302, 1600553.
- [162] F. P. W. Melchels, J. Feijen, D. W. Grijpma, *Biomaterials* **2010**, 31, 6121.
- [163] Y. Wang, Y. F. Zhao, *Procedia Manuf.* **2017**, 10, 779.
- [164] I. Gibson, D. W. Rosen, B. Stucker, in *Addit. Manuf. Technol.* (Ed: C. Glaser), Springer US, Boston, MA **2010**, pp. 187–222.
- [165] J. O. Hardin, T. J. Ober, A. D. Valentine, J. A. Lewis, *Adv. Mater.* **2015**, 27, 3279.
- [166] C. O'Mahony, E. U. Haq, C. Sillien, S. A. M. Tofail, C. O'Mahony, E. U. Haq, C. Sillien, S. A. M. Tofail, *Micromachines* **2019**, 10, 99.
- [167] L. Hirt, A. Reiser, R. Spolenak, T. Zambelli, *Adv. Mater.* **2017**, 29, 1604211.
- [168] Y. Jin, K. Song, N. Gellermann, Y. Huang, *ACS Appl. Mater. Interfaces* **2019**, 11, 29207.
- [169] H. Wang, J. Shen, D. J. Kline, N. Eckman, N. R. Agrawal, T. Wu, P. Wang, M. R. Zachariah, *Adv. Mater.* **2019**, 31, 1806575.
- [170] M. S. Mannoor, Z. Jiang, T. James, Y. L. Kong, K. A. Malatesta, W. O. Soboyejo, N. Verma, D. H. Gracias, M. C. McAlpine, *Nano Lett.* **2013**, 13, 2634.
- [171] M. K. Gupta, F. Meng, B. N. Johnson, Y. L. Kong, L. Tian, Y.-W. Yeh, N. Masters, S. Singamaneni, M. C. McAlpine, *Nano Lett.* **2015**, 15, 5321.
- [172] B. N. Johnson, K. Z. Lancaster, G. Zhen, J. He, M. K. Gupta, Y. L. Kong, E. A. Engel, K. D. Krick, A. Ju, F. Meng, L. W. Enquist, X. Jia, M. C. McAlpine, *Adv. Funct. Mater.* **2015**, 25, 6205.
- [173] B. N. Johnson, K. Z. Lancaster, I. B. Hogue, F. Meng, Y. L. Kong, L. W. Enquist, M. C. McAlpine, *Lab Chip* **2016**, 16, 1393.
- [174] D. Kokkinis, F. Bouville, A. R. Studart, *Adv. Mater.* **2018**, 30, 1705808.
- [175] Y. Yu, F. Liu, R. Zhang, J. Liu, *Adv. Mater. Technol.* **2017**, 2, 1700173.
- [176] J. T. Muth, D. M. Vogt, R. L. Truby, Y. Mengüç, D. B. Kolesky, R. J. Wood, J. A. Lewis, *Adv. Mater.* **2014**, 26, 6307.
- [177] K. Hajash, B. Sparrman, C. Guberman, J. Laucks, S. Tibbits, *3D Print. Addit. Manuf.* **2017**, 4, 123.
- [178] T. Bhattacharjee, S. M. Zehnder, K. G. Rowe, S. Jain, R. M. Nixon, W. G. Sawyer, T. E. Angelini, *Sci. Adv.* **2015**, 1, e1500655.
- [179] D. B. Kolesky, R. L. Truby, A. S. Gladman, T. A. Busbee, K. A. Homan, J. A. Lewis, *Adv. Mater.* **2014**, 26, 3124.
- [180] T. J. Hinton, Q. Jallerat, R. N. Palchesko, J. H. Park, M. S. Grodzicki, H.-J. Shue, M. H. Ramadan, A. R. Hudson, A. W. Feinberg, *Sci. Adv.* **2015**, 1, e1500758.
- [181] A. Lee, H. Jin, H. W. Dang, K. H. Choi, K. H. Ahn, *Langmuir* **2013**, 29, 13630.
- [182] L. Wang, A. J. Ryan, in *Electrospinning for Tissue Regeneration* (Eds: L. A. Bosworth, S. Downes), Woodhead Publishing **2011**, pp. 3–33.
- [183] J. U. Park, J. H. Lee, U. Paik, Y. Lu, J. A. Rogers, *Nano Lett.* **2008**, 8, 4210.
- [184] M. Hedges, A. B. Marin, in *DDMC 2012 Conf.*, Berlin, Germany **2012**, p. 1.
- [185] M. S. Saleh, C. Hu, R. Panat, *Sci. Adv.* **2017**, 3, e1601986.
- [186] J. A. Paulsen, M. Renn, K. Christenson, R. Plourde, in *FIIW 2012—2012 Futur. Instrum. Int. Work. Proc.* (Ed: D. Abbott), IEEE, Piscataway, NJ **2012**, pp. 47–50.
- [187] J. W. Stansbury, M. J. Idacavage, *Dent. Mater.* **2016**, 32, 54.
- [188] T. J. Wallin, J. Pikul, R. F. Shepherd, *Nat. Rev. Mater.* **2018**, 3, 84.
- [189] T. D. Papathanasiou, D. C. Guell, *Flow-Induced Alignment in Composite Materials*, Woodhead Publishing Limited, Cambridge, England **1997**.
- [190] D. E. Yunus, W. Shi, S. Sohrabi, Y. Liu, *Nanotechnology* **2016**, 27, 495302.
- [191] C. Fucinõs, P. Fucinõs, M. Míguez, I. Katime, L. M. Pastrana, M. L. Rúa, *PLoS One* **2014**, 9, e87190.
- [192] J. Hu, H. Meng, G. Li, S. I. Ibekwe, *Smart Mater. Struct.* **2012**, 21, 053001.
- [193] S. Felton, M. Tolley, E. Demaine, D. Rus, R. Wood, *Science* **2014**, 345, 644.
- [194] Y. Jin, C. Liu, W. Chai, A. Compaan, Y. Huang, *ACS Appl. Mater. Interfaces* **2017**, 9, 17456.
- [195] M. K. Hausmann, P. A. Rühs, G. Siqueira, J. Läger, R. Libanori, T. Zimmermann, A. R. Studart, *ACS Nano* **2018**, 12, 6926.
- [196] S. J. Leigh, R. J. Bradley, C. P. Purcell, D. R. Billson, D. A. Hutchins, *PLoS One* **2012**, 7, e49365.
- [197] R. M. Martin, *Phys. Rev. B* **1972**, 5, 1607.
- [198] A. Nafari, H. A. Sodano, *Smart Mater. Struct.* **2019**, 28, 045014.
- [199] C. Andrews, Y. Lin, H. A. Sodano, *Smart Mater. Struct.* **2010**, 19, 025018.
- [200] N. Zhou, Y. Bekenstein, C. N. Eisler, D. Zhang, A. M. Schwartzberg, P. Yang, A. P. Alivisatos, J. A. Lewis, *Sci. Adv.* **2019**, 5, eaav8141.
- [201] H. Lee, B. Seong, J. Kim, Y. Jang, D. Byun, *Small* **2014**, 10, 3918.
- [202] L. Lu, X. Tang, S. Hu, Y. Pan, *3D Print. Addit. Manuf.* **2018**, 5, 151.
- [203] S. Shabaniverki, S. Thorud, J. J. Juárez, *Chem. Eng. Sci.* **2018**, 192, 1209.
- [204] M. S. Scholz, B. W. Drinkwater, R. S. Trask, *Ultrasonics* **2014**, 54, 1015.
- [205] T. Nakamoto, S. Marukado, *Int. J. Autom. Technol.* **2016**, 10, 916.
- [206] C. Yang, *Int. J. Adv. Manuf. Technol.* **2013**, 68, 1745.
- [207] J. Giboz, T. Copponnex, P. Mélé, *J. Micromech. Microeng.* **2009**, 19, 025023.
- [208] Z. Lu, K. F. Zhang, *Int. J. Adv. Manuf. Technol.* **2009**, 40, 490.
- [209] Z. Lu, K. F. Zhang, *Polym. Eng. Sci.* **2009**, 49, 1661.
- [210] G. Trujillo-De Santiago, M. M. Alvarez, M. Samandari, G. Prakash, G. Chandrabhatla, P. I. Rellstab-Sánchez, B. Byambaa, P. Pour Shahid Saeed Abadi, S. Mandla, R. K. Avery, A. Vallejo-Arroyo, A. Nasajpour, N. Annabi, Y. S. Zhang, A. Khademhosseini, *Mater. Horiz.* **2018**, 5, 813.
- [211] H. J. Cui, H. M. Yu, J. F. Zheng, Z. J. Wang, Y. Y. Zhu, S. P. Jia, J. Jia, Z. P. Zhu, *Nanoscale* **2016**, 8, 2795.
- [212] A. Hauke, L. S. S. Kumar, M. Y. Kim, J. Pegan, M. Khine, H. Li, K. W. Plaxco, J. Heikenfeld, *Biosens. Bioelectron.* **2017**, 94, 438.
- [213] M. Gou, X. Qu, W. Zhu, M. Xiang, J. Yang, K. Zhang, Y. Wei, S. Chen, *Nat. Commun.* **2014**, 5, 3774.
- [214] M. R. Gullo, S. Takeuchi, O. Paul, *Adv. Healthcare Mater.* **2017**, 6, 1601053.
- [215] K. R. Stevens, M. A. Scull, V. Ramanan, C. L. Fortin, R. R. Chaturvedi, K. A. Knouse, J. W. Xiao, C. Fung, T. Mirabella, A. X. Chen, M. G. McCue, M. T. Yang, H. E. Fleming, K. Chung, Y. P. De Jong, C. S. Chen, C. M. Rice, S. N. Bhatia, *Sci. Transl. Med.* **2017**, 9, eaah5505.
- [216] G. M. Whitesides, B. Grzybowski, *Science* **2002**, 295, 2418.
- [217] N. Bassik, G. M. Stern, M. Jamal, D. H. Gracias, *Adv. Mater.* **2008**, 20, 4760.

- [218] Y. Zhang, F. Zhang, Z. Yan, Q. Ma, X. Li, Y. Huang, J. A. Rogers, *Nat. Rev. Mater.* **2017**, 2, 17019.
- [219] A. T. L. Tan, J. Beroz, M. Kolle, A. J. Hart, *Adv. Mater.* **2018**, 30, 1803620.
- [220] R. D. Deegan, O. Bakajin, T. F. Dupont, G. Huber, S. R. Nagel, T. A. Witten, *Nature* **1997**, 389, 827.
- [221] S. Boissé, J. Rieger, K. Belal, A. Di-Cicco, P. Beaunier, M.-H. Li, B. Charleux, *Chem. Commun.* **2010**, 46, 1950.
- [222] A. Crivoi, F. Duan, *J. Phys. Chem. B* **2013**, 117, 5932.
- [223] H. Fan, S. Reed, T. Baer, R. Schunk, G. P. López, C. J. Brinker, *Microporous Mesoporous Mater.* **2001**, 44–45, 625.
- [224] R. D. Deegan, *Phys. Rev. E: Stat. Phys., Plasmas, Fluids, Relat. Interdiscip. Top.* **2000**, 61, 475.
- [225] Y. Li, C. Fu, J. Xu, *Jpn. J. Appl. Phys.* **2007**, 46, 6807.
- [226] F. Wang, H. Wu, *Sci. Rep.* **2015**, 5, 17521.
- [227] T. P. Bigioni, X.-M. Lin, T. T. Nguyen, E. I. Corwin, T. A. Witten, H. M. Jaeger, *Nat. Mater.* **2006**, 5, 265.
- [228] Y. L. Kong, F. Boulogne, H. Kim, J. Nunes, J. Feng, H. A. Stone, *Langmuir* **2015**, 31, 12560.
- [229] C. Wang, X. Wang, Y. Wang, J. Chen, H. Zhou, Y. Huang, *Nano Energy* **2015**, 11, 678.
- [230] C. Kullmann, N. C. Schirmer, M.-T. Lee, S. H. Ko, N. Hotz, C. P. Grigoropoulos, D. Poulikakos, *J. Micromech. Microeng.* **2012**, 22, 055022.
- [231] M. Kuang, J. Wang, B. Bao, F. Li, L. Wang, L. Jiang, Y. Song, *Adv. Opt. Mater.* **2014**, 2, 34.
- [232] F. Boulogne, Y. L. Kong, J. K. Nunes, H. A. Stone, *Phys. Rev. Lett.* **2016**, 116, 238001.
- [233] C. Lu, N. Wu, X. Jiao, C. Luo, W. Cao, *Chem. Commun.* **2003**, 3, 1056.
- [234] H. Zhang, C. Wang, M. Li, X. Ji, J. Zhang, B. Yang, *Chem. Mater.* **2005**, 17, 4783.
- [235] B. Dubertret, P. Skourides, D. J. Norris, V. Noireaux, A. H. Brivanlou, A. Libchaber, *Science* **2002**, 298, 1759.
- [236] S. Vafaei, C. Tuck, I. Ashcroft, R. Wildman, *Chem. Eng. Res. Des.* **2016**, 109, 414.
- [237] A. Stannard, *J. Phys.: Condens. Matter* **2011**, 23, 083001.
- [238] C. Jiang, Z. Zhong, B. Liu, Z. He, J. Zou, L. Wang, J. Wang, J. Peng, Y. Cao, *ACS Appl. Mater. Interfaces* **2016**, 8, 26162.
- [239] A. Askounis, K. Sefiane, V. Koutsos, M. E. R. Shanahan, *Colloids Surf., A* **2014**, 441, 855.
- [240] D. Soltman, V. Subramanian, *Langmuir* **2008**, 24, 2224.
- [241] A. Mohapatra, A. Singh, S. A. Abbas, Y.-J. Lu, K. M. Boopathi, C. Hanmandlu, N. Kaiser, C.-H. Lee, C.-W. Chu, *Nano Energy* **2019**, 63, 103826.
- [242] C. Linghu, S. Zhang, C. Wang, J. Song, *npj Flexible Electron.* **2018**, 2, 26.
- [243] A. A. Yu, T. Savas, S. Cabrini, E. DiFabrizio, H. I. Smith, F. Stellacci, *J. Am. Chem. Soc.* **2005**, 127, 16774.
- [244] B. N. Chandrashekar, A. S. Smitha, Y. Wu, N. Cai, Y. Li, Z. Huang, W. Wang, R. Shi, J. Wang, S. Liu, S. Krishnaveni, F. Wang, C. Cheng, *Sci. Rep.* **2019**, 9, 3999.
- [245] R. D. Piner, J. Zhu, F. Xu, S. Hong, C. A. Mirkin, *Science* **1999**, 283, 661.
- [246] S. Zhang, *Nat. Biotechnol.* **2003**, 21, 1171.
- [247] P. Yin, H. M. T. Choi, C. R. Calvert, N. A. Pierce, *Nature* **2008**, 451, 318.
- [248] K. M. Ryan, A. Mastroianni, K. A. Stancil, H. Liu, A. P. Alivisatos, *Nano Lett.* **2006**, 6, 1479.
- [249] B. D. Korth, P. Keng, I. Shim, S. E. Bowles, C. Tang, T. Kowalewski, K. W. Nebesny, J. Pyun, *J. Am. Chem. Soc.* **2006**, 128, 6562.
- [250] R. Sheparovych, Y. Sahoo, M. Motornov, S. Wang, H. Luo, P. N. Prasad, I. Sokolov, S. Minko, *Chem. Mater.* **2006**, 18, 591.
- [251] J. Park, J. Moon, *Langmuir* **2006**, 22, 3506.
- [252] D. J. Harris, J. A. Lewis, *Langmuir* **2008**, 24, 3681.
- [253] H. Hu, R. G. Larson, *J. Phys. Chem. B* **2006**, 110, 7090.
- [254] C. G. Sztrum, O. Hod, E. Rabani, *J. Phys. Chem. B* **2005**, 109, 6741.
- [255] M. O. Blunt, C. P. Martin, M. Ahola-Tuomi, E. Pauliac-Vaujour, P. Sharp, P. Nativio, M. Brust, P. J. Moriarty, *Nat. Nanotechnol.* **2007**, 2, 167.
- [256] Y. Bai, L. Yan, J. Wang, Z. Yin, N. Chen, F. Wang, Z. Tan, *Mater. Des.* **2016**, 103, 315.
- [257] W. Cheng, N. Park, M. T. Walter, M. R. Hartman, D. Luo, *Nat. Nanotechnol.* **2008**, 3, 682.
- [258] L. Maillard, L. Motte, M. P. Pileni, *Adv. Mater.* **2001**, 13, 200.
- [259] C. Stowell, B. A. Korgel, *Nano Lett.* **2001**, 1, 595.
- [260] C. P. Martin, M. O. Blunt, P. Moriarty, *Nano Lett.* **2004**, 4, 2389.
- [261] A. Stannard, C. P. Martin, E. Pauliac-Vaujour, P. Moriarty, U. Thiele, *J. Phys. Chem. C* **2008**, 112, 15195.
- [262] P. C. Ohara, J. R. Heath, W. M. Gelbart, *Angew. Chem., Int. Ed. Engl.* **1997**, 36, 1078.
- [263] L. V. Govor, G. Reiter, J. Parisi, G. H. Bauer, *Phys. Rev. E: Stat. Phys., Plasmas, Fluids, Relat. Interdiscip. Top.* **2004**, 69, 8.
- [264] A. Stannard, H. Alhummiy, E. Pauliac-Vaujour, J. S. Sharp, P. Moriarty, U. Thiele, *Langmuir* **2010**, 26, 13892.
- [265] G. Ge, L. Brus, *J. Phys. Chem. B* **2002**, 104, 9573.
- [266] E. Rabani, D. R. Reichman, P. L. Geissler, L. E. Brus, *Nature* **2003**, 426, 271.
- [267] C. G. Sztrum, E. Rabani, *Adv. Mater.* **2006**, 18, 565.
- [268] O. Kletenik-Edelman, C. G. Sztrum-Vartash, E. Rabani, *J. Mater. Chem.* **2009**, 19, 2872.
- [269] O. Kletenik-Edelman, E. Ploshnik, A. Salant, R. Shenhar, U. Banin, E. Rabani, *J. Phys. Chem. C* **2008**, 112, 4498.
- [270] C. P. Martin, M. O. Blunt, E. Pauliac-Vaujour, A. Stannard, P. Moriarty, I. Vancea, U. Thiele, *Phys. Rev. Lett.* **2007**, 99, 116103.
- [271] G. Yosef, E. Rabani, *J. Phys. Chem. B* **2006**, 110, 20965.
- [272] H. Zhang, Y. G. Shan, L. Li, M. Lu, R. Li, *Appl. Therm. Eng.* **2016**, 94, 650.
- [273] J. Hao, Z. Wang, Z. Wang, Y. Yin, R. Jiang, B. Li, Q. Wang, *Macromolecules* **2017**, 50, 4384.
- [274] B. Li, W. Han, M. Byun, L. Zhu, Q. Zou, Z. Lin, *ACS Nano* **2013**, 7, 4326.
- [275] A. Stein, B. E. Wilson, S. G. Rudisill, *Chem. Soc. Rev.* **2013**, 42, 2763.
- [276] C. I. Aguirre, E. Reguera, A. Stein, *Adv. Funct. Mater.* **2010**, 20, 2565.
- [277] M. Kuang, L. Wang, Y. Song, *Adv. Mater.* **2014**, 26, 6950.
- [278] D. Mampallil, H. B. Eral, *Adv. Colloid Interface Sci.* **2018**, 252, 38.
- [279] W. Li, D. Lan, Y. Wang, *Phys. Rev. E* **2017**, 95, 042607.
- [280] K. N. Al-Milaji, H. Zhao, *J. Phys. Chem. C* **2019**, 123, 12029.
- [281] R. G. Larson, *AIChE J.* **2014**, 60, 1538.
- [282] S. Kinge, M. Crego-Calama, D. N. Reinhoudt, *ChemPhysChem* **2008**, 9, 20.
- [283] C. R. P. Courtney, C. K. Ong, B. W. Drinkwater, A. L. Bernassau, P. D. Wilcox, D. R. S. Cumming, *Proc. R. Soc. London, Ser. A* **2012**, 468, 337.
- [284] H. Sazan, S. Piperno, M. Layani, S. Magdassi, H. Shpaysman, *J. Colloid Interface Sci.* **2019**, 536, 701.
- [285] M. C. Gaidis, L. Thomas, *Nanoscale Semicond. Memories Technol. Appl.* **2013**, 320, 229.
- [286] J. Dean, M. T. Bryan, J. D. Cooper, A. Virbule, J. E. Cunningham, T. J. Hayward, *Appl. Phys. Lett.* **2015**, 107, 142405.
- [287] A. Ozcelik, J. Rufo, F. Guo, Y. Gu, P. Li, J. Lata, T. J. Huang, *Nat. Methods* **2018**, 15, 1021.
- [288] J. Shi, D. Ahmed, X. Mao, S. C. S. Lin, A. Lawit, T. J. Huang, *Lab Chip* **2009**, 9, 2890.
- [289] H. Bruus, *Lab Chip* **2012**, 12, 1014.
- [290] M. Kumar, D. L. Feke, J. M. Belovich, *Biotechnol. Bioeng.* **2005**, 89, 129.

- [291] C. Reyes, L. Fu, P. P. A. Suthanthiraraj, C. E. Owens, C. W. Shields, G. P. López, P. Charbonneau, B. J. Wiley, *Part. Part. Syst. Charact.* **2018**, 35, 1700470.
- [292] L. Meng, F. Cai, F. Li, W. Zhou, L. Niu, H. Zheng, *J. Phys. D: Appl. Phys.* **2019**, 52, 273001.
- [293] A. Marzo, S. A. Seah, B. W. Drinkwater, D. R. Sahoo, B. Long, S. Subramanian, *Nat. Commun.* **2015**, 6, 8661.
- [294] T. Vasileiou, D. Foresti, A. Bayram, D. Poulikakos, A. Ferrari, *Sci. Rep.* **2016**, 6, 20023.
- [295] D. Foresti, M. Nabavi, M. Klingauf, A. Ferrari, D. Poulikakos, *Proc. Natl. Acad. Sci. USA* **2013**, 110, 12549.
- [296] M. Wu, Y. Ouyang, Z. Wang, R. Zhang, P.-H. Huang, C. Chen, H. Li, P. Li, D. Quinn, M. Dao, S. Suresh, Y. Sadovsky, T. J. Huang, *Proc. Natl. Acad. Sci. USA* **2017**, 114, 10584.
- [297] D. J. Collins, Z. Ma, J. Han, Y. Ai, *Lab Chip* **2017**, 17, 91.
- [298] J. R. Wu, *J. Acoust. Soc. Am.* **1991**, 89, 2140.
- [299] M. Saito, T. Daian, K. Hayashi, S. Y. Izumida, *J. Appl. Phys.* **1998**, 83, 3490.
- [300] M. K. Tan, J. R. Friend, L. Y. Yeo, *Lab Chip* **2007**, 7, 618.
- [301] G. Sitters, D. Kamsma, G. Thalhammer, M. Ritsch-Marte, E. J. G. Peterman, G. J. L. Wuite, *Nat. Methods* **2014**, 12, 47.
- [302] H. Schlicke, T. Jochum, S. C. Bittinger, T. Vossmeier, J. S. Niehaus, H. Weller, in *2018 IEEE 13th Nanotechnol. Mater. Devices Conf.* (Ed: D. Abbott), IEEE, Piscataway, NJ **2018**, pp. 1–4.
- [303] R. Das, A. J. Pattanayak, S. K. Swain, in *Polym. Nanocomposites Energy Environ. Appl.*, Elsevier **2018**, pp. 205–218.
- [304] Y. Lu, M. C. Biswas, Z. Guo, J. W. Jeon, E. K. Wujcik, *Biosens. Bioelectron.* **2019**, 123, 167.
- [305] T. M. Llewellyn-Jones, B. W. Drinkwater, R. S. Trask, *Smart Mater. Struct.* **2016**, 25, 02LT01.
- [306] J. Greenhall, L. Homel, B. Raeymaekers, *J. Compos. Mater.* **2019**, 53, 1329.
- [307] P. S. Theocaris, J. Milios, *Int. J. Fract.* **1980**, 16, 31.
- [308] M. T. Tilbrook, R. J. Moon, M. Hoffman, *Compos. Sci. Technol.* **2005**, 65, 201.
- [309] M. T. Tilbrook, K. Rozenburg, E. D. Steffler, L. Rutgers, M. Hoffman, *Composites, Part B* **2006**, 37, 490.
- [310] K. Friedrich, R. Walter, H. Voss, J. Karger-Kocsis, *Composites* **1986**, 17, 205.
- [311] S. Parkin, S.-H. Yang, *Nat. Nanotechnol.* **2015**, 10, 195.
- [312] S. Yim, K. Goyal, M. Sitti, *IEEE/ASME Trans. Mechatronics* **2013**, 18, 1413.
- [313] S. Yim, M. Sitti, *IEEE Trans. Rob.* **2012**, 28, 183.
- [314] B. W. An, K. Kim, H. Lee, S. Y. Kim, Y. Shim, D. Y. Lee, J. Y. Song, J. U. Park, *Adv. Mater.* **2015**, 27, 4322.
- [315] M. Yu, K. H. Ahn, S. J. Lee, *Mater. Des.* **2016**, 89, 109.
- [316] R. T. Collins, M. T. Harris, O. A. Basaran, *J. Fluid Mech.* **2007**, 588, 75.
- [317] A. L. Yarin, S. Koombhongse, D. H. Reneker, *J. Appl. Phys.* **2001**, 90, 4836.
- [318] D. Shin, J. Kim, J. Chang, *J. Manuf. Process.* **2018**, 36, 231.
- [319] S.-Y. Min, T.-S. Kim, B. J. Kim, H. Cho, Y.-Y. Noh, H. Yang, J. H. Cho, T.-W. Lee, *Nat. Commun.* **2013**, 4, 1773.
- [320] X. Liu, L. Gu, Q. Zhang, J. Wu, Y. Long, Z. Fan, *Nat. Commun.* **2014**, 5, 4007.
- [321] C. Soci, A. Zhang, B. Xiang, S. A. Dayeh, D. P. R. Aplin, J. Park, X. Y. Bao, Y. H. Lo, D. Wang, *Nano Lett.* **2007**, 7, 1003.
- [322] D. Li, Y. Xia, *Nano Lett.* **2003**, 3, 555.
- [323] C. L. Zhang, K. P. Lv, N. Y. Hu, L. Yu, X. F. Ren, S. L. Liu, S. H. Yu, *Small* **2012**, 8, 2936.
- [324] J. U. Park, M. Hardy, S. J. Kang, K. Barton, K. Adair, D. K. Mukhopadhyay, C. Y. Lee, M. S. Strano, A. G. Alleyne, J. G. Georgiadis, P. M. Ferreira, J. A. Rogers, *Nat. Mater.* **2007**, 6, 782.
- [325] F. Molina-Lopez, T. Z. Gao, U. Kraft, C. Zhu, T. Öhlund, R. Pfattner, V. R. Feig, Y. Kim, S. Wang, Y. Yun, Z. Bao, *Nat. Commun.* **2019**, 10, 2676.
- [326] T. Someya, Z. Bao, G. G. Malliaras, *Nature* **2016**, 540, 379.
- [327] W. Lee, D. Kim, J. Rivnay, N. Matsuhisa, T. Lonjaret, T. Yokota, H. Yawo, M. Sekino, G. G. Malliaras, T. Someya, *Adv. Mater.* **2016**, 28, 9722.
- [328] W. Xu, S.-Y. Min, H. Hwang, T.-W. Lee, *Sci. Adv.* **2016**, 2, e1501326.
- [329] Y. Kim, A. Chortos, W. Xu, Y. Liu, J. Y. Oh, D. Son, J. Kang, A. M. Foudeh, C. Zhu, Y. Lee, S. Niu, J. Liu, R. Pfattner, Z. Bao, T.-W. Lee, *Science* **2018**, 360, 998.
- [330] T. Takahashi, T. Murayama, A. Higuchi, H. Awano, K. Yonetake, *Carbon* **2006**, 44, 1180.
- [331] L. A. Chavez, J. E. Regis, L. C. Delfin, C. A. Garcia Rosales, H. Kim, N. Love, Y. Liu, Y. Lin, *J. Appl. Polym. Sci.* **2019**, 136, 47600.
- [332] T. Subbiah, G. S. Bhat, R. W. Tock, S. Parameswaran, S. S. Ramkumar, *J. Appl. Polym. Sci.* **2005**, 96, 557.
- [333] D. Li, Y. Xia, *Adv. Mater.* **2004**, 16, 1151.
- [334] A. K. Moghe, B. S. Gupta, *Polym. Rev.* **2008**, 48, 353.
- [335] A. Greiner, J. H. Wendorff, *Angew. Chem., Int. Ed.* **2007**, 46, 5670.
- [336] A. Frenot, I. S. Chronakis, *Curr. Opin. Colloid Interface Sci.* **2003**, 8, 64.
- [337] Q. Li, C. W. Kartikowati, S. Horie, T. Ogi, T. Iwaki, K. Okuyama, *Sci. Rep.* **2017**, 7, 9894.
- [338] J. Mohapatra, J. P. Liu, in *Handbook of Magnetic Materials* (Ed: E. Brück), North Holland Amsterdam, Netherlands **2018**, pp. 1–57.
- [339] R. F. Butler, in *Paleomagn. Magn. Domains to Geol. Terranes* (Ed: S. Rallison), Blackwell Scientific Publications, Hoboken, NJ **1992**, pp. 16–30.
- [340] M. H. Dodson, E. McClelland-Brown, *J. Geophys. Res.* **1980**, 85, 2625.
- [341] M. Winklhofer, K. Fabian, F. Heider, *J. Geophys. Res.: Solid Earth* **1997**, 102, 22695.
- [342] J. Wan, G. Tang, Y. Qian, *Appl. Phys. A* **2006**, 86, 261.
- [343] Y. Kim, H. Yuk, R. Zhao, S. A. Chester, X. Zhao, *Nature* **2018**, 558, 274.
- [344] R. M. Erb, J. Segmehl, M. Charilaou, J. F. Löffler, A. R. Studart, *Soft Matter* **2012**, 8, 7604.
- [345] S. Weiner, H. D. Wagner, *Annu. Rev. Mater. Sci.* **1998**, 28, 271.
- [346] D. W. Lee, *Am. Sci.* **1997**, 85, 56.
- [347] D. W. Lee, *Nature* **1991**, 349, 260.
- [348] J. Zi, X. Yu, Y. Li, X. Hu, C. Xu, X. Wang, X. Liu, R. Fu, *Proc. Natl. Acad. Sci. USA* **2003**, 100, 12576.
- [349] S. Tokura, M. Hara, N. Kawaguchi, N. Amemiya, *J. Magn. Magn. Mater.* **2016**, 411, 68.
- [350] R. Barry, J. Ambro, US5309246A, **1991**.
- [351] J. S. Choi, J. Yoo, *IEEE Trans. Magn.* **2008**, 44, 2361.
- [352] J. Li, E. H. Hill, L. Lin, Y. Zheng, *ACS Nano* **2019**, 13, 3783.
- [353] A. Vyatskikh, S. Delalande, A. Kudo, X. Zhang, C. M. Portela, J. R. Greer, *Nat. Commun.* **2018**, 9, 593.
- [354] M. Deubel, G. Von Freymann, M. Wegener, S. Pereira, K. Busch, C. M. Soukoulis, *Nat. Mater.* **2004**, 3, 444.
- [355] M. Röhrig, M. Thiel, M. Worgull, H. Hölscher, *Small* **2012**, 8, 3009.
- [356] A. Ashkin, *Phys. Rev. Lett.* **1970**, 24, 156.
- [357] A. S. Urban, A. A. Lutich, F. D. Stefani, J. Feldmann, *Nano Lett.* **2010**, 10, 4794.
- [358] G. Von Freymann, V. Kitaev, B. V. Lotsch, G. A. Ozin, *Chem. Soc. Rev.* **2013**, 42, 2528.
- [359] A. F. Koenderink, A. Lagendijk, W. L. Vos, *Phys. Rev. B: Condens. Matter Mater. Phys.* **2005**, 72, 153102.
- [360] J. Hu, in *Act. Coatings Smart Text.* (Ed.: J. Hu), Woodhead Publishing, Cambridge, England **2016**, pp. 1–463.
- [361] S. M. Kuebler, C. Xia, R. Sharma, J. L. Diggaum, N. P. Martinez, C. L. Valle, R. C. Rumpf, in *Org. Photonic Mater. Devices XXI* (Eds: C. E. Tabor, F. Kajzar, T. Kaino), SPIE, Bellingham, WA **2019**, p. 1.

- [362] J. Serbin, A. Egbert, A. Ostendorf, B. N. Chichkov, R. Houbertz, G. Domann, J. Schulz, C. Cronauer, L. Fröhlich, M. Popall, *Opt. Lett.* **2003**, 28, 301.
- [363] A. Ovsianikov, J. Viertel, B. Chichkov, M. Oubaha, B. MacCraith, I. Sakellari, A. Giakoumaki, D. Gray, M. Vamvakaki, M. Farsari, C. Fotakis, *ACS Nano* **2008**, 2, 2257.
- [364] J. Serbin, A. Ovsianikov, B. Chichkov, *Opt. Express* **2004**, 12, 5221.
- [365] K. Kaneko, H.-B. Sun, X.-M. Duan, S. Kawata, *Appl. Phys. Lett.* **2003**, 83, 2091.
- [366] R. Guo, Z. Li, Z. Jiang, D. Yuan, W. Huang, A. Xia, *J. Opt. A: Pure Appl. Opt.* **2005**, 7, 396.
- [367] K. Kim, W. Zhu, X. Qu, C. Aaronson, W. R. McCall, S. Chen, D. J. Sirbuly, *ACS Nano* **2014**, 8, 9799.
- [368] K. Kim, J. L. Middlebrook, J. E. Chen, W. Zhu, S. Chen, D. J. Sirbuly, *ACS Appl. Mater. Interfaces* **2016**, 8, 33394.
- [369] H. Cui, R. Hensleigh, D. Yao, D. Maurya, P. Kumar, M. G. Kang, S. Priya, X. Zheng, *Nat. Mater.* **2019**, 18, 234.
- [370] R. M. Hensleigh, H. Cui, J. S. Oakdale, J. C. Ye, P. G. Campbell, E. B. Duoss, C. M. Spadaccini, X. Zheng, M. A. Worsley, *Mater. Horiz.* **2018**, 5, 1035.
- [371] J. H. Strickler, W. W. Webb, in *CAN-AM East '90* (Eds: R. L. Antos, A. J. Krisiloff), SPIE, Bellingham, WA **2012**, pp. 107–118.
- [372] S. Steenhusen, F. Burmeister, M. Groß, G. Domann, R. Houbertz, S. Nolte, *Thin Solid Films* **2018**, 668, 74.
- [373] T. Bückmann, N. Stenger, M. Kadic, J. Kaschke, A. Frölich, T. Kennerknecht, C. Eberl, M. Thiel, M. Wegener, *Adv. Mater.* **2012**, 24, 2710.
- [374] W. Zheng, in *Adv. Opt. Imaging Technol.* (Eds: X.-C. Yuan, K. Shi, M. G. Somekh), SPIE, Bellingham, WA **2018**, p. 7.
- [375] F. Ding, A. Pors, S. I. Bozhevolnyi, *Rep. Prog. Phys.* **2018**, 81, 026401.
- [376] Y. Cheng, H. Zhang, X. S. Mao, R. Z. Gong, *Mater. Lett.* **2018**, 219, 123.
- [377] P. Fan, B. Bai, G. Jin, H. Zhang, M. Zhong, *Appl. Surf. Sci.* **2018**, 457, 991.
- [378] E.-T. Hu, X.-X. Liu, Y. Yao, K.-Y. Zang, Z.-J. Tu, A.-Q. Jiang, K.-H. Yu, J.-J. Zheng, W. Wei, Y.-X. Zheng, R.-J. Zhang, S.-Y. Wang, H.-B. Zhao, O. Yoshie, Y.-P. Lee, C.-Z. Wang, D. W. Lynch, J.-P. Guo, L.-Y. Chen, *Mater. Res. Express* **2018**, 5, 066428.
- [379] J. Bauer, L. R. Meza, T. A. Schaedler, R. Schwaiger, X. Zheng, L. Valdevit, *Adv. Mater.* **2017**, 29, 1701850.
- [380] L. C. Montemayor, J. R. Greer, *J. Appl. Mech.* **2015**, 82, 071012.
- [381] V. S. Deshpande, N. A. Fleck, M. F. Ashby, *J. Mech. Phys. Solids* **2001**, 49, 1747.
- [382] W. Y. Jang, S. Kyriakides, A. M. Kraynik, *Int. J. Solids Struct.* **2010**, 47, 2872.
- [383] Y. Takahashi, D. Okumura, N. Ohno, *Int. J. Mech. Sci.* **2010**, 52, 377.
- [384] R. Lakes, *Nature* **1993**, 361, 511.
- [385] Y. Tao, W. Li, K. Wei, S. Duan, W. Wen, L. Chen, Y. Pei, D. Fang, *Composites, Part B* **2019**, 176, 107219.
- [386] R. Oftadeh, B. Haghighpanah, D. Vella, A. Boudaoud, A. Vaziri, *Phys. Rev. Lett.* **2014**, 113, 104301.
- [387] G. N. Greaves, A. L. Greer, R. S. Lakes, T. Rouxel, *Nat. Mater.* **2011**, 10, 823.
- [388] A. Marino, C. Filippeschi, V. Mattoli, B. Mazzolai, G. Ciofani, *Nanoscale* **2015**, 7, 2841.
- [389] A. Marino, C. Filippeschi, G. G. Genchi, V. Mattoli, B. Mazzolai, G. Ciofani, *Acta Biomater.* **2014**, 10, 4304.
- [390] K. Autumn, C. Majidi, R. E. Groff, A. Dittmore, R. Fearing, *J. Exp. Biol.* **2006**, 209, 3558.
- [391] B. Schubert, J. Lee, C. Majidi, R. S. Fearing, *J. R. Soc., Interface* **2008**, 5, 845.
- [392] M. K. Kwak, H. E. Jeong, W. G. Bae, H.-S. Jung, K. Y. Suh, *Small* **2011**, 7, 2296.
- [393] C. Greiner, A. del Campo, E. Arzt, *Langmuir* **2007**, 23, 3495.
- [394] A. K. Nguyen, R. J. Narayan, *Mater. Today* **2017**, 20, 314.
- [395] M. B. Frank, S. E. Naleway, T. Haroush, C. H. Liu, S. H. Siu, J. Ng, I. Torres, A. Ismail, K. Karandikar, M. M. Porter, O. A. Graeve, J. McKittrick, *Mater. Sci. Eng., C* **2017**, 77, 484.
- [396] S. Deville, E. Saiz, R. K. Nalla, A. P. Tomsia, *Science* **2006**, 311, 515.
- [397] U. G. K. Wegst, M. Schecter, A. E. Donius, P. M. Hunger, *Philos. Trans. R. Soc., A* **2010**, 368, 2099.
- [398] K. L. Scotti, D. C. Dunand, *Prog. Mater. Sci.* **2018**, 94, 243.
- [399] I. Nelson, S. E. Naleway, *J. Mater. Res. Technol.* **2019**, 8, 2372.
- [400] L. Qiu, J. Z. Liu, S. L. Y. Chang, Y. Wu, D. Li, *Nat. Commun.* **2012**, 3, 1241.
- [401] F. E. Wang, in *Bond. Theory Met. Alloy*. (Ed: A. Hess), Elsevier, Amsterdam **2019**, pp. 157–191.
- [402] J. F. Shackelford, in *Introduction to Mater. Sci. Eng.* (Eds: H. Stark, S. Rodriguez), Pearson Higher Education, Upper Saddle River, NJ, **2016**, pp. 261–280.
- [403] V. Seetharaman, R. Trivedi, *Metall. Trans. A* **1988**, 19, 2955.
- [404] J. Kim, L. K. Agesen, J. H. Choi, J. Choi, H. S. Kim, J. Liu, C.-R. Cho, J. G. Kang, A. Ramazani, K. Thornton, P. V. Braun, *Adv. Mater.* **2015**, 27, 4551.
- [405] R. I. Merino, M. F. Acosta, V. M. Orera, *J. Eur. Ceram. Soc.* **2014**, 34, 2061.
- [406] S. Bhowmick, M. Iodice, M. Gioffrè, G. Breglio, A. Irace, M. Riccio, G. Romano, S. Grilli, P. Ferraro, L. Mecozzi, S. Coppola, O. Gennari, R. Rega, G. Coppola, *Sens. Actuators, A* **2017**, 261, 140.
- [407] H. Maiwa, *Nanoscale Ferroelectr.-Multiferroic Mater. Energy Harvesting Appl.* (Eds: H. Kimura, Z. Cheng, T. Jia), Elsevier **2019**, pp. 217–229.
- [408] S. Sanna, W. G. Schmidt, *Phys. Rev. B* **2010**, 81, 214116.
- [409] S. Coppola, V. Vespini, V. Bianco, L. Mecozzi, F. Olivieri, M. Todino, M. Paturzo, S. Grilli, P. Ferraro, in *Proc. SPIE 9705, Microfluidics, BioMEMS, and Medical Microsystems XIV* (Eds: B. L. Gray, H. Becker), Bellingham, WA **2016**, p. 97050L.
- [410] F. Merola, S. Grilli, S. Coppola, V. Vespini, S. DeNicola, P. Maddalena, C. Carfagna, P. Ferraro, *Mol. Cryst. Liq. Cryst.* **2013**, 572, 66.
- [411] S. Coppola, V. Vespini, L. Mecozzi, L. Miccio, S. Grilli, P. Ferraro, I. A. Grimaldi, F. Loffredo, G. Nenna, E. Lepera, F. Villani, C. Minarini, in *2014 Fotonica AEIT Ital. Conf. Photonics Technol.* (Ed: D. Abbott), IEEE, Piscataway, NJ **2014**, pp. 1–3.
- [412] O. A. Basaran, *AIChE J.* **2002**, 48, 1842.
- [413] H. Song, D. L. Chen, R. F. Ismagilov, *Angew. Chem., Int. Ed.* **2006**, 45, 7336.
- [414] S. Gantenbein, K. Masania, W. Woigk, J. P. W. Sesse, T. A. Tervoort, A. R. Studart, *Nature* **2018**, 561, 226.
- [415] P. Niksjar, F. Su, M. Frank, T. Ogden, S. Naleway, M. Meyers, J. McKittrick, M. Porter, *Ceramics* **2019**, 2, 208.
- [416] I. Nelson, T. A. Ogden, S. Al Khateeb, J. Graser, T. D. Sparks, J. J. Abbott, S. E. Naleway, *Adv. Eng. Mater.* **2019**, 21, 1.
- [417] R. P. Feynman, *J. Microelectromech. Syst.* **2002**, 1, 60.
- [418] M. A. Sklyar-Scott, S. G. M. Uzel, L. L. Nam, J. H. Ahrens, R. L. Truby, S. Damaraju, J. A. Lewis, *Sci. Adv.* **2019**, 5, eaaw2459.
- [419] China National Space Administration to Establish 3D Printed Houses on the Moon—3D Printing Industry, <https://3dprintingindustry.com/news/china-national-space-administration-to-establish-3d-printed-houses-on-the-moon-147133/> (accessed: September 2019).
- [420] M. Gaskill, Solving the Challenges of Long Duration Space Flight with 3D Printing | NASA, **2019**, https://www.nasa.gov/mission_pages/station/research/news/3d-printing-in-space-long-duration-spaceflight-applications.

- [421] T. Prater, N. Werkheiser, F. Ledbetter, D. Timucin, K. Wheeler, M. Snyder, *Int. J. Adv. Manuf. Technol.* **2019**, *101*, 391.
- [422] K. Northon, NASA Funds Demo of 3D-Printed Parts Made, Assembled in Orbit, **2019** <https://www.nasa.gov/press-release/nasa-funds-demo-of-3d-printed-spacecraft-parts-made-assembled-in-orbit/> (accessed: September 2019).
- [423] B9 Core Series Technical Specifications | B9Creations, <https://www.b9c.com/products/tech-specs> (accessed: December 2019).
- [424] PICO₂—Products—Asiga, <https://www.asiga.com/products/printers/pico2/> (accessed: December 2019).
- [425] Solidator 2—DLP 3D Printer—Fast Stereolithography 3D Printer with a Large Build Volume” <https://www.solidator.com/3D-Printer.html#targetText=The%Solidator%is%an%ultra,13.22%22x8.26%22> (accessed: December 2019).
- [426] Pro Desktop 3D Printer Technical Specifications | SprintRay Inc., <https://sprintray.com/pro-desktop-3d-printer-technical-specifications/> (accessed: December 2019).
- [427] F. P. W. Melchels, J. Feijen, D. W. Grijpma, *Biomaterials*. **2010**, *31*, 6121.
- [428] M. Shusteff, A. E. M. Browar, B. E. Kelly, J. Henriksson, T. H. Weisgraber, R. M. Panas, N. X. Fang, C. M. Spadaccini, *Sci. Adv.* **2017**, *3*, eaao5496.
- [429] N. Afshar-Mohajer, C. Y. Wu, T. Ladun, D. A. Rajon, Y. Huang, *Build. Environ.* **2015**, *93*, 293.
- [430] M. Singh, H. M. Haverinen, P. Dhagat, G. E. Jabbour, *Adv. Mater.* **2010**, *22*, 673.
- [431] J. He, F. Xu, R. Dong, B. Guo, D. Li, *Biofabrication* **2017**, *9*, 015007.
- [432] Z. K. Nagy, A. Balogh, B. Démuth, H. Pataki, T. Vigh, B. Szabó, K. Molnár, B. T. Schmidt, P. Horák, G. Marosi, G. Verreck, I. Van Assche, M. E. Brewster, *Int. J. Pharm.* **2015**, *480*, 137.
- [433] A. Mahajan, C. D. Frisbie, L. F. Francis, *ACS Appl. Mater. Interfaces* **2013**, *5*, 4856.